
THE UNIVERSITY
*of* EDINBURGH

# Investigating tropospheric and surface ozone sensitivity from present day to future

**Zhenze Liu**

Doctor of Philosophy

School of Geosciences

University of Edinburgh

November 2021

# Declaration

I declare that this thesis has been composed solely by myself and that it has not been submitted, either in whole or in part, in any previous application for a degree. Except where otherwise acknowledged, the work presented is entirely my own.

Zhenze Liu

November 2021

# Abstract

Tropospheric ozone ($O_3$) is an important reactive gas in the atmosphere influencing human health, ecosystems and climate. Since the mid-20th century, scientists started to explore the mechanism of tropospheric $O_3$ formation after severe $O_3$ air pollution in Los Angeles. They found that $O_3$ is a photochemical pollutant as its formation involves energy from sunlight, as well as precursors nitrogen oxide ($NO_x$), volatile organic compounds (VOCs) and carbon monoxide (CO). Nowadays, highly $O_3$ polluted episodes can still occur in areas where emissions have been controlled strictly due to the non-linear chemical reactions of $O_3$ formation. Therefore, it is important to implement suitable emission control strategies to mitigate $O_3$ pollution, and to understand the impacts of emissions and climate on $O_3$ changes in the future.

Firstly, a chemistry scheme with more reactive VOC species is developed based on the Strat-Trop chemistry scheme in the United Kingdom Earth System Model, UKESM1. This permits a more realistic and photochemically active environment for $O_3$ simulation in areas with high reactive VOC emissions. The effectiveness of emission controls in reducing surface $O_3$ concentrations in the industrial regions of China in summer, 2016, is investigated. The concentrations of surface $O_3$ in those regions generally can be simulated accurately, and the diurnal variation of $O_3$ can also be captured

well by the model. $O_3$ production in most regions is VOC-limited, suggesting that surface $O_3$ concentrations will increase as $NO_x$ emissions decrease. In the VOC-limited regions, more than 70 % reductions in $NO_x$ emissions alone are required to reduce surface $O_3$ concentrations. Reductions in 20 % VOC emissions alone lead to 11 % decreases in surface $O_3$ concentrations, and are effective in offsetting increased $O_3$ levels that would otherwise occur through decreased $NO_x$ emissions alone.

Subsequently, the evolution of tropospheric $O_3$ from the present day (2004-2014) to the future (2045-2055) under the shared socio-economic pathways (SSPs) is investigated to demonstrate the impacts of different climate and emissions on $O_3$ changes. In the context of climate change, changes in the tropospheric $O_3$ burden in the future can be largely explained by changes in $O_3$ precursor emissions. However, surface $O_3$ changes vary substantially by season in high-emission regions due to different seasonal $O_3$ sensitivity. VOC-limited areas are more extensive in winter (7 %) than in summer (3 %) across the globe. Reductions in $NO_x$ emissions are the key to transform $O_3$ production from a VOC- to $NO_x$-limited chemical environment, but will lead to increased $O_3$ concentrations in high-emission regions, and hence emission controls on VOC and methane ($CH_4$) are also necessary.

Lastly, a deep learning model is developed to demonstrate the feasibility of correcting surface $O_3$ biases in UKESM1, to identify key processes causing them, and to correct projections of future surface $O_3$. Temperature and related geographic variables latitude and month show the strongest relationship with $O_3$ biases. This indicates that $O_3$ biases are sensitive to temperature and suggests weakness in representation of temperature-sensitive physical or chemical processes. Photolysis rates are also shown to be important for $O_3$ biases likely due to uncertainties in cloud cover and insolation simulations.

Chemical species such as the hydroxyl radical, nitric acid and peroxyacyl nitrates show a clear relationship to $O_3$ biases, associated with uncertainties in emissions, chemical production and destruction, and deposition. Corrected seasonal $O_3$ changes are generally smaller than those simulated with UKESM1 in high-emission regions. This demonstrates that $O_3$ sensitivity to future emissions and climate in UKESM1 may be stronger than that in the real atmosphere. Given the uncertainty in simulating future ozone, we show that deep learning approaches can provide improved assessment of the impacts of climate and emission changes on future air quality, along with valuable information to guide future model development.

The work presented here offers a valuable assessment of emission control strategies to resolve current $O_3$ air pollution problems in China, and also quantifies the changes in the tropospheric $O_3$ burden and global surface $O_3$ sensitivity in the future under different emission and climate scenarios. Deep learning guides possible directions to improve model performance in surface $O_3$ simulations for a global chemistry-climate model, and provides more accurate projections of $O_3$ pollution in the future.

# Lay summary

Ozone is a reactive gas and protects life on the Earth by absorbing most of the harmful ultraviolet radiation from the sun in the upper atmosphere, the stratosphere, but is a pollutant in the lower atmosphere, the troposphere. Ozone is formed by a series of chemical reactions with the presence of sunlight and precursors such as nitrogen oxide and volatile organic compounds. While emissions of precursors have already been controlled in some polluted regions, severe ozone air pollution can still occur. This reflects the non-linear chemical reactions of ozone formation, which limits the effectiveness of emission controls. Ozone concentrations are also governed by meteorology, transport and deposition, and all of these factors are affected by climate change. It is hence important to understand the different impacts of emissions and climate on future ozone.

Firstly, a computational chemistry-climate model is used to simulate surface ozone concentrations in the main industrial regions of China where ozone polluted episodes occur frequently in recent years. The aim is to investigate the increased ozone concentrations in these regions, even though stringent controls on $NO_x$ and aerosol emissions have been implemented successfully in China. Another aim is to investigate the suitable emission control strategies to reduce ozone pollution. The results show that if only emissions of nitro-

gen oxide are reduced, more than 70 % emission reductions are required to reduce surface ozone concentrations in most high-emission regions in China; otherwise surface ozone levels increase. The 20 % reductions in emissions of volatile organic compounds reduce surface ozone concentrations by at most 11 %. The results highlight that emission controls on nitrogen oxide and volatile organic compounds should be implemented simultaneously, which can effectively offset high ozone levels in China.

Secondly, the evolution of global tropospheric ozone is investigated under changing emissions and climate in the future. The changes in the ozone burden are mainly attributed to changing surface emissions of ozone precursors. Methane, as an inactive volatile organic compound, also shows great importance to surface ozone levels. We show that the future tropospheric ozone burden will increase by 4 % with higher $NO_x$ and VOC emissions but decrease by 7 % if $NO_x$ and VOC emissions are reduced and by 5 % if atmospheric methane mixing ratios are reduced. Under a warmer climate, enhanced biogenic emissions of volatile organic compounds promote ozone production, but a more humid atmosphere accelerates ozone destruction. The seasonal changes in surface ozone levels vary substantially in different regions principally because ozone sensitivity varies by seasons and regions. Regional ozone sensitivity also changes in the future, indicating that emission control strategies should change correspondingly.

Lastly, a machine learning technique is used to correct model ozone biases due to the limitations of current models in representing processes governing ozone. The possible processes causing model biases are also explored. The results show that the ozone biases in a chemistry-climate model are highly related to temperature, reflected by positive biases in summer and negative biases in winter. The photolysis rates associated with ozone production and

destruction also affect $O_3$ biases greatly, likely due to the large uncertainties in the simulations of cloud coverage and insolation. Hydroxyl radical and oxidative nitrogen species such as nitric acid and peroxyacyl nitrates all show great importance to ozone biases on a regional scale. Due to uncertainty in simulating future $O_3$, surface $O_3$ projections are corrected by the machine learning model, showing the smaller effects of changes in climate and emission on $O_3$.

Overall, emissions of nitrogen oxide and volatile organic compounds are important factors for both surface ozone levels and the tropospheric ozone burden. Reducing these emissions will benefit the overall improvement of environment on a global scale, but will further lead to the degradation of air quality in some polluted regions, which depends on the regional ozone sensitivity. By correcting ozone biases in the model, an improved assessment of the impacts of changing climate and emissions on future air quality can be provided.

# Acknowledgements

I would like to thank my supervisors Prof. Ruth Doherty and Prof. Oliver Wild for leading me towards the right path for science exploration. This has been an ambitious and exciting journey, initiated by a common interest in atmospheric science, but with you both, I feel the strength of warmth beyond science, making everything that I have done deserved. Ruth always has a clear mind about what to do and when to do it, and has guided me in every step from beginning until the end of my Ph.D. Oliver has a rigorous attitude towards science, and always encourages me to think what the big and important scientific questions are. This helps expand my thoughts and persuades me to do unique things. I really appreciate you both for your patience, and massively instructive feedback on papers. What I have learned is beyond knowledge, and more about an approach to thinking in more depth. I have been always thinking what is the purpose of what we are doing and we are doing right or wrong? There may be no answers to these questions, but the process of seeking answers really matters and makes me feel peaceful and pleased. Thank you very much indeed for what I have earned, which will benefit me for my whole life.

I would also like to thank Fiona O'Connor and Steven Turnock for communications and guidance for my research, and valuable advice and reviews on

my papers. I also need to thank Michael Hollaway and Mohit Dalvi for help in implementing model developments and setting up model simulations. I would like to say thanks to Jamie Kelly and Sara Fenech for caring for me so much in our office, the Crew Attic, and I cannot forget every greeting in the morning, which made the first year of my Ph.D less boring. I thank Prof. Paul Palmer and Prof. Alex Archibald as my Ph.D examiners for providing insightful comments to further improve the thesis.

I would like to thank the scholarship from the China Scholarship Council and the University of Edinburgh for providing financial support, which I am proud of. I would like to thank all my friends in Edinburgh for valuable times we were together, making my life more colorful and enjoyable with countless times spent in chatting, food, hiking and board games.

Lastly, I would like to thank my dad and mum for endless support and love all the time. I love you forever. I also love those who love me in my life, including my beloved grandfather who passed away this year. All of you have made this Ph.D possible, and I express my great thanks here again.

# Contents

# Chapter 1

# Introduction

## 1.1 Motivation and aims

Tropospheric ozone ($O_3$) has significant impacts on air quality, ecosystems and climate hence there is much interest in its formation. $O_3$ is a secondary pollutant as it is formed through a series of chemical reactions in the presence of sunlight. Many factors affect $O_3$ concentrations, including emissions of precursors, meteorology, transport and deposition. While strict emission controls have been implemented in many polluted areas, high $O_3$ air pollution levels still occur frequently in these regions (Wang et al., 2017a). This is due to insufficient reductions in emissions but non-linear $O_3$ chemistry also limits the effectiveness of emission controls. Increases in background $O_3$ levels also worsen air quality if the local $O_3$ production does not decrease.

Many studies show that surface $O_3$ concentrations have generally decreased in North America and Europe since the 2000s due to consistent emission controls over the last decades (Simon et al., 2015; Colette et al., 2016). Meanwhile, major $O_3$ polluted regions have gradually shifted from North America and

Europe to Asia in recent years (Fleming et al., 2018). China has stringent emission controls, but surface $O_3$ pollution still occurs frequently in some regions (Li et al., 2019a,b). Therefore, there is a need to investigate the main cause of increased $O_3$ pollution in China, and effective emission control strategies for China. The effectiveness of emission controls may differ in different regions in China due to different chemical environments. The surface chemical environment is hence investigated for China to explore suitable emission control strategies to mitigate $O_3$ pollution.

Tropospheric $O_3$ concentrations will be influenced by a warmer climate by changing humidity and biogenic VOC emissions, but the tropospheric $O_3$ burden and surface $O_3$ concentrations may respond differently to changing climate and emissions in the future. Hence, there is a need to quantify the impacts of changes in climate and emissions on the $O_3$ burden and surface $O_3$ to understand the evolution of future $O_3$. Surface $O_3$ mitigation in the future in the context of climate change is still a concern. Therefore, surface $O_3$ sensitivity across the globe under different climate-emission scenarios is investigated to identify the key factors controlling $O_3$ sensitivity and suitable emission controls for different regions.

Current chemistry-climate models are imperfect in $O_3$ simulations, but it is difficult to identify the sources of biases in a complex model, which limits the assessment of future $O_3$ changes. Understanding biases in $O_3$ concentrations in model simulations is therefore important. A machine learning technique is hence used to identify key variables likely causing $O_3$ biases and to guide directions for model development. An improved assessment of future $O_3$ projections is also required to assess the real impacts of future climate and emissions on $O_3$ concentrations, which is important for understanding the relationships between air composition and climate in the Earth system.

Therefore, this thesis is aimed at investigating: suitable and effective emission control strategies to mitigate surface $O_3$ pollution in China, the evolution of tropospheric $O_3$ in the future, and the improvement of model performance in $O_3$ simulations and the implications for future $O_3$. The aims of the thesis are provided below, along with a brief introduction of the relevant research background.

1. To assess the effectiveness of emission control strategies in reducing $O_3$ levels in the industrial regions of China.

   Background: Anthropogenic emissions are believed to have decreased substantially in China since 2013 but surface $O_3$ pollution has become more severe in industrial regions.

2. To investigate the evolution of tropospheric $O_3$ from the present day to the future under different emission and climate scenarios.

   Background: The current climate is warming and regional emission changes in the future differ substantially across the globe, which have varying influences on the tropospheric $O_3$ burden and surface $O_3$ concentrations.

3. To quantify and correct $O_3$ biases in a chemistry-climate model and to explore potential reasons causing model biases.

   Background: Deficiencies in process representation in chemistry-climate models lead to biases in simulating surface $O_3$ concentrations and to

uncertainty in the projections of future $O_3$ changes.

The following sections in the introductory chapter introduce tropospheric $O_3$ in terms of $O_3$ impacts, chemistry, observations, and the pathways of future $O_3$ projection (Section 1.2). Then an Earth system model is introduced and the newly developed gas-phase chemistry scheme is described, which has been used throughout this thesis (Section 1.3). Subsequently, the origins of machine learning, its advantages and disadvantages, and its applications in atmospheric science are introduced (Section 1.4). The main research chapters are outlined in Section 1.5.

## 1.2 Tropospheric ozone

### 1.2.1 Ozone impacts and hazards

$O_3$ is a reactive trace gas in the atmosphere, with more than 90 % in the stratosphere, about 15-50 km above the surface, and the rest in the troposphere below the tropopause (Salawitch et al., 2019). Stratospheric $O_3$ protects life on the Earth by absorbing most of the Sun's harmful ultraviolet (UV) radiation. However, tropospheric $O_3$ is a photochemical pollutant, produced through the reactions between nitrogen oxide ($NO_x$), volatile organic compounds (VOCs) and carbon monoxide (CO) with the presence of sunlight (Fishman and Crutzen, 1978; Seinfeld and Pandis, 1998; Monks et al., 2015). Tropospheric $O_3$ has significant impacts on human health, ecosystems and climate change (Lefohn et al., 2018) as described below.

1. Human health

   Exposure to a high-$O_3$ environment will induce a variety of illnesses such as asthma, autism, strokes, respiratory diseases, cardiovascular diseases and Alzheimer's disease as well as premature mortality (WHO, 2021). In addition, $O_3$ affects metabolism and immune systems (Shore, 2019), and accelerates the aging of human beings (Fuks et al., 2019). The World Health Organization (WHO) air quality standard for outdoor 8-h maximum moving average (MDA8) $O_3$ concentrations is 100 $\mu g/m^3$. Both short-term and long-term exposures to $O_3$ above the standard concentrations can lead to morbidity and mortality caused by these diseases, which has been reported as a global issue by many studies (Lim et al., 2019; Zhang et al., 2019a; Vicedo-Cabrera et al.,

2020). Several studies estimate that more than 1 million deaths are attributed to $O_3$ pollution every year, especially in high-emission regions (Lelieveld et al., 2015; Stanaway et al., 2018).

2. Ecosystems

Ground level $O_3$ causes damage to vegetation, and influences ecosystems in terms of carbon cycling, nutrient cycling and water cycling (Mills et al., 2013; Grulke and Heath, 2020). Studies estimate that there was an economic loss of US $14–26 billion due to crop damage in the year 2000 (Emberson, 2020). Vegetation damage varies with different types of crops, which is estimated to be 2–16 % for major staple crops: wheat, rice, maize and soybean (Tai et al., 2021). Tree growth has also been reported to decrease by 7 % due to a 11 % reduction in photosynthesis of temperate and boreal forests in the Northern Hemisphere since the industrial revolution (Wittig et al., 2007). $O_3$ also poses a threat to terrestrial biodiversity by affecting physiological traits of insect and plant communities (Agathokleous et al., 2020).

3. Climate change

$O_3$ acts as an important greenhouse gas (GHG), absorbing infrared energy emitted by the Earth and heating the atmosphere. Mean $O_3$ radiative forcing to climate is estimated to be $0.4 \pm 0.2$ W/m$^2$ from the industrial era (around 1750) to the year 2000, which is comparable to radiative forcings from methane ($CH_4$) and halocarbons, but is much lower than that from carbon dioxide ($CO_2$) (Ehhalt et al., 2001; Naik

et al., 2021). In recent decades, stratospheric ozone concentrations have decreased due to rising reactive chlorine and bromine amounts in the atmosphere, leading to a small negative radiative forcing. However, the magnitude of negative radiative forcing is much smaller than positive radiative forcing exerted by increased tropospheric $O_3$ due to human activities, which demonstrates the importance of tropospheric $O_3$ to climate change. In addition, $O_3$ also influences the production of hydroxyl radical (OH), and indirectly affects the lifetime of $CH_4$. Furthermore, increased tropospheric $O_3$ reduces stomatal conductance and photosynthetic $CO_2$ uptake rates of plants and trees, leading to less $CO_2$ absorbed by vegetation and hence a warmer climate.

Tropospheric $O_3$ is a pollutant that influences human health, ecosystems and climate, and these aspects are also associated with each other. Human health and ecosystems will be further affected by a warmer climate due to more frequent heat stress and high $O_3$ episodes. Due to the positive feedback between different systems, the impacts of tropospheric $O_3$ on human and ecosystem health may be even larger than those estimated.

### 1.2.2 Ozone chemistry

Tropospheric $O_3$ is a secondary product, formed through a series of chemical reactions between $NO_x$, VOCs, $CH_4$ and CO (Chameides and Walker, 1973; Crutzen, 1974). The reactions are driven by energy from sunlight, so $O_3$ is a photochemical pollutant. The dominant mechanisms of $O_3$ formation vary between clean areas (e.g. remote oceans) and polluted areas (e.g. urban) due to the different abundances of $O_3$ precursors (Liu et al., 1987; Lin et al.,

1988; Kleinman, 1994). The balance between $O_3$ gross production and gross destruction is largely influenced by $NO_x$ concentrations, and increased concentrations of VOCs, $CH_4$ and CO generally accelerate $O_3$ production. $O_3$ formation mechanisms are described below in two conditions: clean regions and polluted regions.

**Clean regions:**

In clean areas with relatively low $NO_x$ emissions, the natural background $O_3$ concentrations are low, typically 25–40 ppb (Reid et al., 2008). $O_3$ formation starts from the photolysis of nitrogen dioxide ($NO_2$) (Equation 1.1), and $O(^3P)$ atoms created combine with oxygen ($O_2$) to form $O_3$ (Equation 1.2). $O_3$ can be destroyed quickly by reacting with nitric oxide (NO) to regenerate $NO_2$ (Equation 1.3). Therefore, $O_3$, $NO_2$ and NO create a closed $O_3$ production and destruction cycle, reflected by the stable concentrations of these species in a photochemical stationary state.

$$NO_2 + hv \rightarrow NO + O(^3P) \tag{1.1}$$

$$O(^3P) + O_2 + M \rightarrow O_3 + M \tag{1.2}$$

$$O_3 + NO \rightarrow NO_2 + O_2 \tag{1.3}$$

**Polluted regions:**

The photochemical stationary state between $O_3$, $NO_2$ and NO will not remain stable in polluted areas due to fast $O_3$ production and $O_3$ destruction affected by local $O_3$ precursor emissions. Instantaneous $O_3$ production rates are largely governed by $O_3$ precursor concentrations. $O_3$ production will be initialised by the oxidation of hydrocarbons (RH) or CO by reacting with reactive OH radicals to generate organic peroxy radicals ($RO_2$) and hydroperoxyl radicals ($HO_2$) (Equation 1.4, 1.5). Primary $O_3$ production rates are hence controlled by the concentrations of hydrocarbons, CO and OH.

$$RH + OH \rightarrow RO_2 + H_2O \tag{1.4}$$

$$CO + OH + M \rightarrow HO_2 + CO_2 + M \tag{1.5}$$

Next, the critical step is the conversion of NO to $NO_2$ (Equation 1.6, 1.7) through the reactions between NO and $RO_2$ radicals. These reactions avoid $O_3$ destruction by reaction with NO, and allow more $O_3$ production. $HO_2$ and OH can be also regenerated in these reactions, which will participate in further $O_3$ formation. In addition, generated secondary VOCs will react with OH or photolyse to generate more radicals to promote $O_3$ formation.

$$RO_2 + NO \rightarrow HO_2 + NO_2 + secondary\,VOC \tag{1.6}$$

$$HO_2 + NO \rightarrow OH + NO_2 \tag{1.7}$$

Therefore, peroxy radicals play important roles in initialising $O_3$ formation. Excited oxygen atoms $O(^1D)$ created by $O_3$ photolysis can be captured by water vapour, which is an important source of OH (Equation 1.8, 1.9).

$$O_3 + hv \rightarrow O(^1D) + O_2 \tag{1.8}$$

$$O(^1D) + H_2O \rightarrow 2OH \tag{1.9}$$

In addition, the reactions between NO and $HO_2$ produce OH (Equation 1.7). The OH and peroxyl radicals can convert with each other by reacting with $O_3$ (Equation 1.10, 1.11), and these reactions are chemical sinks of $O_3$.

$$O_3 + OH \rightarrow HO_2 + O_2 \tag{1.10}$$

$$O_3 + HO_2 \rightarrow OH + 2O_2 \tag{1.11}$$

In polluted areas, radical sources also include the photolysis of nitrous acid (HONO), formaldehyde (HCHO), and the ozonolysis of alkenes ($C_nH_{2n}$) (Equation 1.12, 1.13, 1.14).

$$HONO + hv \rightarrow OH + NO \tag{1.12}$$

$$HCHO + 2O_2 + hv \rightarrow 2HO_2 + CO \tag{1.13}$$

$$O_3 + Alkene \rightarrow HO_x + RO_2 \tag{1.14}$$

However, $O_3$ concentrations cannot increase continuously as $NO_x$, VOC and CO emissions increase. This is principally due to the rapid loss of radicals in

high-$NO_x$ environments. In low-$NO_x$ environments, major radical sinks are the formation of hydrogen peroxide ($H_2O_2$) and organic peroxide (ROOH) (Equation 1.15, 1.16). These two peroxide species are soluble, so some fractions of peroxides are removed from the atmosphere by wet deposition, and the rest can react with OH or photolyse to regenerate radicals again.

$$HO_2 + HO_2 \rightarrow H_2O_2 + O_2 \tag{1.15}$$

$$RO_2 + HO_2 \rightarrow ROOH + O_2 \tag{1.16}$$

However, in high-$NO_x$ environments, both OH and $NO_x$ can be consumed rapidly by the formation of nitric acid ($HNO_3$) (Equation 1.17), and a large amount of $O_3$ can be directly destroyed by reaction with NO. $HNO_3$ is also a highly soluble species that can be removed by wet deposition or by the formation of nitrate aerosol uptake by particles. Therefore, $HNO_3$ acts as a reservoir of both radicals and $NO_x$, and is more effective in terminating $O_3$ production than $H_2O_2$ and ROOH.

$$OH + NO_2 + M \rightarrow HNO_3 + M \tag{1.17}$$

Peroxyacyl nitrate (PAN) is also an important reservoir for $NO_x$ as it is formed by the reaction between $NO_2$ and the radical $CH_3C(O)O_2$ (Equation 1.18), and it could have a much longer lifetime (a few months) (Fischer et al., 2014) than $NO_x$ (a few hours). $CH_3C(O)O_2$ can be produced by oxidation of acetaldehyde ($CH_3CHO$) by OH, or by photolysis of other carbonyl VOCs. PAN can influence $O_3$ formation in remote areas by transporting $NO_x$ in a long distance before thermally decomposing. Overall, the balance between

$O_3$ production and $O_3$ destruction largely depends the losses of radicals, which are governed by the relative $NO_x$ concentrations.

$$CH_3(O)CO_2 + NO_2 + M \rightarrow PAN + M \tag{1.18}$$

At nighttime without sunlight, $O_3$ cannot be produced and is gradually consumed by NO. $O_3$ can react with $NO_2$ to form the nitrate radical ($NO_3$) (Equation 1.19), an important species at night because $NO_3$ is rapidly photolysed back to $NO_x$ during the day. $NO_3$ can rapidly react with NO to produce $NO_2$ again or react with other VOCs, but some $NO_3$ reacts with $NO_2$ to produce dinitrogen pentoxide ($N_2O_5$) (Equation 1.20). $N_2O_5$ acts as a minor sink of $O_3$ at nighttime, primarily lost by the reactions on aerosol surfaces before it is thermally decomposed, which forms $HNO_3$ (Equation 1.21).

$$O_3 + NO_2 \rightarrow NO_3 + O_2 \tag{1.19}$$

$$NO_3 + NO_2 \rightarrow N_2O_5 \tag{1.20}$$

$$N_2O_5 + H_2O \rightarrow 2HNO_3 \tag{1.21}$$

Based on the equations above, net $O_3$ chemical production rates can be expressed as the gross rate of $O_3$ production, $P(O_3)$, minus the gross rate of $O_3$ loss, $L(O_3)$. Given the small contribution of the minor chemical pathways of $O_3$ formation, a simple but useful approximation of net $O_3$ chemical

production rates is given as:

$$\begin{aligned} \text{Net tendency, } P(O_3) &= P(O_3) - L(O_3) \\ &= k_1[RO_2][NO] + k_2[HO_2][NO] \\ -(k_3[O(^1D)][H_2O] &+ k_4[O_3][OH] + k_5[O_3][HO_2] + k_6[O_3][Alkenes]) \end{aligned}$$

where $k_i$ represents the rate coefficient of reaction $i$, and species in the brackets represents the concentration.

### 1.2.3 Ozone sensitivity

Since $O_3$ production rates are not linearly proportional to changes in precursor concentrations, $O_3$ production efficiency varies, and this determines the effectiveness of emission controls in reducing $O_3$ pollution. $O_3$ sensitivity is hence an important concept associated with $O_3$ production efficiency, which can be characterised as '$NO_x$-limited' and 'VOC-limited' $O_3$ production (Sillman et al., 1990; Sillman, 1999; Kleinman et al., 2001). '$NO_x$-limited' regimes would turn into 'VOC-limited' regimes as the concentrations of $NO_x$ increase, leading to a decrease in $O_3$ production efficiency due to the removal of radicals through the formation of $H_2O_2$, ROOH and $HNO_3$ that can be removed by wet deposition. $NO_x$-limited regimes represent relatively low-$NO_x$ environments, in which $O_3$ concentrations increase with $NO_x$ emissions but are not sensitive to VOC emissions. In contrast, in VOC-limited regimes when $NO_x$ concentrations are relatively high, $O_3$ concentrations increase with decreasing $NO_x$ emissions, and are proportional to VOC increases. There are several factors influencing $O_3$ chemical sensitivity, including meteorology, transport, radiation and deposition. All these factors indirectly affect the instanta-

neous production rates of $O_3$ through temperature, photolysis rates and $O_3$ precursor concentrations. VOC reactivity also influences $O_3$ sensitivity as $O_3$ production could be very sensitive to reactive VOCs despite their low concentrations, leading to a '$NO_x$-limited' regime (Chameides et al., 1988; Pierce et al., 1998).

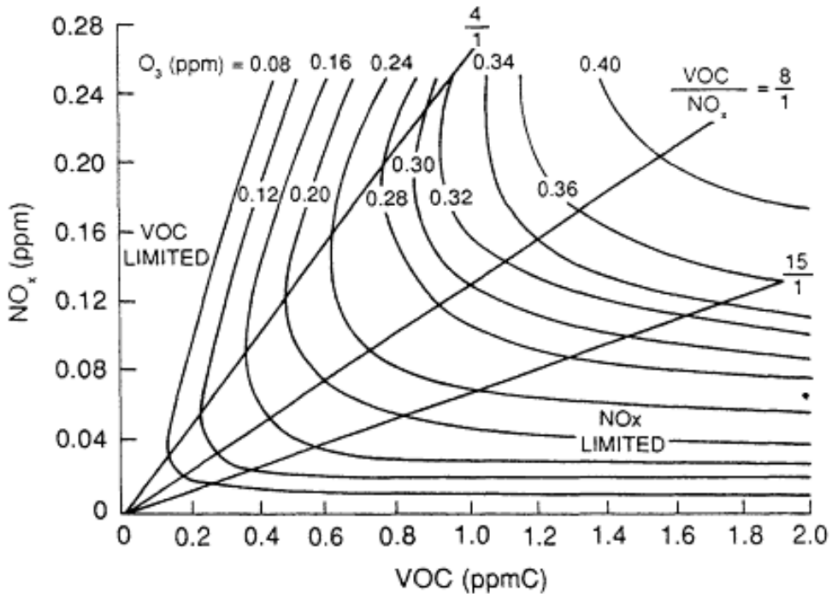


**Figure 1.1:** An example of an $O_3$ isopleth diagram showing $O_3$ concentrations as a function of VOC and $NO_x$ concentrations, and VOC- and $NO_x$-limited regimes for $O_3$ production. The picture is adapted from *Rethinking the Ozone Problem in Urban and Regional Air pollution*, National Research Council 1992.

$O_3$ sensitivity can be characterised with a variety of approaches based on observations or models. Observation-based approaches such as Incremental Reactivity (IR) (Carter and Atkinson, 1989) and Relative Incremental Reactivity (RIR) (Cardelino and Chameides, 1995) use in situ concentrations

of chemical species to calculate the instantaneous sensitivity of $O_3$ to precursors. However, limited observations cannot provide a general picture of $O_3$ sensitivity from a large scale. The model-based approach quantifies $O_3$ responses to emission changes, but this may be computationally intensive as $O_3$ responses can be only obtained for a specific emission scenario set so several model runs are needed. However, when the comprehensive relationships between $O_3$ concentrations and precursor emissions or concentrations are derived from models, there is a ridge on the $O_3$ isopleth plot distinguishing $NO_x$-limited and VOC-limited $O_3$ production regimes, as seen in Figure 1.1. However, $O_3$ sensitivity diagnosed by this $O_3$ isopleth method may not be accurate due to uncertainties and biases in simulated variables related to $O_3$ simulations. There are also uncertainties in emission inventory and chemistry schemes implemented in models (Sillman et al., 1997).

$O_3$ sensitivity indicators are an extension of the model-based approach, which allow to identify $O_3$ sensitivity regimes relatively easily. Two typical indicators are the ratio of $NO_x$/VOC concentrations or emissions and the ratio of $HNO_3/H_2O_2$ concentrations (Sillman, 1995; Sillman and He, 2002). Both indicators are useful in distinguishing $O_3$ sensitivity regimes but from different perspectives. $NO_x$/VOC ratios represent the relative abundances of $NO_x$ and VOCs, reflecting low- and high-$NO_x$ environments. In contrast, $HNO_3/H_2O_2$ ratios reflect the dominant radical sink, $HNO_3$ or $H_2O_2$, governed by high- and low-$NO_x$ concentrations separately. However, the poor representation of uptake of $HNO_3$ and radicals by aerosols in models may lead to biases in the determination of $O_3$ sensitivity regimes because the $HNO_3/H_2O_2$ indicator is more sensitive to chemistry schemes.

### 1.2.4 Ozone observations and satellite measurements

It is critical to establish $O_3$ observation networks to investigate the spatial distributions and temporal trends in $O_3$ concentrations, which provides opportunities to better understand $O_3$ chemistry and transport by evaluating model results against observations. The observed $O_3$ concentrations or column concentrations can be collected by satellite, aircraft, ozonesondes and ground based instruments. Satellite instruments measure the total $O_3$ column and provides some information of derived $O_3$ profiles. This is especially helpful to measure the total $O_3$ changes, and an example is the detection of the $O_3$ hole over the Antarctic (Levelt et al., 2018). Aircraft and ozonesonde data provide vertical profiles of $O_3$ and other related speices but these data are limited in time and space (Liu et al., 2013; Gaudel et al., 2018). Surface $O_3$ has the closest link to human health and ecosystem sustainability. Ground based instruments provide surface $O_3$ data, but they are sparsely distributed across different regions (Sofen et al., 2016). Current measurement sites are mostly located in developed regions. It is undoubtedly beneficial to investigate $O_3$ pollution in these specific regions, but the lack of $O_3$ observations in developing countries hinder a comprehensive understanding of $O_3$ pollution in more polluted environments and the underlying transport of $O_3$ across continents.

Most surface $O_3$ observation networks are developed on a regional basis. In North America, the United States Environmental Protection Agency Air Quality System (EPA AQS) is the main national network to monitor air quality under the Clean Air Act, consisting of 2,963 stations across America. The Canadian National Air Pollution Surveillance Program (NAPS) measure air quality from 373 stations in Canada. In Europe, the European

Environment Agency (EEA) AirBase is the largest air quality data provider, including 3,505 stations from 40 European countries. In East Asia, the National Institute for Environmental Studies (NIES) is in charge of air quality measurements from 1260 sites in Japan. The Korea Air Quality Network (KRAQN) provides data from 312 sites in Korea. The World Data Center for Greenhouse Gases (WDCGG) from the World Meteorological Organization (WMO) Global Atmospheric Watch (GAW) is an early international program that began to monitor reactive gas in 1971, but it only provides $O_3$ data from 155 stations mainly in developed countries (Schultz et al., 2015).

To integrate $O_3$ observation data from different sources, the Tropospheric Ozone Assessment Report (TOAR, https://toar-data.org/) was established in 2014, under the International Global Atmospheric Chemistry Project (IGAC). It provides a comprehensive assessment of tropospheric $O_3$ in terms of global distributions and the trends from surface to the tropopause, using 9,690 stations from 1970 to 2015 for research communities (Schultz et al., 2017). For surface $O_3$ data, the database can be accessed via the Jülich Open Web Services Interface (JOIN; https://join.fz-juelich.de). The processed monthly, seasonal, annual mean data, trend datasets and gridded datasets can be obtained in the data publication (https://doi.pangaea.de/10.1594/PANGAEA.876108).

While the TOAR database includes all available $O_3$ observations, there are still large areas without measurement sites such as South America, Africa and Asia. For China, there are only 34 stations (only 11 sites in the mainland China) included in the TOAR database. However, air quality in China is changing rapidly in recent years under emission controls, with the decreases in some pollutants but surface $O_3$ increases, which has drawn many scientific

concerns. The Chinese air quality monitoring network has been established since 2013 with initial 450 measurement stations, growing rapidly to 2,734 stations now. Hourly mean data can be accessed from the public website (https://quotsoft.net/air/) which mirrors data from the Chinese National Environmental Monitoring Centre (CNEMC).

### 1.2.5 Ozone in the past and for present day

Tropospheric $O_3$ concentrations have increased in recent decades mainly due to the increases in anthropogenic emissions and natural emissions of wildfires, BVOC and released $CH_4$ from wetlands caused by climate change. However, regional surface $O_3$ changes vary substantially due to anthropogenic emission changes associated with varying levels of industrialisation, urbanisation and socio-economic development in different countries (Lamarque et al., 2010; Hoesly et al., 2018). It has been estimated that human activities (emissions) account for 30 % of the present-day tropospheric $O_3$ burden (the total mass of $O_3$ in the troposphere) (Young et al., 2013). Multi-model mean results show that the $O_3$ burden for the year 2000 was 337 Tg, ranging from 302 to 378 Tg (Young et al., 2013). Over the period 1850–2010, the model results show that the $O_3$ burden increased by 45 %, from 247 $\pm$ 36 Tg to 356 $\pm$ 31 Tg (Griffiths et al., 2021). The simulated present-day $O_3$ burden is consistent with the estimates (336 $\pm$ 8 Tg) based on the TOAR observation data (Gaudel et al., 2018). The increases in the $O_3$ burden can be mainly explained by the growth of $O_3$ precursor emissions in the same period of time. The impacts of climate change on the $O_3$ burden are reflected by changing temperature, humidity, biogenic emissions, lightning and pollution transport patterns (Lin et al., 2015; Doherty et al., 2013, 2017). The $O_3$

burden generally decreases in a warmer climate mainly due to more $O_3$ destruction through water vapour, but surface $O_3$ concentrations may increase due to enhanced BVOC emissions, weaker transport of $O_3$ precursors and decomposition of PAN at higher temperatures (Liao et al., 2006; Fiore et al., 2015).

For the present-day surface $O_3$, high $O_3$ concentrations ($> 50$ ppb) are often found in the western USA, southern Europe, South Korea, Japan and China. However, starting from the 1950s, surface $O_3$ concentrations increased in most of the developed countries, reflecting their rapid growth of society and emissions (Cooper et al., 2014). After the 2000s, surface $O_3$ concentrations in North America and Europe decreased as anthropogenic emissions of $NO_x$, CO and VOCs decreased (Simon et al., 2015; Colette et al., 2016), and the main emission source regions have gradually shifted from North America and Europe to Asia. At the same time, $O_3$ concentrations remained stable in Japan and decreased in some areas but consistently increased in South Korea (Fleming et al., 2018), as seen in Figure 1.2. Surface $O_3$ levels are also observed to increase in China since 2013 when observation data are available (Lu et al., 2018a). For regions across the globe, the maximum $O_3$ concentrations are observed in spring or summer, and very high daytime ozone values ($> 80$ ppb) are widespread in Asia (Gaudel et al., 2018).

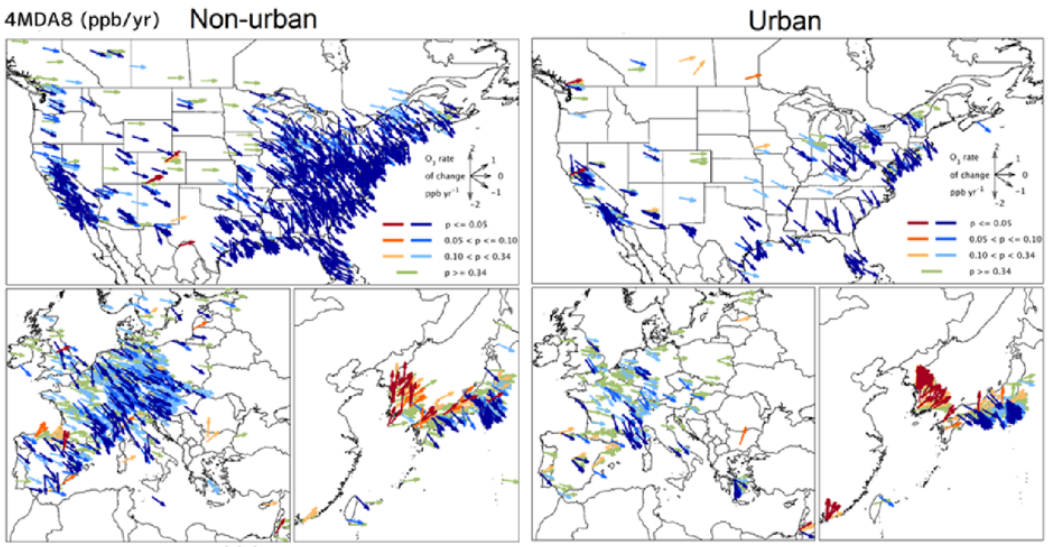


**Figure 1.2:** Urban and non-urban $O_3$ trends for the $4^{th}$ highest daily maximum 8-hour ozone (4MDA8; ppb/yr) for the 15-year period 2000-2014. The direction of arrows indicates the magnitude of the trend. Red and orange colours indicate increasing ozone levels and blue colours indicate decreasing ozone levels over time. The figure is adapted from Fleming et al. (2018).

In recent years in China, high $O_3$ episodes have been observed despite decreases in $O_3$ precursor emissions. Thus, many studies focused on the $O_3$ pollution issue in China. The studies show that the concentrations of fine particles ($PM_{2.5}$) in China had an overall decrease by 30–50 % from 2013 to 2018 (Zhang et al., 2019b; Zhai et al., 2021) due to strict controls on anthropogenic emissions, and this has greatly improved $PM_{2.5}$ air quality. However, annual mean surface MDA8 $O_3$ concentrations have increased with a growth rate of 5 % per year in recent years, especially in the industrial regions of China such as the North China Plain, the Yangtze River Delta, the Pearl River Delta and the Sichuan Basin, where the most stringent emission controls are implemented (Silver et al., 2018; Liu et al., 2020). There are still

ongoing debates about the principal cause leading to $O_3$ increases in China, including non-linear $O_3$ chemistry, meteorological impacts, and aerosol impacts on radical uptake and radiation strength (Wang et al., 2019; Hollaway et al., 2019; Li et al., 2019a; Liu and Wang, 2020). Uncertainty in emission inventories also leads to inaccurate assessments of surface $O_3$ changes in China. However, undoubtedly, the rapid but contrasting changes in $O_3$ and $PM_{2.5}$ concentrations are associated with the substantial emission changes in China, and emission controls are the only practical way to mitigate surface $O_3$ pollution. North America and Europe had some success in controlling surface $O_3$ air pollution by emission controls, and China seems to follow the way these countries did. The key question is what emission control strategies can maximise the effectiveness in reducing $O_3$ pollution with least economic costs.

### 1.2.6 Future climate projections

The current climate is changing and influences tropospheric $O_3$ in a variety of ways as discussed in the last section. Therefore, there is a need to predict future $O_3$ under climate change but with different trajectories of emissions to quantify $O_3$ changes, and to understand whether surface $O_3$ pollution can be controlled in the future. Representative Concentration Pathways (RCPs) provide such future climate and emission scenarios that are widely used and adopted by the fifth Assessment Report (AR5) of the Intergovernmental Panel on Climate Change (IPCC) in 2014. RCPs include time series data of emissions, concentrations of greenhouse gases and land use from the present day to 2100, to reflect future temperature changes represented by radiative forcings (Moss et al., 2008; Van Vuuren et al., 2011). There are four

original pathways - RCP2.6, RCP4.5, RCP6.0 and RCP8.5, and each value represents the targeted radiative forcings with W $m^{-2}$ units in the year 2100. All these pathways represent a warmer climate in the future with increased temperature ranging from about 2.0–4.3 °C from the pre-industrial level to 2100. RCP1.9 is an additional pathway added by the Paris Agreement to limit the global warming within 1.5 °C by the end of this century.

Unlike RCPs that simply consider climate change in a physical way based on greenhouse gases and other radiative forcers, Shared Socioeconomic Pathways (SSPs) account for population, economy, education, urbanisation and technology development to derive emission changes under different climate policies based on RCPs (O'Neill et al., 2014; Van Vuuren et al., 2014). They are the latest climate and emission future scenarios under the Coupled Model Intercomparison Projects Phase 6 (CMIP6), used for the IPCC sixth Assessment Report (AR6) in 2021 (IPCC, 2021). They describe five basic pathways - SSP1, SSP2, SSP3, SSP4 and SSP5 for future society development to achieve different radiative forcing targets, as shown in Fig. 1.3. These pathways represent different levels of challenges for mitigation and adaptation to climate change. Different pathways also have the targeted radiative forcings in 2100, so they are identified as SSP1-2.6, SSP2-4.5, SSP4-6.0 and SSP5-8.5 with similar radiative forcings as RCPs. However, they are distinguished from RCPs by different emission trajectories of greenhouse gases and other near-term climate forcers to represent different society development pathways. The new added SSPs include SSP1-1.9, SSP4-3.4, SSP5-3.4 and SSP3-7.0. SSP1-1.9 is the most optimistic pathway to limit the global warming below 1.5 °C by 2100 above the pre-industrial levels, but the target of net zero $CO_2$ emissions should be achieved around 2050. Different climate policies correspond to different emission mitigation pathways, influ-

encing both climate and surface $O_3$ in the future, which requires assessments to guide win-wins for climate and air quality.

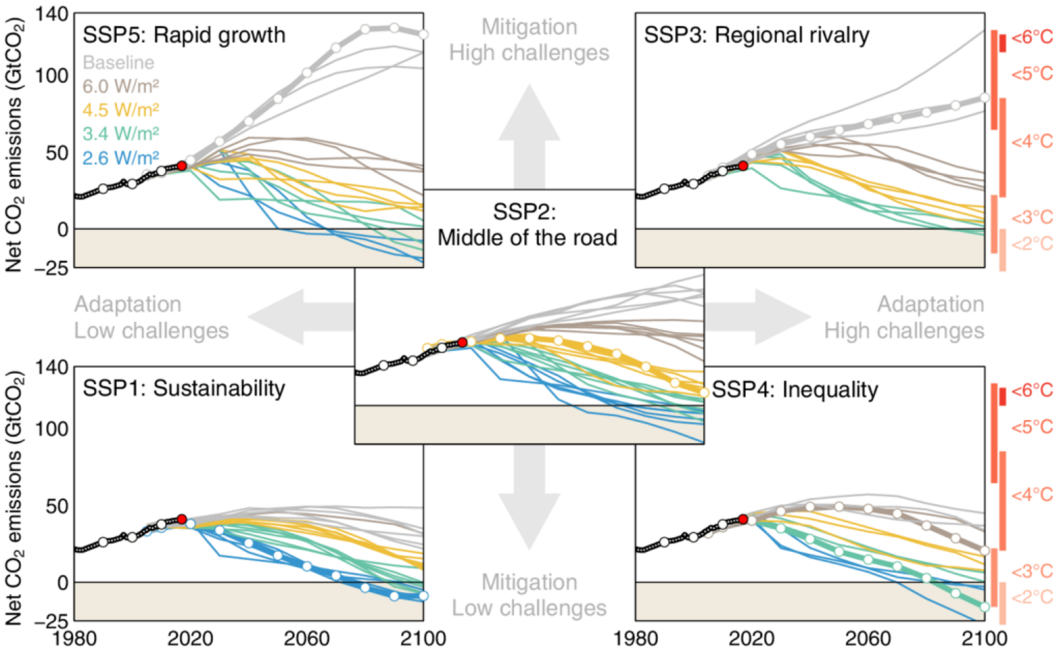


**Figure 1.3:** Global $CO_2$ emissions and potential temperature increases by 2100 relative to the pre-industrial level in the SSP database simulated by multi-model runs. SSP no-climate-policy baseline scenarios are shown grey, and SSP scenarios with various mitigation targets are shown in colour. Five basic pathways for future climate projections: SSP1, SSP2, SSP3, SSP4 and SSP5 are shown in each subplot. The figure is adapted from the Global Carbon Project, https://www.globalcarbonproject.org/.

## 1.3 Chemistry climate modelling

### 1.3.1 The United Kingdom Earth System Model

Computer models are used to simulate physical and chemical processes in the atmosphere, and there are two basic types used to represent atmospheric composition: chemistry transport models and chemistry climate models. Chemistry transport models are designed to focus on chemical processes in the atmosphere, so meteorological reanalysis data are normally used to provide reliable meteorological fields to drive chemistry. In chemistry climate models, meteorology can be simulated by dynamic modules to drive chemical processes. Chemistry climate models also account for the feedback of chemistry on meteorology and radiation, and include the interactive modules of atmospheric dynamic, chemistry, radiation transfer, aerosols, clouds, vegetation, ocean and sea ice, as seen in Figure 1.4.

The version 1 of United Kingdom Earth System Model (UKESM1) is a chemistry climate model that simulates atmospheric composition from the troposphere to the upper stratosphere (Sellar et al., 2019). UKESM1 consists of a physical climate model, the Hadley Centre Global Environment Model version (HadGEM3-GC3.1) (Kuhlbrodt et al., 2018; Williams et al., 2018), configured with the Global Atmosphere 7.1 and Global Land 7.0 (GA7.1/GL7.0) components (Walters et al., 2019) to which Earth System processes have been coupled. Atmospheric gas-phase composition and aerosols are modelled using a state-of-the-art chemistry and aerosol module, the United Kingdom Chemistry and Aerosol (UKCA) (Archibald et al., 2020b), including a stratosphere-troposphere gas-phase chemistry scheme (StratTrop). UKCA is coupled with the Fast-JX Photolysis scheme (Telford et al., 2013), and the Global Model of Aerosol Processes (GLOMAP) aerosol scheme (Mann et al., 2010; Mulcahy

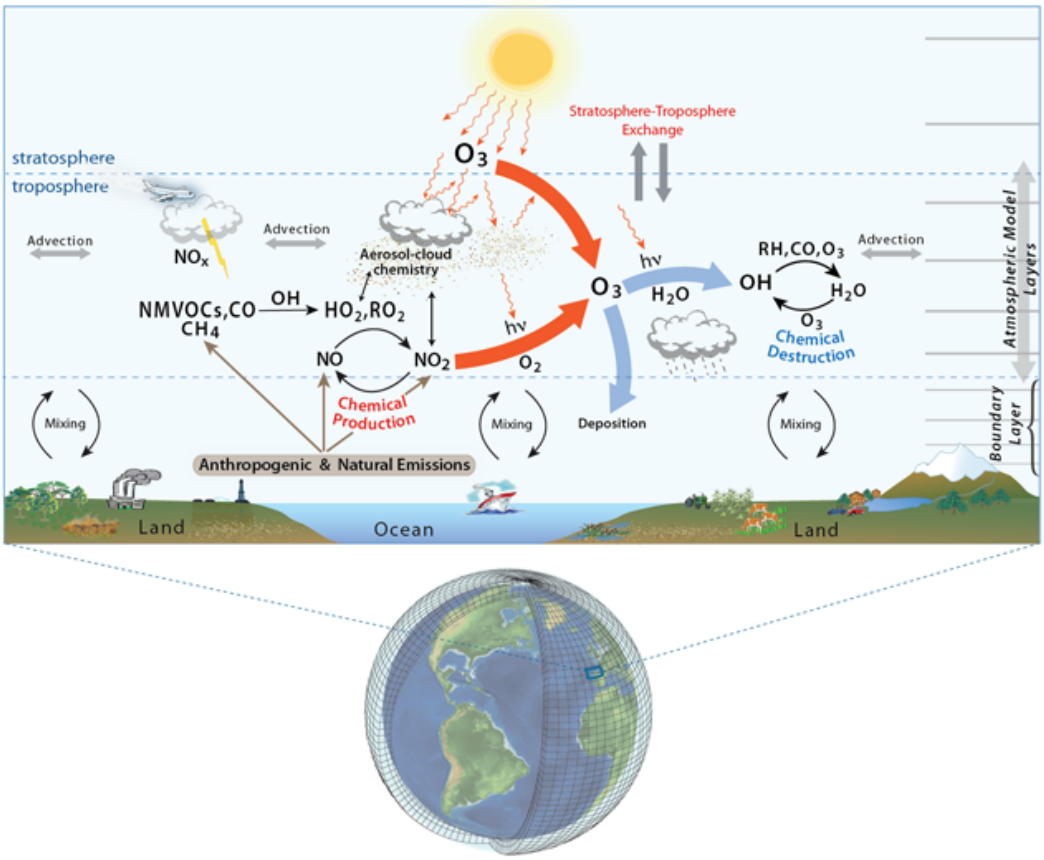


**Figure 1.4:** Schematic of chemical and physical processes included in a typical global chemistry model to simulate tropospheric ozone. The figure is adapted from Young et al. (2018b).

et al., 2020). The model resolution used in all studies here is N96L85 with 1.875° in longitude and 1.25° in latitude. UKESM1 has 85 terrain-following hybrid height layers and a model top at 85 km.

### 1.3.2 Developments for VOCs in the gas-phase chemistry scheme

The StratTrop gas-phase chemistry scheme in the UKCA is used to simulate the inorganic odd oxygen ($O_x$), hydrogen oxide radicals ($HO_x$ = OH + $HO_2$) and $NO_x$ chemical cycles; the oxidation of CO and VOCs; chlorine and bromine chemistry; and heterogeneous processes on polar stratospheric clouds and liquid sulfate aerosols. There are a total of 87 species and 305 reactions in the StratTrop scheme. 12 gas-phase species are treated as emitted tracers: NO, CO, sulfur dioxide ($SO_2$), HCHO, ethane ($C_2H_6$), propane ($C_3H_8$), acetaldehyde ($CH_3CHO$), acetone ($(CH_3)_2CO$), methanol ($CH_3OH$), isoprene ($C_5H_8$), monoterpene ($C_{10}H_{16}$) and dimethyl sulfide (DMS). Monoterpenes are not involved in chemical reactions in the chemistry scheme but contribute to the formation of secondary organic aerosols in the aerosol scheme.

The selection of a limited number of primary VOC species in the chemistry scheme means that $O_3$ formation is initiated by the oxidation of only 7 VOC species as well as CO and $CH_4$ in the StratTrop scheme. This is a typical approach to process thousands of VOC species and related reactions in chemistry climate models to reduce the computation burden. It is also sensible because these VOC species are representative of major primary VOCs in the atmosphere. Most of these VOC species are relatively long-lived and can be transported on a regional scale, which is suitable to investigate the overall spatial distributions of $O_3$ across the globe and the tropospheric $O_3$ burden. However, this may not be suitable to simulate the regional $O_3$ pollution in high-emission areas where large contributions from reactive VOCs lead to $O_3$ production.

High-emission regions normally occur in high-population areas such as the industrial regions of China, where $PM_{2.5}$ pollution has been reported to decrease substantially since 2013 but $O_3$ pollution becomes severe (section 1.2.5). Many studies show that more reactive VOCs such as alkenes and aromatics are important to $O_3$ production (Wu and Xie, 2017; Tan et al., 2019; Liu et al., 2020), but these species are not included in the StratTrop chemistry scheme. Therefore, for highly polluted regions, a more comprehensive chemistry scheme is needed to investigate the mechanism of $O_3$ formation. To address this, we incorporate propene ($C_3H_6$), butane ($C_4H_{10}$) and toluene ($C_7H_8$) into the StratTrop chemistry scheme to represent the more reactive VOC classes of alkenes, higher alkanes and aromatic compounds, respectively. The added chemical reactions and their rate coefficients are based on the atmospheric experimental study of Atkinson et al. (2006), and modelling studies of Folberth et al. (2006) and Monks et al. (2017). The incorporation of reactive VOCs permits a more realistic simulation of photochemically active environments and allows rapid $O_3$ formation in high-VOC-emission regions to be captured. 14 chemical species tracers and 43 chemical reactions are added. The improved chemistry scheme now includes 101 species, 244 bimolecular reactions, 26 bi- and termolecular reactions, 70 photolytic reactions, 5 heterogeneous reactions, and 3 aqueous-phase reactions for the sulfur cycle. The detailed information of added species, the properties of species and reactions are shown in the Table 1.1 and 1.2 below.

In addition to the developments in the chemistry scheme, diurnal and vertical profiles of emissions (Bieser et al., 2011; Mailler et al., 2013) are applied so that different emission sources have different diurnal and vertical variations. Accumulation of $O_3$ precursor emissions at the surface likely leads to excessive $O_3$ production or $O_3$ destruction especially at nighttime when boundary layer

mixing is weak. The incorporation of diurnal and vertical emission profiles is hence beneficial to investigate diurnal changes in surface $O_3$ concentrations as the contribution of emissions to $O_3$ formation varies in different time periods of a day. The original emissions are replaced by sectoral emissions from five sectors: industry, power plants, transport, residences and agriculture.

**Table 1.1:** Chemical species added and their properties in the StratTrop chemistry scheme. 'Dry' and 'wet' refer to deposition. 'Emitted' means emissions.

| No. | Species | Descriptions | Dry | Wet | Emitted |
|---|---|---|---|---|---|
| 1 | $C_3H_6$ | propene | No | No | Yes |
| 2 | PrpeOO | propyl peroxy radical | No | No | No |
| 3 | PrpeOOH | propyl hydroperoxide | Yes | Yes | No |
| 4 | $C_4H_{10}$ | butane | No | No | Yes |
| 5 | BtOO | butyl peroxy radical | No | No | No |
| 6 | BtOOH | butyl hydroperoxide | Yes | Yes | No |
| 7 | TOLUENE | aromatic | No | No | Yes |
| 8 | $AROMO_2$ | aryl peroxy radical | No | No | No |
| 9 | AROMOOH | aryl hydroperoxide | Yes | Yes | No |
| 10 | MEK | methyl ethyl ketone | No | No | No |
| 11 | $MEKO_2$ | peroxy radical from MEK | No | No | No |
| 12 | MEKOOH | hydroperoxide from MEK | Yes | Yes | No |
| 13 | MeCOCOMe | peroxy radical from MEKOOH | Yes | Yes | No |
| 14 | ORGNIT | organic nitrates | Yes | Yes | No |

**Table 1.2:** Chemical reactions added to the StratTrop chemistry scheme.

| No. | Reactions |
|---|---|
| Bimolecular reactions | |
| 1* | $C_3H_6 + O_3 \rightarrow HCHO + MeCHO + OH + HO_2$ |
| 2* | $C_3H_6 + O_3 \rightarrow EtOO + MGLY + CH_4 + CO$ |
| 3* | $C_3H_6 + O_3 \rightarrow MeOH + MeOO + HCOOH$ |
| 4 | $C_3H_6 + NO_3 \rightarrow ORGNIT$ |
| 5* | $PrpeOO + NO \rightarrow MeCHO + HCHO + HO_2 + NO_2$ |
| 6* | $PrpeOO + NO \rightarrow ORGNIT$ |
| 7 | $PrpeOO + HO_2 \rightarrow PrpeOOH$ |
| 8 | $PrpeOOH + OH \rightarrow PrpeOO + H_2O$ |
| 9 | $PrpeOOH + OH \rightarrow HACET + OH$ |
| 10 | $C_4H_{10} + OH \rightarrow BtOO + H_2O$ |
| 11* | $BtOO + NO \rightarrow NO_2 + MEK + HO_2 + EtOO$ |
| 12* | $BtOO + NO \rightarrow ORGNIT + MeCHO$ |
| 13 | $BtOO + HO_2 \rightarrow BtOOH$ |
| 14* | $BtOO + MeOO \rightarrow MEK + HCHO + HO_2 + MeCHO$ |
| 15* | $BtOO + MeOO \rightarrow MeOH + EtOO$ |
| 16 | $BtOOH + OH \rightarrow BtOO + MEK + OH + H_2O$ |
| 17 | $MEK + OH \rightarrow MEKO_2$ |
| 18 | $MEKO_2 + NO \rightarrow MeCHO + MeCO_3 + NO_2 + ORGNIT$ |
| 19 | $MEKO_2 + HO_2 \rightarrow MEKOOH$ |
| 20 | $MEKOOH + OH \rightarrow MeCOCOMe + OH + OH$ |
| 21 | $ORGNIT + OH \rightarrow MEK + NO_2 + H_2O$ |
| 22 | $TOLUENE + OH \rightarrow AROMO_2 + HO_2$ |
| 23* | $AROMO_2 + NO \rightarrow MGLY + NO_2 + MeCO_3 + CO$ |

**Table 1.2** – Continued.

| No. | Reactions |
|---|---|
| 24* | $AROMO_2 + NO \rightarrow HO_2$ |
| 25* | $AROMO_2 + NO_3 \rightarrow MGLY + NO_2 + MeCO_3 + CO$ |
| 26* | $AROMO_2 + NO_3 \rightarrow HO_2$ |
| 27 | $AROMO_2 + HO_2 \rightarrow AROMOOH$ |
| 28* | $AROMO_2 + MeOO \rightarrow MGLY + CO + MeCO_3 + MeOH$ |
| 29* | $AROMO_2 + MeOO \rightarrow HO_2 + HCHO$ |
| 30* | $AROMOOH + OH \rightarrow AROMO_2$ |
| 31* | $AROMOOH + OH \rightarrow OH + H_2O$ |
| 32* | $AROMOOH + OH \rightarrow MeCO_3 + CO + HO_2 + OH$ |
| Termolecular reactions | |
| 33 | $C_3H_6 + OH + M \rightarrow PrpeOO + M$ |
| Photolysis reactions | |
| 34* | $BtOOH + h\nu \rightarrow MEK + MEK + EtOO + MeCHO$ |
| 35* | $BtOOH + h\nu \rightarrow HO_2 + HO_2$ |
| 36* | $BtOOH + h\nu \rightarrow OH + OH + OH$ |
| 37 | $MEK + h\nu \rightarrow MeCO_3 + EtOO$ |
| 38 | $MeCOCOMe + h\nu \rightarrow MeCO_3 + MeCO_3$ |
| 39 | $MEKOOH + h\nu \rightarrow MeCO_3 + MeCHO + OH$ |
| 40* | $ORGNIT + h\nu \rightarrow MeCHO + ORGNIT$ |
| 41* | $ORGNIT + h\nu \rightarrow NO_2 + MEK + HO_2 + EtOO$ |
| 42* | $AROMOOH + h\nu \rightarrow MeCO_3 + AROMOOH$ |
| 43* | $AROMOOH + h\nu \rightarrow OH + Me_2CO + HO_2 + CO$ |

* Reactions are split between multiple lines.

## 1.4 Machine learning

### 1.4.1 Origins and developments in machine learning

Machine learning is an artificial intelligence technique which is a branch of computer science. Machine learning algorithms are aimed at learning relationships from data automatically, and applying the relationships to complete tasks or make predictions. The process of the automatic improvement of machine learning models is called model training. There are three basic machine learning training approaches: supervised learning, unsupervised learning and reinforcement learning. Supervised learning discovers relationships between pre-labelled data sets (i.e. labelled input and output), and evaluates model accuracy on training data to improve the model. Supervised learning is useful in classification and regression problems. However, not all data can be labelled correctly and some problems have no explicit answers or solutions. Unsupervised learning, in contrast, aims at discovering the inherent relationships of unlabelled data. Unsupervised learning hence can be applied in clustering, anomaly detection, association and autoencoders tasks. Some other tasks in reality are complex without explicit guidance but with a clear purpose, which fits reinforcement learning. Reinforcement learning introduces a reward mechanism in model training with the aim to maximise cumulative rewards by rewarding optimal actions towards goals. It shows great advantages in resolving problems in a complex environment such as training robotics, video games and the game of Go (Kober et al., 2013; Silver et al., 2016; Berner et al., 2019).

The concept of machine learning started in the 1950s, but practical models only appeared about 20 years later because the most important model training method, the mechanism of backpropagation was only investigated fully

until in the 1980s (Rumelhart et al., 1986). The original artificial neural network, one type of machine learning model, were composed of a few layers with variables, called neurons to mimic the structure of biological neurons that transfer biological signals (LeCun et al., 2015). Deep learning models are developed based on artificial neural networks, but they have deep layers with a large number of neurons that can be trained (Goodfellow et al., 2016). Each neuron is assigned with parameters or weights to be trained and updated to obtain the best model performance. Scientists had proved that this multilayer architecture can be trained through the backpropagation approach. Backpropagation refers to the updates of neuron weights to reduce model errors, according to the derivatives or gradients of an objective loss function to weights. The multilayer architecture laid the foundation for modern machine learning models.

There were still some challenges to the developments of machine learning. In the 1990s, neural networks and backpropagation were largely forsaken, because some machine learning communities argued that model training is infeasible and ineffective due to the lack of prior knowledge. The fact is that backpropagation was not always useful mainly because neuron weights cannot have effective updates. This is because loss function values could fluctuate around local low values so global low values cannot be found, leading to little change in loss function values and hence small updates in neuron weights. This phenomenon is called gradient diminishing. However, many theoretical studies later showed that trapping in a local minimum is not a serious issue because it can be effectively resolved by incorporating activation functions in models.

Backpropagation is the key to machine learning models. Many other types of main-stream models have different architectures. These models include

convolutional neural networks (CNN) (LeCun et al., 1989), recurrent neural networks (RNN) (El Hihi and Bengio, 1996), long short-term memory networks (LSTM) (Hochreiter and Schmidhuber, 1997) and the recent Transformer model that adopts the mechanism of attention (Vaswani et al., 2017). They have been developed for different fields such as speech recognition, computer vision, natural language processing, machine translation, bioinformatics, drug discovery, recommendation systems and computer games (Hinton et al., 2012; Sutskever et al., 2014). A CNN model won the ImageNet competition with a high accuracy of recognising 1,000 different classes from a million images in 2012 (Krizhevsky et al., 2012), and after that machine learning has started developing quickly in many domains.

Despite the broad applications of machine learning, there are potential issues and the major one is that machine learning models are 'black box' models due to the lack of interpretation in their results. It is difficult to understand why some good model results are generated, and to guarantee good model performance in different conditions. Apart from good model results, some problematic results also cannot be explained such as classifying unrecognisable images to a familiar category (Nguyen et al., 2015). This is particularly dangerous when machine learning techniques are applied to fields impacting human health such as automatic self-driving. Machine learning models have advantages in finding relationships from a large volume of data, but causality in data may not be captured. However, machine learning provides a unique way to resolve problems that people are not capable of at the moment such as understanding relationships between massive data.

### 1.4.2 Applications of machine learning in atmospheric science

In scientific fields, machine learning models can behave better than traditional models because of poorly constrained parameterisations and large uncertainty in how model processes are represented. Machine learning hence provides opportunities and solutions in investigating and resolving scientific problems. Many scientific problems in atmospheric science are constrained by limited observations and hence poor parameterisation of physical and chemical processes. While atmospheric science is built on solid physical and chemical theories expressed in a mathematical way, this does not mean that all details of physical and chemical processes happening in the atmosphere are known by scientists. In addition, it is not realistic to simulate all processes with atmospheric process-based models due to the heavy computational burden. Comprehensive scientific knowledge is also constrained to limited observations. Some processes are highly parameterised in atmospheric models, leading to errors in simulations. Machine learning has advantages in finding relationships from data and hence can replace those uncertain processes in atmospheric models. Given the capabilities of atmospheric models in predicting climate, weather and air pollution, the atmospheric model performance can be hopefully further improved with the aid of machine learning.

A sensible way to improve the performance of atmospheric models is to integrate machine learning models as modules into process-based models, called hybrid models (Schultz et al., 2021). A common usage of machine learning in atmospheric science is to predict precipitation. Machine learning models, with radar and satellite data as inputs, have potentials to achieve better results compared with Numerical Weather Prediction (NWP) models, in terms

of model accuracy, spatial resolution and forecasting leading time in precipitation forecasts (Sønderby et al., 2020; Ayzel et al., 2020; Ravuri et al., 2021). Air pollution can be also predicted with machine learning models, which can directly use observational meteorological and pollutant data as inputs (Alléon et al., 2020; Kleinert et al., 2021). There are errors in simulated concentrations of air pollutants, but it is difficult to identify the sources causing these errors. Some studies hence focus on error corrections for processed-based models (Ivatt and Evans, 2020; Keller et al., 2021). Machine learning is also used to assimilate observations and multi-atmospheric-model results to generate more accurate predictions for the future (e.g. surface $O_3$) (Sun and Archibald, 2021). Modules in atmospheric models can be also replaced independently by machine learning models for less computation costs and more effective parameterisations. The chemical solvers for ordinary differential equations (Keller and Evans, 2019) in chemistry transport models and the dynamic solvers for partial differential equations (Han et al., 2018) in meteorological models, and parameterising subgrid processes for clouds in climate models (Rasp et al., 2018) were all tried to be replaced by machine learning. The types and architectures of machine learning models used in these studies vary substantially because there are no explicit rules of model selections.

Tropospheric $O_3$ is influenced by emissions and climate, and there is large uncertainty in the projections of future $O_3$. Relatively accurate $O_3$ predictions could be derived from machine learning models, which allow more accurate assessments of the impacts of future emissions and climate on tropospheric $O_3$. However, the lack of interpretation for machine learning results are also reflected in the applications in atmospheric science. Especially when directly using observation data as inputs to implement predictions, model results can

be relatively accurate but this is not beneficial for understanding science because weaknesses in representing physical or chemical processes in atmospheric models are still unknown. However, by investigating the relationships between $O_3$ biases and related variables by machine learning, it is possible to identify the key variables that have high importance to biases, which will be useful to guide potential directions for model development. Given large uncertainties in simulating surface $O_3$ concentrations with a global chemistry climate model, $O_3$ bias correction permits more accurate assessments of future $O_3$ evolution, and this helps quantify the real impacts of changing climate and emissions on surface $O_3$.

## 1.5 Outline of the thesis

The main research chapters of this thesis are presented from Chapters 2 to 4, demonstrating suitable emission control strategies in China, tropospheric $O_3$ evolution in the future and surface $O_3$ bias correction to resolve research aims. A brief summary of each chapter is given below. Conclusions are given in Chapter 5, including section 5.3 which provides a 'synthesis of research findings' to address the aims of this thesis.

**Chapter 2: Contrasting chemical environments in summertime for atmospheric ozone across major Chinese industrial regions: the effectiveness of emission control strategies**

The UKESM1 chemistry-climate model is used to quantify the differences in chemical environment for surface $O_3$ for six major industrial regions across China in summer 2016. First, the gas-phase chemistry scheme is extended by incorporating reactive VOC tracers that are necessary to represent urban and regional-scale $O_3$ photochemistry. The model with the improved chemistry scheme demonstrates the capability in capturing the observed magnitudes and diurnal patterns of surface $O_3$ concentrations across these regions. $O_3$ response surfaces for each region are constructed by changing $NO_x$ and VOC emissions to contrast the effectiveness of measures to reduce surface $O_3$ concentrations. The $O_3$ responses to changing emissions in highly populated regions in other parts of the world are further investigated to be compared with the regions in China. The work provides an assessment of the effectiveness of emission control strategies to mitigate surface $O_3$ pollution in major Chinese industrial regions.

**Chapter 3: Tropospheric ozone changes and ozone sensitivity from present-day to future under shared socio-economic pathways**

Tropospheric $O_3$ is important for future air quality and climate. Tropospheric $O_3$ changes and $O_3$ sensitivity to changing emissions in the context of climate change from the present day to the future under a range of shared socio-economic pathways (SSPs) are investigated. The UKESM1 is applied with an extended chemistry scheme including more reactive VOCs to quantify $O_3$ burdens as well as $O_3$ sensitivities globally and regionally based on $NO_x$ and VOC concentrations. Surface $O_3$ changes are investigated in different seasons in high-emission regions under future pathways. Dominant VOC-limited regions in the present day and in the future are also identified. The work highlights that reductions in $NO_x$ emissions are required to transform $O_3$ production from VOC- to $NO_x$-limitation, and that emission controls on VOC and $CH_4$ are necessary to improve $O_3$ air quality in the future.

**Chapter 4: Correcting ozone biases in a global chemistry-climate model: implications for future ozone**

Weaknesses in process representation in chemistry-climate models leads to biases in simulating surface $O_3$ and to uncertainty in projections of future $O_3$ change. A deep machine learning model is developed to demonstrate the feasibility of correcting surface $O_3$ biases in the UKESM1, to identify key factors such as meteorology or emissions causing these $O_3$ biases, and to correct projections of future $O_3$. The projections of future $O_3$ under SSPs are hence corrected. The work shows that the deep learning model provides a valuable approach to correcting the chemistry-climate model and provides

an improved assessment of the impacts of climate and emission changes on future $O_3$ air quality.

# Chapter 2

# Contrasting chemical environments in summertime for atmospheric ozone across major Chinese industrial regions: the effectiveness of emission control strategies

This chapter has been published in the open-access journal Atmospheric Chemistry and Physics (ACP), available online from https://doi.org/10.5194/acp-21-10689-2021. The work has been implemented in collaboration with Prof. Ruth Doherty, Prof. Oliver Wild, Dr. Michael Hollaway and Dr. Fiona O'Connor. ZL, RD and OW designed the study. ZL, MH and FO'C set up the model. ZL ran model simulations and performed the analysis. ZL, RD

and OW prepared the paper with contributions from all co-authors.

## 2.1 Introduction

Surface ozone ($O_3$) has become the main cause of atmospheric pollution in the summertime in China since 2013 and is particularly severe in industrial areas of China such as the North China Plain (NCP), the Yangtze River Delta (YRD), the Pearl River Delta (PRD) and the Sichuan Basin where precursor emissions are high (Li et al., 2019a). The 90th percentile of the maximum daily 8 h average (MDA8) $O_3$ concentration in 30 of 74 Chinese cities exceeded the National Ambient Air Quality Standard (100 ppb) in the summer of 2017 (Wang et al., 2017b; Lu et al., 2018a; Silver et al., 2018; Li et al., 2019b; Lu et al., 2019). During 2013–2017, the national Air Pollution Prevention and Control Action Plan successfully reduced emissions of fine particulate matter ($PM_{2.5}$) and nitrogen oxides ($NO_x = NO + NO_2$) in China by 33 % and 21 %, respectively (Zheng et al., 2018). However, the reduction in $NO_x$ emissions has led to an increase in $O_3$ levels in polluted areas due to the non-linear chemistry of $O_3$ and reduced titration of $O_3$ by NO (Li et al., 2019a; Wang et al., 2019). Volatile organic compounds (VOCs) are also important $O_3$ precursors, and emissions of these have increased across China as a whole over the same period, exacerbating $O_3$ pollution (Zheng et al., 2018). VOC emissions are believed to have decreased in megacity regions such as Beijing (Cheng et al., 2019), but the resulting $O_3$ decrease is likely to have been offset by the $O_3$ increase due to reduced $NO_x$ emissions. This poses a challenge to mitigate surface $O_3$ pollution. Therefore, the balance of emission controls on $NO_x$ and VOC is critical to decreasing $O_3$ levels in these regions. Meteorological processes also affect $O_3$ formation through

temperature, humidity, clouds, precipitation and biogenic emissions, and a number of papers have studied meteorological impacts on $O_3$ over China (Gong and Liao, 2019; Liu and Wang, 2020; Shi et al., 2020). However, emission controls are the primary strategies used to reduce $O_3$ pollution, and we focus on these for this study, as their effectiveness for different regions has not been fully investigated.

$O_3$ is a secondary photochemical pollutant in the troposphere that can be produced rapidly through oxidation of its precursors $NO_x$, VOCs and carbon monoxide (CO) in the presence of sunlight. Power plants, industry, households and transport are the main anthropogenic sources of $NO_x$ and VOC emissions (Monks et al., 2015; Li et al., 2017). Isoprene is the principal biogenic VOC and is released from trees, plants and crops (Sindelarova et al., 2014). $O_3$ formation is mainly initiated through oxidation of VOC species by hydroxyl radicals (OH). The resulting organic peroxy radicals ($RO_2$) and hydroperoxyl radicals ($HO_2$) can convert NO to $NO_2$ without destroying $O_3$. $O_3$ is then created from the combination of $O(^3P)$ atoms, formed from photolysis of the resulting $NO_2$ and oxygen ($O_2$) (Sillman et al., 1990; Von Schneidemesser et al., 2015; Wang et al., 2017b). Under low-$NO_x$ conditions, $HO_2$ radicals may react with themselves or $RO_2$ radicals to produce hydrogen peroxide ($H_2O_2$) and organic peroxide (ROOH), respectively. However, at high $NO_x$ concentrations, nitric acid ($HNO_3$), peroxy nitrates ($RO_2NO_2$) and organic nitrates ($RONO_2$) are more easily formed as $NO_x$ reacts with OH and $RO_2$. These species are the main sinks of radicals and $NO_x$ and are readily removed from the atmosphere by deposition or exported to remote areas (Horowitz et al., 1998). Therefore, increasing $NO_x$ concentrations increase $O_3$ production but also accelerate the formation of $NO_x$ sinks, leading to less efficient $O_3$ formation. In addition, direct titration of $O_3$ by

NO becomes increasingly important at higher levels of $NO_x$. There is hence a transition in the magnitude of $O_3$ production from low- to high-$NO_x$ conditions. This turnover is dependent on the local chemical environment and in particular on the relative abundance of $NO_x$ and VOCs (Sillman, 1995; Kleinman et al., 1997; Thornton et al., 2002; Kleinman et al., 2005; Sillman and West, 2009).

A variety of $O_3$ sensitivity indicators have been proposed to characterise the $O_3$ response to changing precursor emissions. The simplest of these are based on the concentration ratios of the precursors, $NO_x$ / VOCs, or of their oxidation products, $H_2O_2$ / $HNO_3$ (Sillman, 1995). $O_3$ concentrations increase with $NO_x$ emissions and are not sensitive to VOC emissions in a $NO_x$-limited regime when $NO_x$ concentrations are relatively low (Sillman et al., 1990). However, in a VOC-limited regime, $O_3$ levels may increase with decreasing $NO_x$ emissions, which is common in urban areas with high $NO_x$ emissions, and this is reflected in high $NO_x$ / VOC or low $H_2O_2$ / $HNO_3$ ratios. Critical values of these indicators of $O_3$ sensitivity vary by region and by season (Sillman, 1995; Liu et al., 2010; Xing et al., 2019). Most major industrial regions in China are believed to be VOC limited, and rural areas are $NO_x$ limited or in a transition regime (Jin and Holloway, 2015; Wang et al., 2017b). $O_3$ production efficiency (OPE) is another important metric to evaluate the impacts of $NO_x$ emissions on $O_3$ concentrations (Liu et al., 1987; Kleinman et al., 2002). This is defined as the number of $O_3$ molecules produced per molecule of $NO_x$ oxidised. Low OPE values are typically associated with high-$NO_x$ conditions and indicate that there is less $O_3$ produced from a given amount of $NO_x$. OPE values generally increase as $NO_x$ emissions decrease, reflecting greater $O_3$ production per molecule of $NO_x$ oxidised at lower $NO_x$ levels.

In this study, we develop new capabilities in a global-scale model by incorporating higher-VOC chemistry, allowing the model to represent the oxidation environment in major industrialised regions in China. We focus on the spatial and temporal variation of daytime $O_3$ in this study. We first evaluate the performance of this global chemistry–climate model in simulating regional $O_3$ across large industrialised regions. We use $O_3$ sensitivity indicators to compare and contrast the chemical oxidative environment across these different regions in China to identify emission control measures that would be most beneficial to reduce $O_3$ pollution levels. Using a global model novelly allows us to compare the impact of emission control measures in China with those in other major industrialised regions across the world. The value of this approach is that the same model set-up can be used to assess the impact of future emission and climate scenarios, studies of tropospheric and stratospheric $O_3$ influences, and comparisons of $O_3$ in different parts of world.

The configuration of the model used in this study is described in Sect. 2.2, along with its development and application to surface $O_3$ in China. We evaluate the model performance in reproducing the diurnal cycles of surface $O_3$ and $NO_2$ in Sect. 2.3, and we investigate the $O_3$ chemical environment in China, including $O_3$ precursor concentrations and sensitivity ratios in Sect. 2.4. We calculate the local $O_3$ production rates, $O_3$ loss rates, $NO_x$ loss rates and OPE in Sect. 2.5. We then quantify the $O_3$ responses to changing $NO_x$ and VOC emissions in these regions and investigate the requirements of emission controls to reduce $O_3$ levels in each region in Sects. 2.6 and 2.7. To provide a global context we compare and contrast the effectiveness of emission control strategies with that in other parts of the world in Sect. 2.7 and present our conclusions in Sect. 2.8.

## 2.2 Materials and methods

### 2.2.1 Model description, development and application

The chemistry-climate model, UKESM1 is used in this chapter. Model description and development are fully introduced in section 1.3. Only necessary information of the model set-up and the model application for this chapter is described below. Wind speed and temperature are nudged with ERA-Interim reanalyses from the European Centre for Medium-Range Weather Forecasts (ECMWF) every 6 h (Dee et al., 2011). Sea surface temperature and sea ice fields are prescribed with the climatology mean of 1995–2004 (Reynolds et al., 2007).

We perform model simulations for 2016 and focus our results on summer (June–July–August, JJA). We spin up the model for 4 months and then simulate the full year nudged with ERA-Interim reanalysis data for 2016. The new capabilities of the model allow us to investigate regional $O_3$ chemical environment in industrial regions of China in the model. The relatively coarse resolution of the model may lead to biases in surface $O_3$ associated with numerical diffusion (Wild and Prather, 2006; Stock et al., 2014; Fenech et al., 2018; Mertens et al., 2020), but we note that the lifetime of $O_3$ makes it a regional-scale pollutant except very close to high-emission sources (Valari and Menut, 2008; Hodnebrog et al., 2011; Biggart et al., 2020). This study demonstrates the first application of this improved chemistry scheme to high-emission regions worldwide and lays the foundation for more detailed studies of the interactions between air quality and climate in a global chemistry–climate model under future scenarios.

### 2.2.2 Emissions

The anthropogenic emission inventory of Hemispheric Transport of Air Pollution (HTAP) for 2010 is used for the globe outside China (Janssens-Maenhout et al., 2015). The Multi-resolution Emission Inventory for China (MEIC) is used to provide emissions over China for 2013 (Li et al., 2017). We apply independent diurnal and vertical profiles to each emission sector (industry, power plants, transport and residences) according to European Monitoring and Evaluation Programme (EMEP) emissions (Bieser et al., 2011; Mailler et al., 2013). Biogenic VOC (BVOC) emissions are calculated interactively through the Joint UK Land Environment Simulator (JULES) land-surface scheme in UKCA (Pacifico et al., 2011). The Global Fire Emissions Database (GFED4) is used for biomass burning emissions (Van der Werf et al., 2010). Other natural aspects of the emissions used are as described in Archibald et al. (2020b).

Given the rapid changes in anthropogenic emissions across China, we adjust $NO_x$, VOCs, CO, sulfur dioxide ($SO_2$), black carbon (BC) and organic carbon (OC) emissions in MEIC from 2013 to 2016 by applying national and urban emission scaling factors. $NO_x$ emissions decreased by 18.8 %, and VOC emissions increased slightly by 1.1 % between 2013 and 2016 across China (Zheng et al., 2018). However, $NO_x$ and VOC emissions are estimated to have decreased by 24.2 % and 12.8 % respectively in Beijing and surrounding areas between 2013 and 2016 (Cheng et al., 2019). Given the tighter emission controls in the developed urban regions, we apply the Beijing scaling factors to major industrialised regions, and use national scaling factors across the rest of the country.

### 2.2.3 Selected regions and observations

We focus on six heavily populated regions with high emissions within the major industrialised regions in China. These include Beijing and Shijiazhuang on the North China Plain (32–40° N, 114–121° E), Shanghai and Nanjing in the Yangtze River Delta (28–33° N, 118–123° E), Guangzhou in the Pearl River Delta (21–25° N, 111–115° E), and Chongqing in the Sichuan Basin (28–32° N, 103–108° E); see Fig. 2.1. Anthropogenic $NO_x$ and VOC emissions are high in these regions (Fig. 2.2) due to rapid industrialisation, urbanisation and socio-economic development. Model grid cells that include observation stations located in each of the urban and rural regions are selected to be representative of these regions; see Table 2.1. For comparison with observations, we calculate a grid-weighted mean according to the number of measurement sites in each model grid cell for the region.

We use observed hourly concentrations of air pollutants including $O_3$ and $NO_2$ from the surface monitoring networks of China, obtained from the public website https://quotsoft.net/air/, which mirrors data from the Chinese National Environmental Monitoring Centre (CNEMC) http://www.cnemc.cn/. A total of 450 measurement stations in China started operating in 2013, growing rapidly to 1670 stations by 2019.

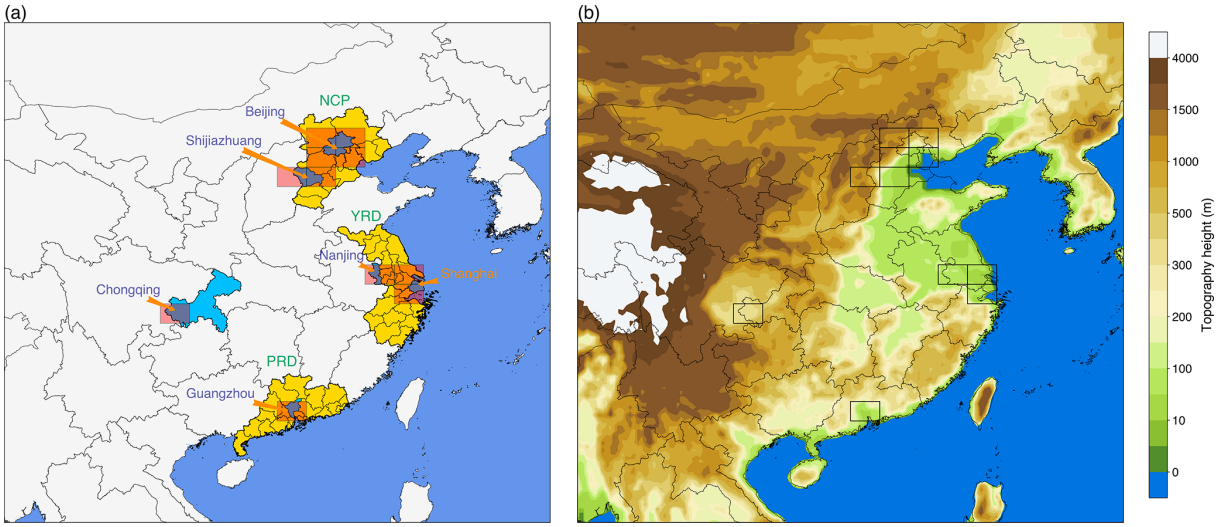


**Figure 2.1:** Map of China showing **(a)** the key provinces (yellow) representing the NCP, the YRD, and the PRD and locations of the six regions (blue) – Beijing, Shijiazhuang, Shanghai, Nanjing, Guangzhou and Chongqing – and UKCA model grid cells co-located with these regions (red); and **(b)** elevations across the whole of China.

**Table 2.1:** Number of measurement sites and grid cells in the six industrial regions.

| Region | No. of measurement sites | No. of grid cells |
|---|---|---|
| Beijing | 46 | 4 |
| Shijiazhuang | 28 | 2 |
| Shanghai | 58 | 2 |
| Nanjing | 45 | 1 |
| Guangzhou | 45 | 1 |
| Chongqing | 25 | 1 |

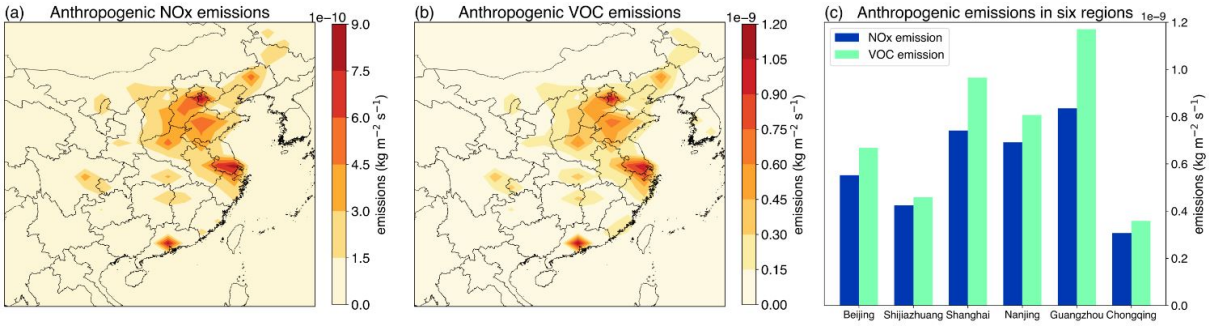


**Figure 2.2:** Spatial distributions of anthropogenic $NO_x$ and VOC emissions ($kg\,m^{-2}\,s^{-1}$) across China **(a, b)** and grid-weighted averaged emissions for the six regions within the four major industrialised regions **(c)** in JJA, 2016.

## 2.3 Model evaluation of surface $O_3$ and $NO_2$

We evaluate the diurnal variation in simulated surface $O_3$ and $NO_2$ concentrations against summertime observations for JJA, 2016, for the six industrialised regions (Figs. 2.3, 2.4). In general, the diurnal variation of observed $O_3$ is matched relatively well, and the correlation coefficients are relatively high; see Table 2.2. Mean concentrations for $O_3$ and $NO_2$ over the lowest three model layers (from the surface up to 130 m) are also compared with observations to investigate boundary mixing effects on pollutants. In the daytime, differences between the surface and three lowest layers are small due to efficient mixing in the planetary boundary layer (PBL). The height of the nocturnal PBL is typically underestimated in the model (Stock et al., 2014), leading to overestimated $NO_x$ concentrations and hence underestimated $O_3$ concentrations at nighttime due to excessive $O_3$ titration by NO (André et al., 1978; Petersen et al., 2019; Zhao et al., 2019). Figure 2.3a

shows a large difference in nighttime $O_3$ concentrations across the three layers, reflecting stable conditions that allow $NO_x$ to accumulate at the surface. Simulated surface $O_3$ concentrations therefore tend to be underestimated at nighttime. In addition, nighttime heterogeneous uptake of nitrogen on aerosols remains highly uncertain due to the complexity in estimating uptake coefficients for different aerosol composition/mixing states (Lowe et al., 2015; Tham et al., 2018). In UKCA, the lack of nitrate aerosol in the aerosol scheme may result in a lower uptake of nitrogen (Archibald et al., 2020b), particularly in regions with high $NO_x$ emissions. Therefore, there may be a bias in the heterogeneous removal of nitrogen, potentially leading to higher $NO_2$ and lower $O_3$ concentrations at nighttime. In contrast, the peaks in daytime $O_3$ concentrations are captured relatively well, reflecting efficient $O_3$ production in the high-VOC environment.

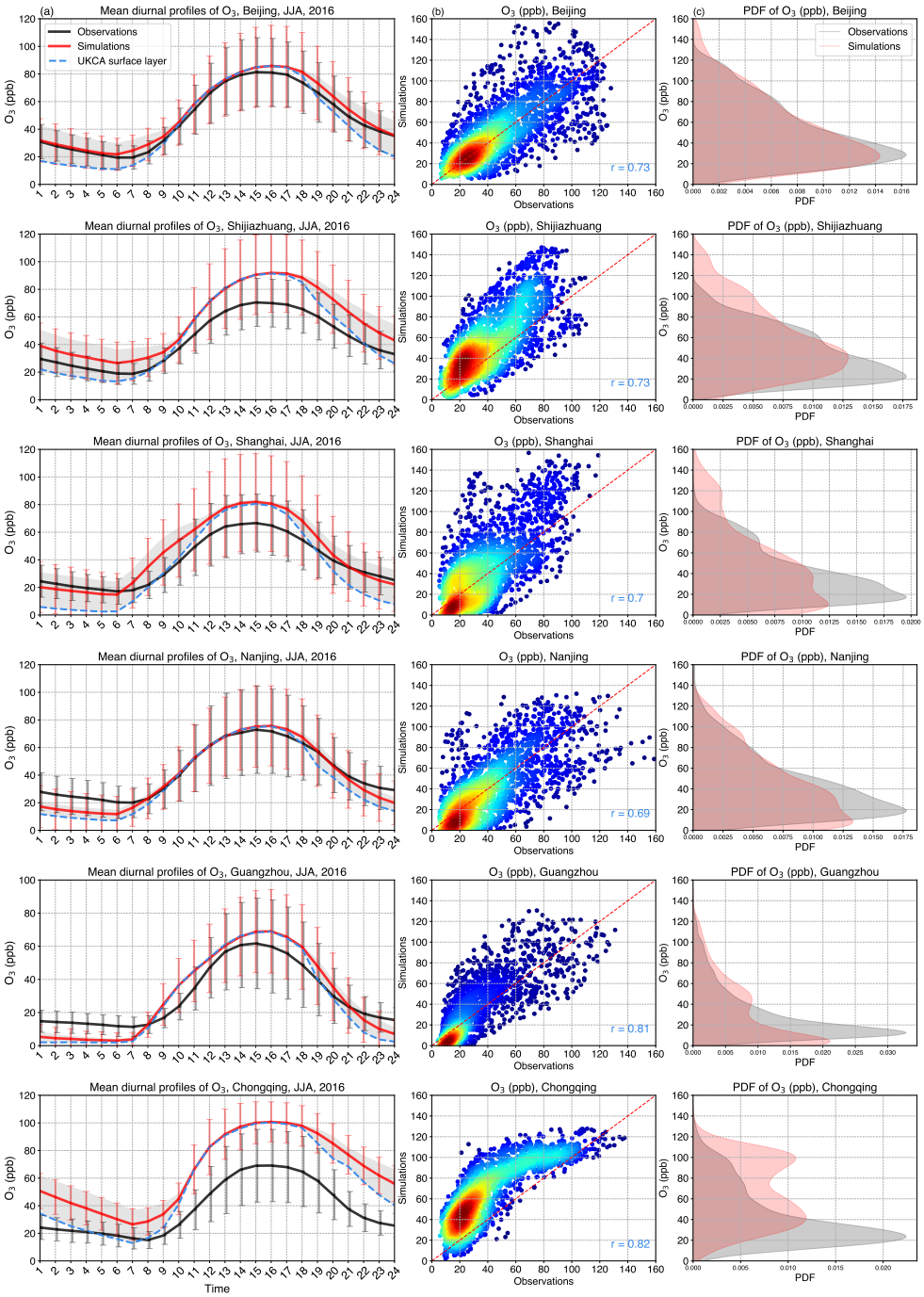


**Figure 2.3:** Comparison of observed and modelled $O_3$ concentrations for the six industrialised regions in JJA, 2016, China. **(a)** Mean diurnal cycles of observed and modelled $O_3$ concentrations (ppb). The shaded area represents the spread across the lowest three model layers. Error bars denote 1 standard deviation of hourly $O_3$ concentrations across all days. **(b)** Observed and modelled hourly $O_3$ concentrations (ppb; three lowest model layers) and correlation coefficient values $r$. **(c)** Probability density function (PDF) of $O_3$ concentrations (ppb) for modelled and observed hourly values.

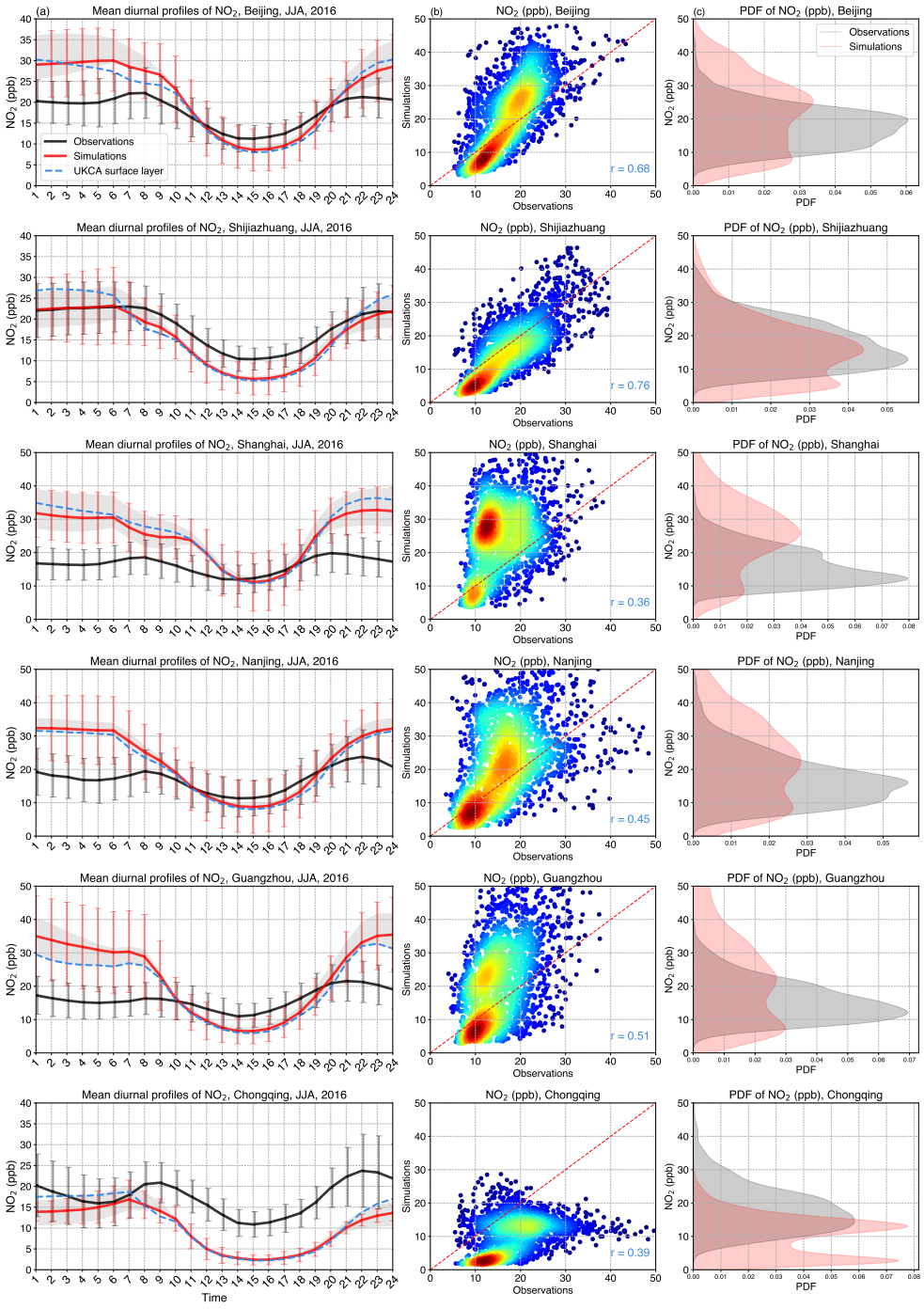


**Figure 2.4:** Comparison of observed and modelled $NO_2$ concentrations for the six industrialised regions in JJA, 2016, China. **(a)** Mean diurnal cycles of observed and modelled $NO_2$ concentrations (ppb). The shaded area represents the spread across the lowest three model layers. Error bars denote 1 standard deviation of hourly $NO_2$ concentrations across all days. **(b)** Observed and modelled hourly $NO_2$ concentrations (ppb; three lowest model layers) and correlation coefficient values $r$. **(c)** PDF of $NO_2$ concentrations (ppb) for modelled and observed hourly values.

**Table 2.2:** Comparison of modelled and observed daily mean surface $O_3$ and $NO_2$ concentrations for the six industrial regions in JJA, 2016, China.

| Region | Obs. (ppb) | Sim. (ppb) | Bias ppb/% | RMSE (ppb) | Correlation $r$ |
|---|---|---|---|---|---|
| $O_3$ | | | | | |
| Beijing | $47.7 \pm 22.1$ | $43.4 \pm 27.7$ | $-4.4$ (9.1 %) | 8.1 | 0.77 |
| Shijiazhuang | $42.9 \pm 18.4$ | $47.6 \pm 28.7$ | 4.7 (10.9 %) | 11.6 | 0.78 |
| Shanghai | $38.3 \pm 17.5$ | $34.4 \pm 28.8$ | $-3.9$ (10.2 %) | 12.7 | 0.77 |
| Nanjing | $42.6 \pm 18.9$ | $35.9 \pm 24.9$ | $-6.8$ (15.8 %) | 9.8 | 0.71 |
| Guangzhou | $29.8 \pm 18.3$ | $28.0 \pm 25.9$ | $-1.8$ ($-6.1$ %) | 9.4 | 0.81 |
| Chongqing | $38.1 \pm 19.2$ | $56.0 \pm 31.3$ | 18.0 (47.2 %) | 22.3 | 0.83 |
| $NO_2$ | | | | | |
| Beijing | $17.8 \pm 3.7$ | $20.7 \pm 8.2$ | 2.9 (16.2 %) | 5.8 | 0.69 |
| Shijiazhuang | $18.1 \pm 4.7$ | $16.7 \pm 8.3$ | $-1.4$ (7.7 %) | 4.3 | 0.76 |
| Shanghai | $16.3 \pm 2.3$ | $26.1 \pm 8.7$ | 9.8 (60.0 %) | 12.1 | 0.50 |
| Nanjing | $17.2 \pm 3.6$ | $21.3 \pm 9.0$ | 4.1 (23.7 %) | 7.8 | 0.49 |
| Guangzhou | $16.1 \pm 3.0$ | $19.9 \pm 9.3$ | 3.8 (23.7 %) | 8.4 | 0.55 |
| Chongqing | $17.4 \pm 3.8$ | $10.9 \pm 6.3$ | $-6.4$ (37.1 %) | 8.0 | 0.43 |

Daily mean $O_3$ concentrations for Beijing, Shijiazhuang, Shanghai and Guangzhou are reproduced well with relatively small biases ($\sim 10\,\%$; see Table 2.2). Simulated daily mean $O_3$ concentrations are highest ($> 40$ ppb) for Beijing, Shijiazhuang and Chongqing; lower in Shanghai and Nanjing ($< 40$ ppb); and lowest for Guangzhou ($\sim 30$ ppb). Although daily mean $O_3$ concentrations are captured relatively well, as seen in Figs. 2.3a and 2.4a, daytime maximum $O_3$ concentrations are overestimated, associated with underestimated $NO_2$ concentrations. This overestimation is largest in Shijiazhuang, where the underestimation of daytime $NO_2$ concentrations is larger than other regions. We find that there is a systematic bias in Chongqing, where simulated $O_3$ levels are higher than observations. Chongqing is a mountainous inland region with complex topography that cannot be fully resolved with coarse model resolution, and surface $O_3$ here is thus representative of higher surface altitudes leading to a systematic bias high compared with observations (Su et al., 2018) and a corresponding bias low for $NO_2$ concentrations. In addition, simulated $O_3$ increases from biogenic emissions in the Sichuan Basin are much larger in summertime than other regions (Lu et al., 2019), and uncertainty in these emissions may contribute to the biases. We therefore investigate $O_3$ chemical environments in different regions to explore regional differences below.

The diurnal patterns in $NO_2$ concentrations can also be captured as reflected by high levels at nighttime and low levels in the daytime for all regions. Daytime $NO_2$ concentrations can be reproduced relatively well relative to nighttime $NO_2$. This underestimation may lead to overestimated $O_3$ concentrations in a VOC-limited regime and underestimated $O_3$ in a $NO_x$-limited regime. While underestimated $NO_x$ concentrations may reflect underestimated $NO_x$ emissions, it is more likely to arise from the effects of dilution

on $NO_x$. High emissions in these regions are diluted over a large grid cell, resulting in lower $NO_2$ concentrations in the daytime. This is offset by high $NO_2$ concentrations in the PBL at nighttime as discussed above. The diurnal variation of $NO_2$ concentrations is hence stronger in the simulations than the observations (Fig. 2.4a).

Figures 2.3 and 2.4 also show the frequency distribution of observed and modelled hourly $O_3$ and $NO_2$ concentrations. The simulated peaks in the distributions of $O_3$ and $NO_2$ are underestimated compared to observations for all six regions, reflecting the larger diurnal variation in the simulations. The diurnal variation is more closely simulated for $O_3$ concentrations (correlation coefficient $r > 0.7$) than for $NO_2$ concentrations. The Chongqing region has the closest correlation with observations ($r = 0.83$), also reflecting the systematic overestimation of $O_3$ as suggested earlier. Overall, the magnitudes (see Table 2.2) and diurnal patterns (see Figs. 2.3 and 2.4) of both species can be simulated reasonably well, with differences between industrial regions clearly captured.

## 2.4 Differences in chemical environment

Spatial distributions of modelled daytime concentrations of $O_3$, $NO_x$, VOCs and $O_3$ sensitivity ratios ($NO_x$ / VOCs and $H_2O_2$ / $HNO_3$) are shown in Fig. 2.5 to illustrate the differences in chemical environment for the six regions. We use the standard definition of the maximum daily average 8 h (MDA8) ozone metric and consider this same time period for other species, which we refer to hereafter as daytime concentrations. For the sensitivity ratio $NO_x$ / VOCs, we consider the sum of anthropogenic and biogenic daytime VOC concentrations.

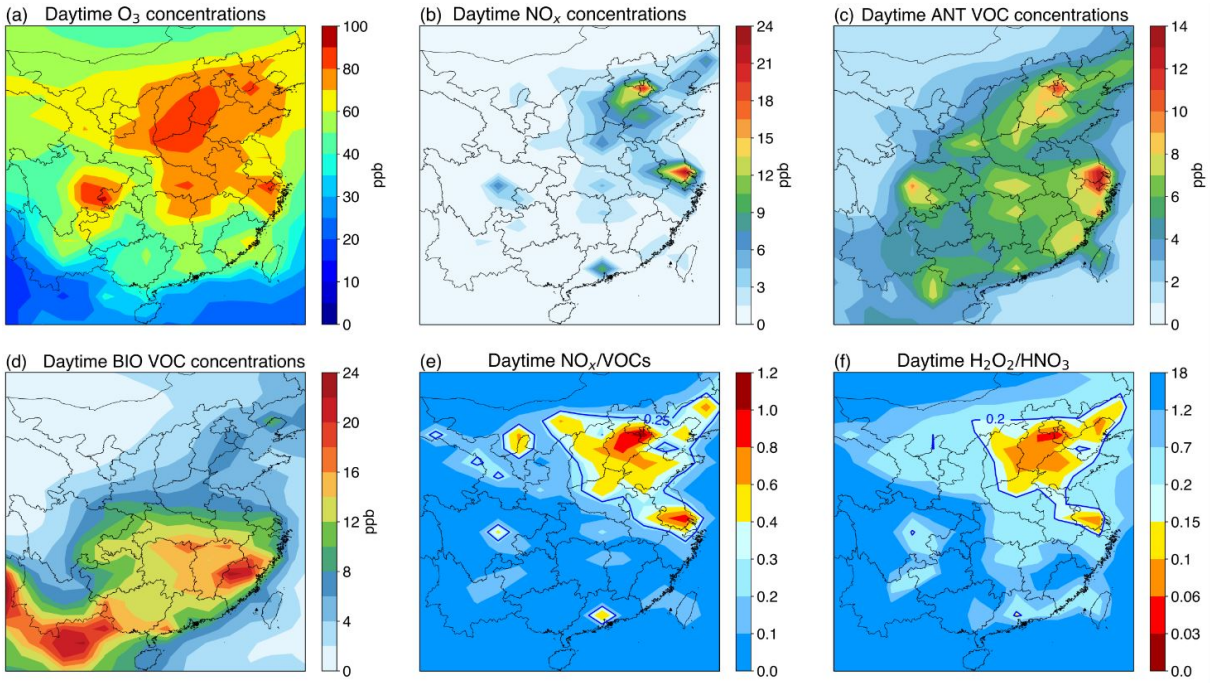


**Figure 2.5:** Spatial distributions of simulated surface daytime $O_3$, $NO_x$, anthropogenic VOCs, biogenic VOCs (ppb) **(a–d)**, and two $O_3$ sensitivity indicators of the concentration ratios – $NO_x$ / VOCs and $H_2O_2$ / $HNO_3$ **(e, f)** – in JJA, 2016, China.

Figure 2.5a shows high daytime $O_3$ levels ($>80$ ppb) across northern China, eastern China and the Sichuan Basin in JJA, 2016. $O_3$ levels in the PRD ($\sim 40$ ppb) are much lower despite high emissions, likely due to transport of clean air from the South China Sea associated with the East Asian summer monsoon (Zhao et al., 2010; Li et al., 2018). Areas with high anthropogenic $NO_x$ and VOC concentrations generally coincide with high-emission regions (Figs. 2.2, 2.5b, c). High daytime $NO_x$ concentrations ($>12$ ppb) are simulated in Beijing and Shijiazhuang, Shanghai, and Nanjing. Chongqing has the lowest $NO_x$ concentrations of 3–6 ppb due to relatively low $NO_x$ emissions. High anthropogenic daytime VOCs concentrations are simulated across the

main industrial regions, in particular in Shanghai with the highest levels ($> 12$ ppb; Fig. 2.5c).

The distribution of biogenic VOC concentrations (including isoprene and methanol) differs from that of anthropogenic VOCs (Fig. 2.5c, d). There is a strong latitudinal gradient, reflecting differences in climate and the spatial distribution of vegetation (Li et al., 2013). The highest biogenic VOC levels are simulated in south-eastern China where deciduous and mixed broadleaf trees are the main source of biogenic VOCs. The YRD, the PRD and the Sichuan Basin have higher biogenic VOC concentrations than the NCP. Chongqing has the highest biogenic VOC levels of the regions considered here. However, higher biogenic VOC levels are found south of China in Laos, Vietnam and Cambodia.

High $NO_x$ / VOC ratios and low $H_2O_2$ / $HNO_3$ ratios typically indicate VOC-limited $O_3$ production as they represent high-$NO_x$ chemical environment. The transition between VOC- and $NO_x$-limited regimes is typically about 0.25 for the $NO_x$ / VOC ratio and about 0.2 for the $H_2O_2$ / $HNO_3$ ratio (Liu et al., 2010; Xing et al., 2019). From these two thresholds for the $O_3$ sensitivity ratios, it can be seen that VOC-limited regions cover most areas of the NCP, parts of the YRD including Shanghai and Nanjing, and Guangzhou in the PRD (Fig. 2.5e, f). All six regions except Chongqing have $NO_x$ / VOCs ratios $\geq 0.6$ and $H_2O_2$ / $HNO_3$ ratios $\leq 0.18$ (Table 2.3). This suggests that these regions have a chemical environment that is strongly VOC limited. In addition, VOC-limited regimes shown by both indicators are quite similar, showing that these two $O_3$ sensitivity ratios may be useful to directly diagnose different $O_3$ sensitivity regimes in China. Regions with high $NO_x$ / VOC ratios and low $H_2O_2$ / $HNO_3$ ratios typically occur where $NO_x$ concentrations are high. Overall, these transition values delineate the different $O_3$ sensitiv-

ity regions across China well, showing VOC-limited regimes in the major industrial regions with high emissions. However, we note that these $O_3$ sensitivity ratios only provide an estimate of the chemical environment, and further, more detailed investigation of $O_3$ responses to emission changes is required.

**Table 2.3:** Simulated surface MDA8 concentrations of species, radicals, $O_3$ sensitivity ratios and the photolysis rate $j(O^1D)$ for the six industrial regions in JJA, 2016, China.

| Region | Beijing | Shijiazhuang | Shanghai | Nanjing | Guangzhou | Chongqing |
|---|---|---|---|---|---|---|
| Species (ppb) | | | | | | |
| $O_3$ | 78.0 | 83.5 | 70.1 | 66.8 | 60.2 | 93.8 |
| $NO_x$ | 12.8 | 8.7 | 19.2 | 12.9 | 10.7 | 3.8 |
| VOC (ANT) | 8.7 | 7.0 | 12.7 | 7.6 | 7.5 | 7.7 |
| VOC (BIO) | 5.5 | 4.3 | 10.6 | 9.2 | 10.2 | 13.5 |
| VOC (Total) | 14.3 | 11.3 | 23.3 | 16.9 | 17.7 | 21.3 |
| Sensitivity ratios | | | | | | |
| $NO_x$ / VOCs | 0.79 | 0.73 | 0.89 | 0.78 | 0.60 | 0.18 |
| $H_2O_2$ / $HNO_3$ | 0.18 | 0.08 | 0.10 | 0.11 | 0.09 | 0.29 |
| Radicals | | | | | | |
| OH / $10^6\,cm^{-3}$ | 7.8 | 10.3 | 8.4 | 9.8 | 13.0 | 16.6 |
| $HO_2$ / $10^8\,cm^{-3}$ | 2.6 | 2.9 | 2.3 | 2.2 | 2.2 | 7.4 |
| $RO_2$ / $10^8\,cm^{-3}$ | 1.0 | 0.9 | 0.8 | 0.8 | 0.9 | 2.5 |
| Photolysis rate | | | | | | |
| $j(O^1D)$/ $10^{-5}\,s^{-1}$ | 2.3 | 2.6 | 2.3 | 2.5 | 3.1 | 3.4 |

## 2.5 Differences in local $O_3$ production rates

In this section, we calculate the daytime production rates for surface $O_3$ to investigate how the local $O_3$ production compares across the six regions. We define the net $O_3$ production rate ($\mathrm{ppb\,h^{-1}}$) as the gross rate of production of $O_3$, $P(O_3)$, from the reactions $HO_2$ + NO and $RO_2$ + NO minus the gross rate of loss of $O_3$, $L(O_3)$, from the reactions $O(^1D)$ + $H_2O$, $O_3$ + OH, $O_3$ + $HO_2$ and $O_3$ + VOCs. We assume that the pathways above represent the net $O_3$ production rate under $O_3$ photochemical steady state between NO and $NO_2$, and they are shown as follows:

$$\begin{aligned} Net\ P(O_3) = &\ P(O_3) - L(O_3) \\ = &\ k_1[HO_2][NO] + k_2[RO_2][NO] \\ -(&k_3[O(^1D)][H_2O] + k_4[O_3][OH] \\ +&k_5[O_3][HO_2] + k_6[O_3][VOCs]), \end{aligned} \tag{2.1}$$

where $k_i$ represents the rate coefficient of reaction $i$.

The loss of $NO_x$, $L(NO_x)$, is principally determined by the reactions OH + $NO_2$, $RO_2$ + $NO_2$ and $RO_2$ + NO, which produce $HNO_3$, $RO_2NO_2$ and $RONO_2$ respectively. OPE is then defined as the number of $O_3$ molecules produced per molecule of $NO_x$ consumed (Liu et al., 1987).

$$OPE = \frac{P(O_3)}{L(NO_{\mathrm{x}})} \tag{2.2}$$

As shown in Fig. 2.6, local $O_3$ production varies across the six regions, with $O_3$ net production rates ranging from 4 to 10 $\mathrm{ppb\,h^{-1}}$. Simulated daytime net $O_3$ production rates are highest ($> 8\,\mathrm{ppb\,h^{-1}}$) in Shanghai and Guangzhou mainly due to high precursor emissions, and this is reflected by higher $O_3$ concentrations in Shanghai than in nearby Nanjing. While $O_3$ production

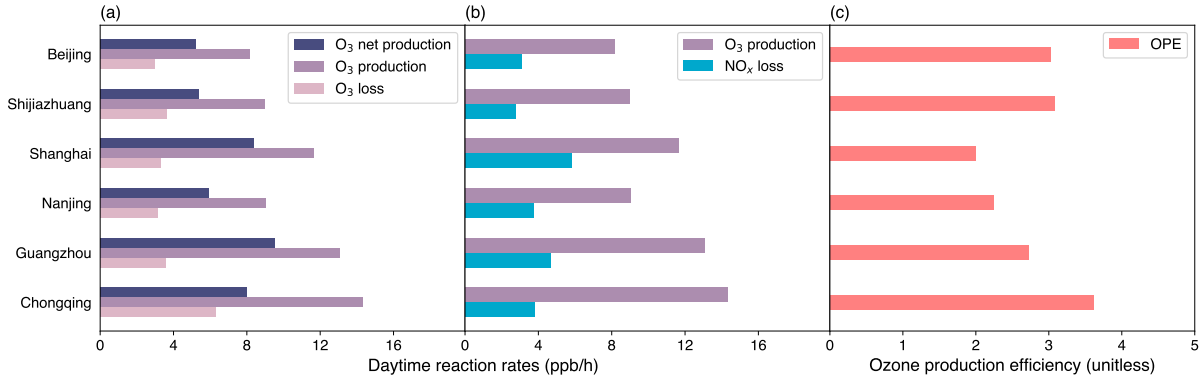


**Figure 2.6:** Simulated surface daytime **(a)** net $O_3$ production rates, gross $O_3$ production rates and gross $O_3$ loss rates (ppb $h^{-1}$); **(b)** gross $O_3$ production rates and $NO_x$ loss rates (ppb $h^{-1}$); and **(c)** OPE (unitless) for the six industrial regions in JJA, 2016, China.

is high in Guangzhou, the $O_3$ concentrations are much lower than in other regions, indicating that meteorological impacts in this coastal region are important to transport $O_3$ produced locally. $O_3$ net production in Beijing and Shijiazhuang is similar to that in Nanjing ($\sim 5$ ppb $h^{-1}$). $O_3$ production in Chongqing is also high, reflecting high radical concentrations (see Table 2.3) that promote $O_3$ production despite lower precursor emissions. High photolysis rates $jO(^1D)$) in Chongqing and Guangzhou contribute to high concentrations of OH radicals (Table 2.3). $O_3$ destruction rates are fairly similar ($< 4$ ppb $h^{-1}$) across these regions but are higher in Chongqing, offsetting its high $O_3$ production rates.

The simulated $NO_x$ loss rates (Fig. 2.6b) show the highest removal of $NO_x$ in Shanghai, where $NO_x$ concentrations are also highest. This influences OPE, which is strongly dependent on $NO_x$ loss, and leads to the lowest OPE in Shanghai and highest in Chongqing (Fig. 2.6c). The low OPE in Shanghai and Nanjing shows the low efficiency in $O_3$ production per molecule of $NO_x$

consumed. However, the OPE values in all six regions are generally lower than those in other remote and rural regions, in agreement with Wang et al. (2018), indicating that high surface $O_3$ concentrations could still occur in these regions due to high precursor emissions despite low OPE.

## 2.6 Response of $O_3$ to emission controls

We quantify the response of daytime $O_3$ to emission changes to investigate the relationship between the chemical environment and the magnitude of $O_3$ changes for the six industrial regions of China. We implement three scenarios applying 20 % reductions in anthropogenic $NO_x$ emissions, VOC emissions, and combined $NO_x$ and VOC emissions.

Spatial distributions of simulated daytime surface $O_3$ responses vary across China (Fig. 2.7). In the 20 % $NO_x$ emission control scenario, substantial $O_3$ increases (2–10 ppb) can be seen in the NCP, the YRD, and the PRD, and $O_3$ concentrations decrease (0–8 ppb) in the Sichuan Basin. In the 20 % VOC emission control scenario, there are small $O_3$ changes in most non-industrial regions of China ($-$1–2 ppb), but $O_3$ concentrations generally decrease by 1–9 ppb across the NCP, the YRD and the PRD. The Sichuan Basin shows relatively small $O_3$ decreases. Areas showing $O_3$ increases in the 20 % $NO_x$ emission control experiment match well with VOC-limited areas indicated by the $NO_x$ / VOCs and $H_2O_2$ / $HNO_3$ ratios (cf. Fig. 2.5e, f vs. Fig. 2.7a), suggesting that all the industrial regions considered here are VOC limited except Chongqing in the Sichuan Basin that is $NO_x$ limited. The determination of $O_3$ sensitivity regimes here is based on the $O_3$ responses to decreasing anthropogenic $NO_x$ and/or VOC emissions, and any potential impacts of changing BVOC emissions has not been assessed. Decreasing BVOC emissions may

offset the increase in $O_3$ levels due to decreased $NO_x$ emissions for the NCP, the YRD, and the PRD and would make all regions more VOC limited. We note that our conclusion of $NO_x$ limitation in Chongqing may be sensitive to our underestimation of $NO_2$ levels (Sect. 2.3) and to the higher BVOC emissions in this region, both of which reduce the ratio of $NO_x$ to VOC in the region (Table 2.3). However, satellite-observation-based studies have also suggested this region as one that is largely $NO_x$ limited, in contrast to the heavily populated coastal regions (Wang et al., 2021).

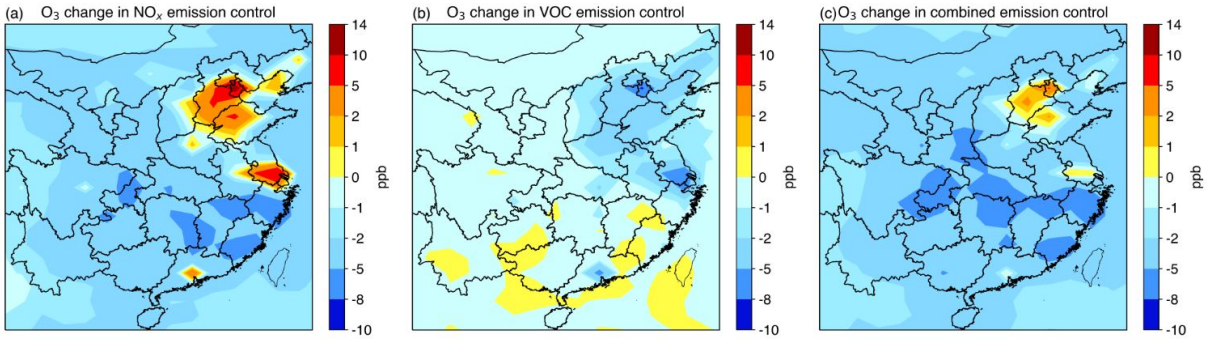


**Figure 2.7:** Spatial distributions of simulated surface daytime $O_3$ concentration changes (ppb) for **(a)** the 20 % $NO_x$ emission control, **(b)** the 20 % VOC emission control, and **(c)** the 20 % combined $NO_x$ and VOC emission control compared to the present-day results in JJA, 2016, China.

In general, the greatest $O_3$ increases in the 20 % $NO_x$ control scenario occur in areas with high precursor concentrations. Shanghai shows the largest $O_3$ increases (11 %) (Table 2.4) and has the highest underlying $NO_x$ concentrations (Table 2.3). $O_3$ increases in Beijing and Guangzhou are similar ($\sim$ 8 %), possibly because of their similar $NO_x$ concentrations. Shijiazhuang in the NCP shows the smallest $O_3$ increase (4 %) because of its lower $NO_x$ concentrations. In contrast, an $O_3$ decrease of 4 % is seen in Chongqing, which is $NO_x$ limited. In the 20 % VOC control scenario, the largest $O_3$ decreases are simulated in Shanghai and Guangzhou ($-10$ %), while minimal $O_3$ decreases ($-1$ %) are simulated in Chongqing. The simulated chemical environment in Chongqing is $NO_x$ limited, and therefore the $O_3$ changes are not sensitive to VOC emissions.

In addition to separate 20 % reductions in $NO_x$ and VOC emissions, we demonstrate the importance of combined $NO_x$ and VOC emission controls to mitigate $O_3$ pollution in VOC-limited regions. This effectively offsets the higher levels of $O_3$ that arise with $NO_x$ emission reductions alone. The $O_3$ increase in Shanghai is fully offset in the combined emission control ($-1$ %). While $O_3$ increases still occur in the other VOC-limited regions, these increases are minimal ($< 3$ %). Reducing both $NO_x$ and VOC emissions decreases $O_3$ levels in Chongqing by 6 %. Therefore, combined emission controls are necessary to efficiently mitigate $O_3$ pollution in all these industrial regions, and VOC emission controls should be at least as stringent as $NO_x$ emission controls to address rising $O_3$ levels in these industrial regions.

**Table 2.4:** Simulated daytime mean $O_3$ concentrations and changes (ppb) in $NO_x$, VOC, and combined $NO_x$ and VOC emission controls for the six industrial regions in JJA, 2016, China.

| Region | Base | $NO_x$ control | Change (%) | VOC control | Change (%) | $NO_x$+VOC control | Change (%) |
|---|---|---|---|---|---|---|---|
| Beijing | 78.0 | 84.7 | 8.6 % | 72.5 | −7.0 % | 79.7 | 2.2 % |
| Shijiazhuang | 83.5 | 86.6 | 3.8 % | 80.2 | −3.9 % | 84.6 | 1.4 % |
| Shanghai | 70.1 | 77.8 | 11.0 % | 63.1 | −10.0 % | 69.4 | −1.0 % |
| Nanjing | 66.8 | 72.4 | 8.5 % | 61.4 | −8.0 % | 67.8 | 1.6 % |
| Guangzhou | 60.2 | 64.8 | 7.6 % | 53.8 | −10.7 % | 60.4 | 0.3 % |
| Chongqing | 93.8 | 89.5 | −4.6 % | 92.5 | −1.4 % | 88.5 | −5.6 % |

## 2.7 Effectiveness of emission controls in reducing surface $O_3$ levels

To provide a more complete exploration of the effectiveness of emission controls, we construct a response surface of summertime daytime $O_3$ for each region to show the effect of changing $NO_x$ and VOC emissions. We do this by performing a set of 64 model simulations with global anthropogenic $NO_x$ and VOC emissions scaled independently over the range 0 %–140 % in increments of 20 %.

Figure 2.8 shows the magnitude and direction of $O_3$ changes in the six regions as $NO_x$ and VOC emissions change. For context, Fig. 2.8a also shows the simulated daytime $O_3$ changes between 2013 and 2019 in the Beijing region, assuming that the emission changes observed between 2013 and 2016 continue at the same rate until 2019 (Cheng et al., 2019). We find that simulated $O_3$ concentrations in Beijing increase from 71.6 ppb in 2013 to 82.6 ppb in 2019, an increase of 1.8 ppb $yr^{-1}$. This is consistent with observed changes of 1.9 ppb $yr^{-1}$ over this period due to anthropogenic emission changes (Li et al., 2020). The observed daytime $O_3$ concentrations are 83 ppb in the Beijing region in 2019. This demonstrates that the model captures not only the magnitude and diurnal pattern of $O_3$ in summer 2016 well but also the observed $O_3$ changes in recent years.

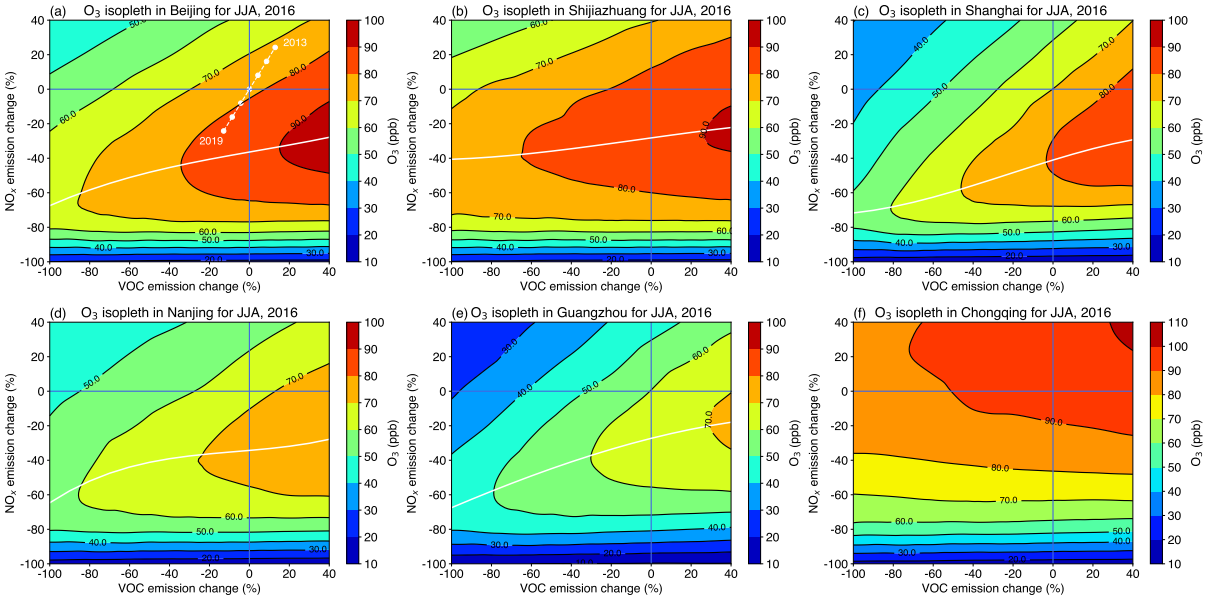


**Figure 2.8:** Simulated MDA8 surface $O_3$ responses (ppb) to anthropogenic $NO_x$ and VOC emission changes for the six industrial regions across China **(a–f)** in JJA, 2016. The intersection of the vertical and horizontal lines marks current $O_3$ levels. White ridge lines mark the peak in $O_3$ concentrations for given VOC emissions and show the approximate transition between VOC-limited (above the ridge) and $NO_x$-limited (below the ridge) regimes. White dots in panel **(a)** represent simulated daytime $O_3$ levels in the Beijing region in JJA between 2013 and 2019 following estimated $NO_x$ and VOC emission changes.

The patterns of $O_3$ response seen in the VOC-limited regions (Fig. 2.8a–e) are similar, such that decreases in $NO_x$ emissions from their current levels increase $O_3$ concentrations. Large $O_3$ increases occur in Shanghai and Beijing, highlighting that it is not beneficial to reduce $NO_x$ emissions unless VOC emissions are also reduced. Large reductions ($\sim 40\,\%$) in $NO_x$ emissions are required to shift the chemical environment from VOC limited to $NO_x$ limited for these two regions. The large decrease in $O_3$ in Shanghai and Guangzhou when reducing VOC emissions indicates that the efficiency in lowering $O_3$ levels by decreasing VOC emissions is high in these regions. In contrast, the efficiency of VOC emissions alone in reducing $O_3$ levels is lower in Shijiazhuang and Chongqing.

Figure 2.9 shows the $O_3$ responses in each region to changes in $NO_x$ emissions, VOC emissions, and combined $NO_x$ and VOC emissions, which represent cross sections through the $O_3$ response surfaces shown in Fig. 2.8. It is difficult to decrease $O_3$ concentrations in Shanghai by reducing $NO_x$ emissions alone because there is a steep rise in surface $O_3$ ($\sim 15\,\%$) when $NO_x$ emissions are reduced by $40\,\%$ from the current state. Decreasing $O_3$ from current levels requires reductions in $NO_x$ emissions of more than $50\,\%$ for Shijiazhuang and Guangzhou and more than $70\,\%$ for Beijing, Shanghai and Nanjing. This suggests that mitigating poor $O_3$ air quality in these VOC-limited regions through $NO_x$ emission controls alone would require much greater reductions than the $21\,\%$ reductions in $NO_x$ emissions that are reported to have occurred in China from 2013 to 2017 (Zheng et al., 2018).

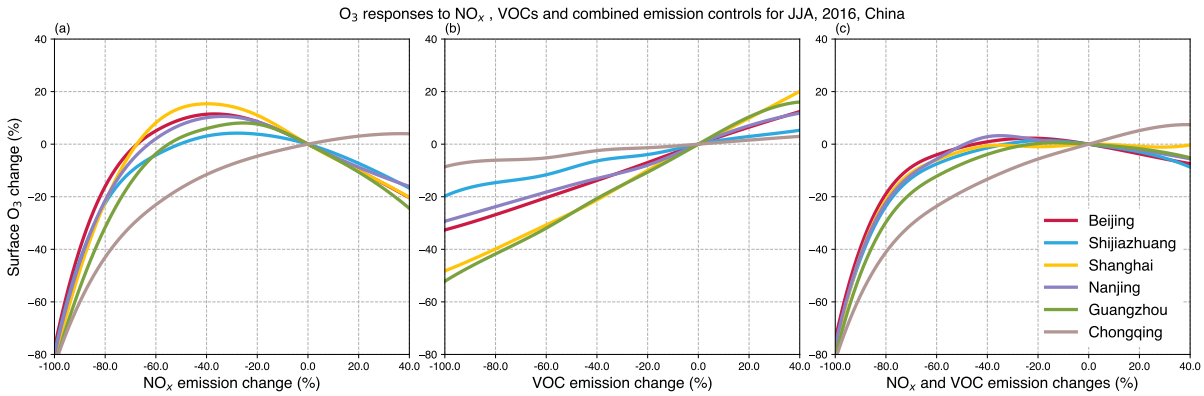


**Figure 2.9:** Simulated daytime surface $O_3$ responses to changes in anthropogenic emissions of **(a)** $NO_x$, **(b)** VOC, and **(c)** combined $NO_x$ and VOC emissions with the same percentage changes for the six industrial regions in JJA, 2016, China.

$O_3$ responses to VOC emission changes are smaller and more linear than the responses seen for $NO_x$ emissions changes (Fig. 2.9a, b). Reducing VOC emissions by 40 % gives large decreases in $O_3$ concentrations (20 %) in Shanghai and Guangzhou and smaller decreases ($<10$ %) in Shijiazhuang and Chongqing (Fig. 2.9b). Reductions in VOC emissions are key to reducing present-day $O_3$ concentrations as they effectively offset the rising $O_3$ levels due to decreasing $NO_x$ emissions (Fig. 2.9c). Emission reductions of 50 % or more are required to reduce $O_3$ levels for all regions if controls on $NO_x$ and VOC emissions are applied simultaneously.

To place our results in a wider global context, Fig. 2.10 shows summer daily mean surface $O_3$ changes over different regions with high emissions in other parts of the world compared with those in China. We consider six major industrialised regions outside of China and select the model grid cell that is most closely co-located with the region. We note that proportional increases in summer daily mean $O_3$ are larger than that of daytime $O_3$ increases when

$NO_x$ emissions are reduced (see Fig. 2.9), principally because absolute $O_3$ concentrations are smaller with the inclusion of nighttime conditions. We find that all selected high-emission regions across the globe outside of China are $NO_x$ limited at the model resolution considered here, such that $NO_x$ emission decreases yield regional $O_3$ decreases. Current levels of $NO_x$ emissions in these regions are considerably lower than for the industrial regions of China, reflecting the different $O_3$ sensitivity regimes (Table 2.5). We note that these results apply to the wide urban regions considered here and that local $O_3$ sensitivity in some parts of these regions may be different.

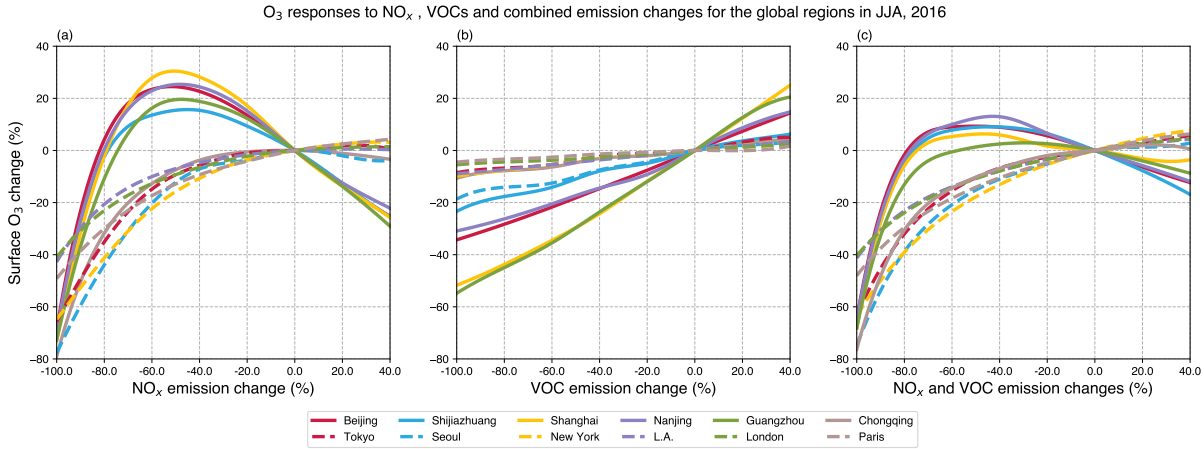


**Figure 2.10:** Simulated summer daily mean surface $O_3$ responses to anthropogenic **(a)** $NO_x$, **(b)** VOC, and **(c)** combined $NO_x$ and VOC emission changes with the same percentage changes in regions across the globe: Tokyo, Seoul, New York, L.A., London, Paris (dashed lines) and those in major industrial regions of China (solid lines) in JJA, 2016.

**Table 2.5:** Anthropogenic $NO_x$ and VOC emissions ($\times 10^{-10}\,\mathrm{kg\,m^{-2}\,s^{-1}}$) and summertime mean surface $O_3$ concentrations (ppb) in regions across the industrial regions of China and the globe. MEIC emissions of 2013 adjusted for 2016 are used for Chinese industrial regions. HTAP emissions of 2010 are used for other regions of the globe.

| Region | $NO_x$ emissions | VOC emissions | $O_3$ conc. |
|---|---|---|---|
| China | | | |
| Beijing | 5.5 | 6.7 | 43.4 |
| Shijiazhuang | 4.2 | 4.6 | 47.6 |
| Shanghai | 7.4 | 9.6 | 34.4 |
| Nanjing | 6.9 | 8.1 | 35.9 |
| Guangzhou | 8.4 | 12.0 | 28.0 |
| Chongqing | 3.1 | 3.6 | 56.0 |
| Global | | | |
| Tokyo | 2.0 | 2.6 | 38.9 |
| Seoul | 1.5 | 2.1 | 45.5 |
| New York | 2.3 | 3.1 | 45.3 |
| L.A. | 1.1 | 1.3 | 40.1 |
| London | 1.1 | 1.5 | 30.6 |
| Paris | 0.8 | 1.0 | 32.6 |

Reductions of both $NO_x$ and VOC emissions substantially decrease $O_3$ levels for these selected regions outside of China, and the magnitude of the $O_3$ decreases are similar to those found for Chongqing (Fig. 2.10). Conversely, the magnitude of $O_3$ decreases when reducing VOC emissions are smaller than all five VOC-limited regions in China. This indicates that $O_3$ concentrations are less sensitive to VOC emissions in these other world regions due to their lower VOC emissions (Table 2.5).

Despite lower $NO_x$ and VOC emissions in the regions outside of China, surface $O_3$ concentrations, particularly in the Seoul and New York regions, are similar to those for China. This highlights that regional $O_3$ levels also depend on background $O_3$ concentrations, despite localised $NO_x$ and VOC emissions that lead to different $O_3$ production regimes. The $O_3$ levels in European regions, e.g. London and Paris, are lowest, in accordance with the lowest $NO_x$ and VOC emission levels. Overall, these results show that there are substantial differences in the efficiency of emission control scenarios to reduce surface $O_3$ levels in different parts of the world. For many industrial regions of China, the extended regions are VOC limited, and hence reductions of VOC emissions are the key to reducing poor $O_3$ air quality. For other regions selected in this study $NO_x$ emission reductions are still pertinent to improving $O_3$ pollution.

## 2.8 Conclusions

This study presents the application of the global chemistry–climate UKCA model with an improved gas-phase chemistry scheme including more reactive VOCs to simulate regional summertime $O_3$ pollution across major industrialised regions in China for the first time. Differences in atmospheric chemical environments are investigated, and the effectiveness of different emission control strategies in reducing $O_3$ concentrations is quantified. The model captures the magnitude, diurnal profiles and diurnal variation of $O_3$ concentrations across most industrial regions well. We highlight that peak $O_3$ concentrations can be captured well, indicating that $O_3$ production can be effectively simulated with more highly active VOC oxidation environments for high-emission regions of China.

Simulated daytime $O_3$ levels are highest on the North China Plain (Beijing and Shijiazhuang) and in the Sichuan Basin (Chongqing) and are lowest in the Pearl River Delta (Guangzhou). We find that there is a systematic bias in $O_3$ throughout the diurnal cycle in Chongqing, reflecting the mountainous inland area that is inadequately captured by the topography in the model. The $O_3$ production rates are highest in the Pearl River Delta compared to other regions. However, its much lower $O_3$ levels reflect the importance of meteorological impacts in this coastal region. OPE values in these industrial regions are low, indicating that their high $O_3$ levels are mainly caused by high precursor emissions. Both $O_3$ sensitivity ratios we apply here ($NO_x$ / VOCs and $H_2O_2$ / $HNO_3$) suggest that all the industrial regions except Chongqing are VOC limited. This study hence provides a broad assessment of the $O_3$ sensitivities for these regions with implications for emission control strategies.

A set of simulations are performed with a range of $NO_x$ and VOC emissions to construct $O_3$ response surfaces to assess the impacts of different emission control strategies in different regions. Reducing $NO_x$ emissions alone by 20 % leads to a substantial $O_3$ increase (11 %) in Shanghai. Reductions in VOC emissions alone of 20 % produce the largest decrease (−11 %) in $O_3$ levels in Shanghai and Guangzhou and the smallest decrease (−1 %) in Chongqing. We find that reducing $O_3$ concentrations across all industrial regions of China would require more than 70 % reductions if reducing $NO_x$ emissions alone, and therefore VOC emission controls are important to reduce $O_3$ levels. We also find that combined emission controls effectively offset high $O_3$ levels that arise from reduced $NO_x$ emissions alone. These responses are substantially different from those currently found in major highly populated regions in other parts of the world. The results show $NO_x$-limited $O_3$ production in these global areas, which also reflects the predominance of heavily populated VOC-limited areas across the industrial regions in China. Therefore, $O_3$ pollution in the industrial regions of China should be treated as a regional issue, and regional VOC emission control strategies should be considered.

The new capabilities for simulating regional surface $O_3$ pollution developed here will be helpful for future model studies to investigate the regional $O_3$ impacts on climate. The magnitude of $O_3$ changes over recent years in the Beijing region can be reproduced well. There remain model biases in regions with complex topography and high elevation – a common issue for global and regional models. Another source of uncertainty is the rapid change in anthropogenic emissions in recent years in China, which presents a particular challenge for inventory development. Recently, while $NO_x$ emissions have been successfully reduced across many regions in China, changes in VOC emissions have been relatively small, and this has led to an increase

in $O_3$ concentrations in many regions. Regional VOC emission controls are hence urgently needed to maximise the effectiveness in reducing surface $O_3$ pollution in China.

# Chapter 3

# Tropospheric ozone changes and ozone sensitivity from present-day to future under shared socio-economic pathways

This chapter has been published in the open-access journal Atmospheric Chemistry and Physics (ACP). The final version is available online from https://doi.org/10.5194/acp-22-1209-2022. The work has been implemented in collaboration with Prof. Ruth Doherty, Prof. Oliver Wild, Dr. Fiona O'Connor and Dr. Steven T. Turnock. ZL, RD, OW, FO'C, ST designed the study. ZL set up the model, conducted model simulations and performed the analysis. ZL, RD and OW prepared the paper. All co-authors contributed to reviewing and editing the paper.

## 3.1 Introduction

Ozone ($O_3$) is a chemically reactive component in the atmosphere that is produced from natural and anthropogenic sources. Emissions of $O_3$ precursors including nitrogen oxides ($NO_x$), volatile organic compounds (VOCs), methane ($CH_4$) and carbon monoxide (CO) lead to the formation of $O_3$ by a series of photochemical reactions in the presence of sunlight. $O_3$ has important impacts on human health, ecosystems and climate change (Lefohn et al., 2008; Zhang et al., 2019a; Agathokleous et al., 2020). $O_3$ concentrations are largely governed by the magnitudes of $O_3$ precursor emissions, transport, deposition and transport from the stratosphere. $O_3$ exerts a positive radiative forcing (Stevenson et al., 2013; O'Connor et al., 2021; Thornhill et al., 2021a), and changes in climate in turn influence ozone (Fiore et al., 2012; Doherty et al., 2013). Climate change can alter natural emissions of biogenic VOCs (BVOC), lightning $NO_x$ and $CH_4$, along with temperature, humidity, convection and clouds, which further influence $O_3$ concentrations (Thornhill et al., 2021b). The interactions between air quality and climate play an important role in the coupled Earth system, and we focus on the impacts of future emissions in the context of climate change on tropospheric $O_3$ in this study.

The tropospheric $O_3$ burden is controlled by the amount of $O_3$ production, $O_3$ destruction, $O_3$ deposition and the $O_3$ transport from the stratosphere (Lelieveld and Dentener, 2000; Wild, 2007). From pre-industrial times to the present day, the tropospheric $O_3$ burden has increased from approximately 240 Tg to 350 Tg mainly due to substantial increases in anthropogenic $O_3$ precursor emissions (Lamarque et al., 2010; Young et al., 2013; Griffiths et al., 2021). However, regional surface $O_3$ changes between the pre-industrial and

present day vary substantially due to different regional emission changes (Turnock et al., 2020) and to differences in $O_3$ sensitivity to $NO_x$ and VOC emissions. In recent decades, there has been a decrease in surface $O_3$ concentrations in North America and Europe due to emission controls (Simon et al., 2015; Colette et al., 2016; Tarasick et al., 2019). In contrast, increases in surface $O_3$ levels are observed in South Asia and East Asia due to industrialization, urbanization and social development (Hakim et al., 2019; Lu et al., 2020). Furthermore, while emission controls have been implemented across industrial regions of China in recent years, these have focused on emissions of $NO_x$ and particulate matter, and have led to increased $O_3$ pollution in some places (Wang et al., 2017b; Silver et al., 2018).

It is important to investigate $O_3$ sensitivity to understand how $O_3$ chemical regimes might change in different parts of the world, and to guide suitable emission control strategies. $O_3$ sensitivity is typically characterised by $NO_x$- or VOC-limited regimes for $O_3$ production, and this determines the effectiveness of different emission control strategies. It is dependent on the relative abundances of $NO_x$ and VOC concentrations (Sillman, 1999), or of their oxidation products, nitric acid ($HNO_3$) and hydrogen peroxide ($H_2O_2$) (Kleinman, 1994; Sillman, 1995). VOC-limited regimes typically occur in highly urbanised regions with high $NO_x$ concentrations in which decreases in $NO_x$ emissions increase $O_3$ concentrations, and $O_3$ production increases with higher VOC emissions. In contrast, changes in $NO_x$ concentrations dominate $O_3$ changes in $NO_x$-limited regimes such that decreases in $NO_x$ emissions decrease $O_3$ concentrations, and $O_3$ concentrations are less sensitive to VOC emissions. $O_3$ sensitivity indicators such as the ratios of $NO_x$/VOCs and $HNO_3/H_2O_2$ allow us to identify $O_3$ sensitivity regimes relatively easily. However, most studies focus on $O_3$ sensitivity in specific regions and for short

time periods (Dunker et al., 2002; Sillman and West, 2009; Ye et al., 2016), leading to inconsistency in the critical indicator values that distinguish $O_3$ sensitivity regimes. To address this, we generalise the approach by quantifying $O_3$ sensitivity using a consistent indicator across the globe. This is the first time that the full range of surface chemical environments across the globe has been explored with a global chemistry-climate model, as far as we are aware. We quantify $O_3$ sensitivity based on the ratio of $NO_x$ and VOC concentrations, and investigate how regional $O_3$ sensitivity might change in the future.

The shared socio-economic pathways (SSPs) are future emission and climate scenarios accounting for future social, economic and environmental developments (O'Neill et al., 2014; van Vuuren et al., 2014). The SSPs represent a range of levels of policy strength (weak, medium and strong) to control emissions of near-term climate forcers (NTCFs) that include tropospheric $O_3$, $O_3$ precursors and aerosols (Rao et al., 2017). Our study is based on simulations using historical and future SSPs emissions and climate undertaken as part of the Aerosol Chemistry Model Intercomparison Project (AerChemMIP; Collins et al., 2017) and the wider Coupled-Model Intercomparison Project Phase 6 (CMIP6; Eyring et al., 2016). The aim of AerChemMIP is to quantify the effects of chemistry and aerosols on air quality and climate in CMIP6 by conducting historical and future experiments using chemistry-climate models with specified climate and emission trajectories.

We examine tropospheric $O_3$ and surface $O_3$ sensitivity under present-day (2004–2014) and future conditions (2045–2055). Model development and application are described in Sect. 3.2 along with descriptions of the emission and climate scenarios used. We compare and evaluate the present-day tropospheric $O_3$ burden and surface $O_3$ concentrations with two different chemistry

schemes in Sect. 3.3. We then investigate the seasonal, daytime and nighttime differences in $O_3$ changes in the future compared to present-day for different regions in Sect. 3.4. Analysis of $O_3$ concentrations and production is used to quantify $O_3$ sensitivity and to explain contrasting regional $O_3$ changes in Sect. 3.5. We then show the changes in $O_3$ sensitivity between different seasons and scenarios in Sect. 3.6 and present our conclusions in Sect. 3.7.

## 3.2 Materials and methods

### 3.2.1 Model description, development and application

The chemistry-climate model, UKESM1 is used in this chapter. Model description and development are fully introduced in section 1.3. Only necessary information of the model set-up and the model application for this chapter is described below. We use UKESM1 to reproduce present-day (2004–2014) $O_3$ concentrations and to predict $O_3$ responses to emissions and climate in the future (2045–2055).

While the UKESM1 configuration for CMIP6 used the UKCA StratTrop mechanism, this study also uses an extended gas-phase chemistry scheme that incorporates more reactive VOC species to permit a more realistic representation of $O_3$ production in polluted environments. The extended chemistry scheme (denoted as Ext_StratTrop hereafter) is based on the StratTrop scheme and includes oxidation of the additional chemical components propene ($C_3H_6$), butane ($C_4H_{10}$) and toluene ($C_7H_8$) to represent alkenes, alkanes and aromatic VOC classes, as described in Liu et al. (2021).

The atmosphere-only configuration of UKESM1 is used with prescribed sea

surface temperatures and sea ice to show the transient impacts of emissions under present-day and future climates. These are prescribed using monthly-mean time-evolving fields from the fully coupled UKESM1. Greenhouse gas concentrations are prescribed as in historical and future simulations conducted by UKESM1 as part of CMIP6 (Meinshausen et al., 2017, 2020).

### 3.2.2 Emissions and experiments

Present-day CMIP6 anthropogenic and biomass burning emissions are taken from Hoesly et al. (2018) and van Marle et al. (2017), respectively. Biogenic VOC emissions are calculated interactively within the iBVOC emissions scheme (Pacifico et al., 2011) in the Joint UK Land Environmental Simulator (JULES) land-surface scheme which is coupled to UKCA. Other aspects of the emissions used here are the same as described in Turnock et al. (2020). Anthropogenic emissions are categorised into five sectors (industry, power plants, transport, residences and agriculture) as inputs to the model, with independent diurnal and vertical emission profiles applied for each sector (Bieser et al., 2011; Mailler et al., 2013; Liu et al., 2021).

Three CMIP6 SSP scenarios are used for future simulations: SSP3-7.0, SSP3-7.0-lowNTCF and SSP3-7.0-lowCH4. SSP3-7.0 pathway has a large anthropogenic climate forcing signal (a radiative forcing of 7.0 W m-2 at 2100) , and weak emission controls on $O_3$ precursors and aerosols, and rapidly increasing $CH_4$ concentrations (Fujimori et al., 2017; Rao et al., 2017). SSP3-7.0-lowNTCF and SSP3-7.0-lowCH4 are additional pathways which use the same underlying climate policies as SSP3-7.0. SSP3-7.0-lowNTCF has strong controls on all NTCF emissions. SSP3-7.0-lowCH4 follows SSP3-7.0 but assumes strong mitigation of $CH_4$ emissions in the future, with 24 % decreases in surface $CH_4$ mixing ratios from 1802 ppb to 1364 ppb. The last time

that historical surface $CH_4$ mixing ratios were this low was more than 50 years ago, in the late 1960s (Prather et al., 2014). BVOC emissions increase under all these pathways due to a warmer climate. We perform four model experiments in this study to investigate tropospheric $O_3$ for the present-day (2004–2014) and three future pathways (SSP3-7.0, SSP3-7.0-lowNTCF and SSP3-7.0-lowCH4; 2045–2055). Table 3.1 shows the model configuration for the four simulations. Table 3.2 lists the CMIP6 global mean NTCF total surface emissions and surface $CH_4$ concentrations for the four scenarios.

**Table 3.1:** Model configurations for present-day and future simulations. "Emissions" refers to emissions of $O_3$ precursors and aerosols. "$CH_4$ conc." refers to prescribed surface $CH_4$ concentrations. "SST/SI" refers to prescribed sea surface temperature and sea ice concentrations. "Historical" means that the emissions, $CH_4$ concentrations or SST/SI evolve as for the CMIP6 historical simulations, and "Reference" means that they evolve as for SSP3-7.0. "Low" emissions or $CH_4$ concentrations evolve following SSP3-7.0 but with lower emissions or $CH_4$ concentrations.

| Experiment name | Time period | Emissions | $CH_4$ conc. | SST/SI |
|---|---|---|---|---|
| Present day | 2004–2014 | Historical | Historical | Historical |
| SSP370 | 2045–2055 | Reference | Reference | Reference |
| SSP370_lowNTCF | 2045–2055 | Low | Reference | Reference |
| SSP370_lowCH4 | 2045–2055 | Reference | Low | Reference |

**Table 3.2:** Overview of global annual mean time-varying surface emissions of $NO_x$, VOCs, CO, sulfur dioxide ($SO_2$), black carbon (BC) and organic carbon (OC) from anthropogenic (ANT), biomass burning (BB), biogenic (BIO) sources for the present day (2004–2014) and future (2045–2055) SSP3-7.0, SSP3-7.0-lowNTCF and SSP3-7.0-lowCH4. Annual mean surface $CH_4$ mixing ratios (ppb) are also shown.

| Emission ($Tg\ yr^{-1}$) | | Present day | SSP3-7.0 | SSP3-7.0-lowNTCF | SSP3-7.0-lowCH4 |
|---|---|---|---|---|---|
| $NO_x$ | ANT | 136.0 | 149.6 | 68.8 | 149.6 |
| | BB | 13.6 | 12.1 | 10.2 | 12.1 |
| | Total | 149.6 | 161.7 | 79.0 | 161.7 |
| VOCs | ANT | 156.3 | 195.3 | 117.6 | 195.3 |
| | BB | 62.7 | 57.1 | 47.5 | 57.1 |
| | BIO | 727.9 | 786.1 | 795.2 | 785.7 |
| | Total | 946.9 | 1038.5 | 960.3 | 1038.1 |
| CO | ANT | 600.8 | 662.7 | 328.4 | 662.7 |
| | BB | 324.6 | 318.5 | 264.5 | 318.5 |
| | Total | 925.4 | 981.2 | 592.9 | 981.2 |
| $SO_2$ | ANT | 115.4 | 95.7 | 43.0 | 95.7 |
| | BB | 2.1 | 2.2 | 1.8 | 2.2 |
| | Total | 117.5 | 97.9 | 44.8 | 97.9 |
| BC | ANT | 7.4 | 9.1 | 4.4 | 9.1 |
| | BB | 1.7 | 1.7 | 1.4 | 1.7 |
| | Total | 9.1 | 10.8 | 5.8 | 10.8 |
| OC | ANT | 18.0 | 23.3 | 10.1 | 23.3 |
| | BB | 15.0 | 14.5 | 11.9 | 14.5 |
| | Total | 33.0 | 37.8 | 22.0 | 37.8 |
| $CH_4$ (ppb) | | 1802.8 | 2471.9 | 2471.9 | 1363.7 |

### 3.2.3 $O_3$ sensitivity indicators

A number of different indicators have been used to distinguish $O_3$ sensitivity regimes, and typical indicators are the ratios of $NO_x$/VOC concentrations or emissions and the ratio of $HNO_3/H_2O_2$ concentrations (Kleinman, 1994; Sillman, 1999). For the $NO_x$/VOC ratio, it is often more appropriate to use concentrations than emissions because this accounts for emissions, transport, chemical reactions and deposition. Indicators based on $HNO_3/H_2O_2$ concentration ratios also account for differences in photochemical conditions and VOC reactivity. In a previous study we found that $O_3$ sensitivity regimes diagnosed with $HNO_3/H_2O_2$ and $NO_x$/VOC ratios were similar (Liu et al., 2021). However, the $HNO_3/H_2O_2$ indicator is more sensitive to uncertainties in chemical mechanism, and studies have shown that there are errors in the simulation of short-lived radicals in polluted areas (Whalley et al., 2021). We hence choose the ratio between $NO_x$ and VOC concentrations as a simple indicator of $O_3$ sensitivity indicator in this study.

We quantify the sensitivity of $O_3$ to $NO_x$ and VOC concentrations by examining monthly mean $O_3$ mixing ratios and $O_3$ net production in each UKESM1 surface grid cell in each of the scenarios in turn. This provides a global overview of the dependence of $O_3$ and its production on $NO_x$ and VOC across different environments. It also allows us to determine a globally-averaged critical threshold value distinguishing $NO_x$-limited and VOC-limited regimes.

We note that dilution of species over coarse resolution model grid cells may lead to the underestimation of local concentrations in high-emission regions. Due to the relatively short lifetime of $NO_x$, this likely results in underestimation of $NO_x$/VOC ratios in these conditions and the regimes may thus be more VOC-limited in reality than are able to simulate in a global

model.

## 3.3 Model evaluation of tropospheric and surface $O_3$

### 3.3.1 Comparison of StratTrop and extended chemistry schemes

We first compare averaged tropospheric $O_3$ burdens, chemical lifetime, chemical production, chemical loss and deposition during 2004–2014 from the extended chemistry scheme (Ext_StratTrop) with those from the StratTrop chemistry scheme used in AerChemMIP simulations (Table 3.3). We define the $O_3$ production rate as the sum of reactions fluxes through $HO_2/RO_2$ + NO, and the $O_3$ loss rate as the sum of $O(^1D) + H_2O$, $O_3 + HO_2/OH/alkenes$. The $O_3$ burden with the extended chemistry scheme (376 Tg) lies at the upper end of the uncertainty range for the observed burden, 340 ± 34 Tg for 2000 (Archibald et al., 2020b). The magnitude of the $O_3$ burden is also consistent with the CMIP6 multi-model mean burden of 356 ± 31 Tg for 2005–2014 (Griffiths et al., 2021). The extended chemistry scheme produces a 5 % higher tropospheric $O_3$ burden than that of StratTrop (358 Tg), demonstrating a more reactive environment for net $O_3$ formation throughout the troposphere due to reactive VOCs. This is also reflected in the higher rates of chemical $O_3$ production (11 %), loss (6 %) and deposition (6 %) with the extended chemistry scheme. However, the higher $O_3$ production is offset by greater $O_3$ destruction and by faster $O_3$ deposition, and hence the mean $O_3$ chemical lifetime remains very similar at about 22 days, which is consistent with previous multi-model estimates of the mean lifetime of 22.2 ± 2.2 days

(Stevenson et al., 2006).

**Table 3.3:** Comparison of tropospheric $O_3$ burden and budget terms during 2004–2014 simulated with StratTrop and Ext_StratTrop chemistry schemes in UKCA. One standard deviation in the annual terms over the 2004–2014 period is shown. We define the tropopause based on the highest layer with an $O_3$ mixing ratio less than 150 ppb.

| | StratTrop | Ext_StratTrop |
|---|---|---|
| $O_3$ burden (Tg) | 358±3 | 376±3 |
| $O_3$ lifetime (days) | 22.6±0.2 | 22.5±0.2 |
| $O_3$ net production (Tg year$^{-1}$) | 895±45 | 996±40 |
| $O_3$ production (Tg year$^{-1}$) | 5698±40 | 6080±66 |
| $O_3$ loss (Tg year$^{-1}$) | 4803±45 | 5084±59 |
| $O_3$ deposition (Tg year$^{-1}$) | 883±9 | 936±9 |

Simulated surface $O_3$ concentrations during 2004–2014 with the two chemistry schemes are compared in Fig. 3.1. Using the extended chemistry scheme, the spatial distribution of surface $O_3$ is similar to that using StratTrop in both winter and summer, but shows a general increase in global $O_3$ levels of about 2 ppb (Fig. 3.1a–d) due to inclusion of the additional reactive VOCs. The applied vertical emission profiles may lead to a decrease in the concentrations of $O_3$ precursors and $O_3$ in some areas. The $O_3$ increases (Fig. 3.1e–f) are most notable for South Asia and East Asia due to the relatively high VOC emissions in these regions (Janssens-Maenhout et al., 2015; Huang et al., 2017; Feng et al., 2020). There is a much larger $O_3$ increase in South Asia in winter than in summer (Fig. 3.1e), mainly due to greater transport of $O_3$ precursors during the summer monsoon in South Asia (Lu et al., 2018b). This leads to higher $O_3$ concentrations in winter than that in summer, consistent with Gao et al. (2020), and demonstrates a larger seasonal variation in $O_3$ concentrations with the Ext_StratTrop chemistry scheme than with the StratTrop chemistry scheme. In addition, there are substantial $O_3$ increases in East Asia and in other polluted continents in summer (Fig. 3.1f) when using the extended chemistry scheme. This is not seen in winter (Fig. 3.1e) because titration of $O_3$ by nitric oxide (NO) remains strong, despite high VOC emissions. The relatively small influence of the additional VOCs on $O_3$ in winter is also seen in other heavily populated regions that have high $NO_x$ emissions such as North America and Europe.

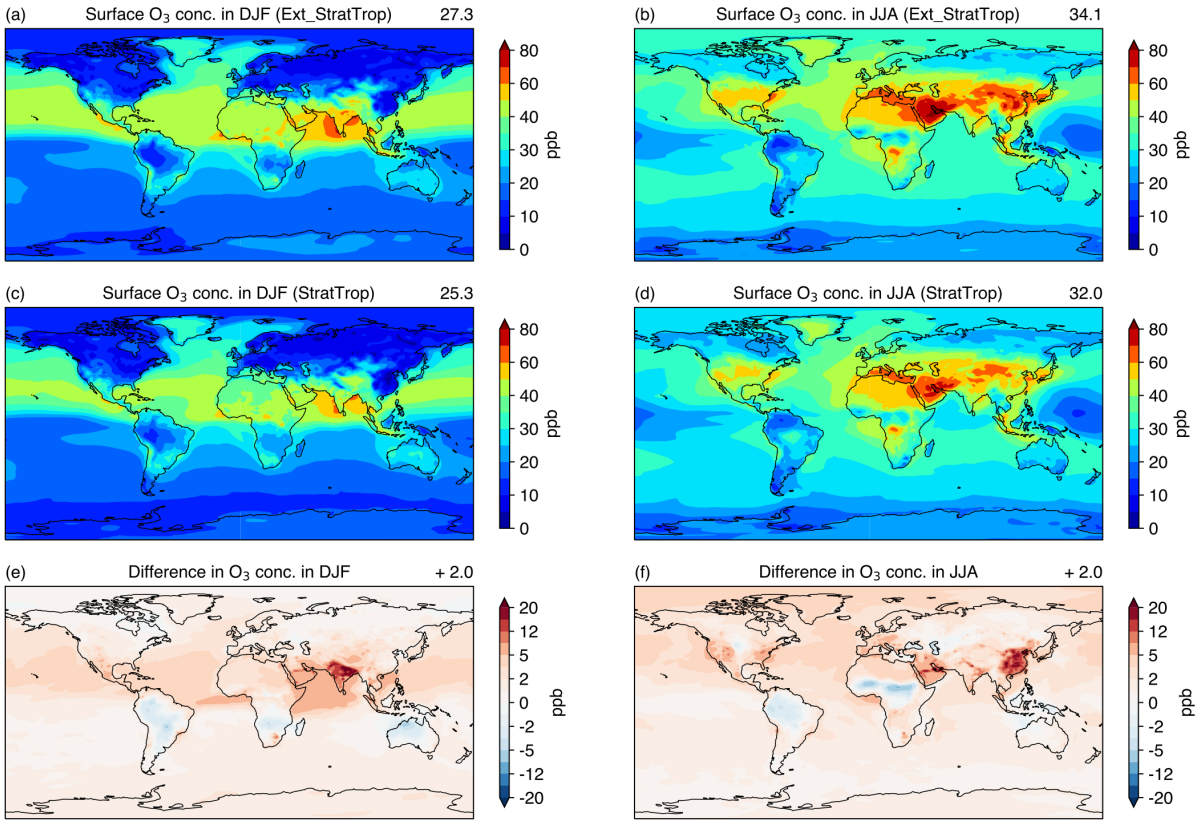


**Figure 3.1:** Comparison of present-day seasonal mean surface $O_3$ concentrations (2004–2014) between the Ext_StratTrop chemistry scheme **(a, b)** and the StratTrop chemistry scheme **(c, d)**. Winter time (December–January–February, DJF) and summer time (June–July–August, JJA) global mean $O_3$ concentrations are shown. Seasonal differences in surface $O_3$ concentrations between the two chemistry schemes are shown in the bottom panels **(e, f)**.

### 3.3.2 Evaluation of surface $O_3$ concentrations

We now evaluate surface $O_3$ concentrations simulated with the Ext_StratTrop chemistry scheme against gridded monthly mean rural observations from the TOAR dataset over the 2004–2014 period (Schultz et al., 2017). Surface $O_3$ concentrations for winter (DJF) and summer (JJA) during 2004–2014 are shown in Fig. 3.2. We find that global mean surface $O_3$ mixing ratios are underestimated in winter (-7.3 ppb) and overestimated in summer (+13.5 ppb), with relatively small biases in spring and autumn. The positive biases in summer and negative biases in winter for $O_3$ concentrations are also seen in results using the StratTrop chemistry scheme (Archibald et al., 2020b; Turnock et al., 2020). The model seasonality with both schemes (19.4–45.5 ppb; DJF-JJA) is rather stronger than that observed (26.7–32.0 ppb; DJF-JJA), but the Ext_StratTrop chemistry scheme improves the model performance slightly in DJF for surface $O_3$ (Fig. 3.2b) despite larger biases in summer (Fig. 3.2d). Numerical diffusion of $O_3$ precursor emissions due to coarse model horizontal resolution may explain the biases (Wild and Prather, 2006; Stock et al., 2014; Fenech et al., 2018), and we note that these seasonal $O_3$ biases are also evident in other chemistry-climate models (Young et al., 2018b; Turnock et al., 2020). Insufficient turbulent mixing in the planetary boundary layer may also contribute to the bias (O'Connor et al., 2014), as accumulation of $NO_x$ at the surface leads to greater $O_3$ production in summer and greater titration by NO in winter. However, we note that a much more comprehensive chemistry scheme applied in UKCA, the Common Representative Intermediates Mechanism (CRI-Strat), shows similar systematic biases in surface $O_3$ mixing ratios, -4.6 ppb in DJF and +12.0 ppb in JJA for the 2010–2018 period (Archer-Nicholls et al., 2020). This suggests that other biases in the model are primarily responsible for the biases in surface $O_3$. We

choose to apply the extended chemistry scheme as it permits representation of a more appropriate chemical environment for $O_3$ production in high-emission areas and is thus more suitable to investigate $O_3$ sensitivity.

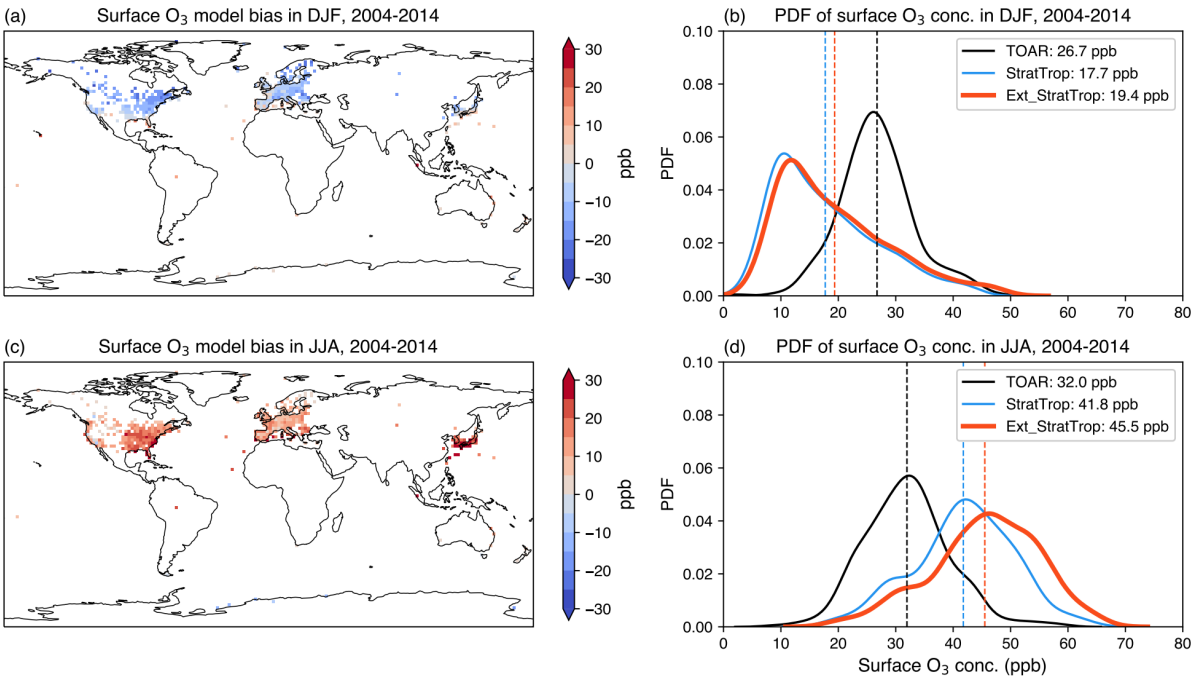


**Figure 3.2:** Modelled surface $O_3$ biases with the Ext_StratTrop chemistry scheme for winter (DJF) and summer (JJA) over 2004–2014 **(a, c)**. Probability distribution function (PDF) of seasonal mean $O_3$ concentrations between observations, StratTrop and Ext_StratTrop chemistry schemes **(b, d)**. Vertical dashed lines indicate seasonal mean surface $O_3$ concentrations. Observations from the Tropospheric Ozone Assessment Report (TOAR) dataset (Schultz et al., 2017) are used for comparison.

## 3.4 $O_3$ changes under future scenarios

### 3.4.1 Emission changes

The SSP3-7.0 pathway is characterized by relatively strong emission controls in some parts of the world such as North America and Europe but weaker controls or emission increases elsewhere. Increases in $NO_x$ and VOC emissions from anthropogenic and biomass burning sources are seen in Central and South America, North Africa, the Middle East, and South and East Asia (Fig. 3.3a, c). SSP3-7.0-lowCH4 has the same NTCF emissions as SSP3-7.0 but lower $CH_4$ emissions that lead to lower $CH_4$ concentrations (Table 3.2). SSP3-7.0-lowNTCF represents strong emission controls across the globe, with reductions in emissions in most major high-emission regions except for South Asia (Fig. 3.3b, d). Total BVOC emission changes are driven by changes in land-use, vegetation and temperature. Fig. 3.3e, f shows general increases in total BVOC emissions in most parts of the Northern Hemisphere except for South Asia in the future, which partly offset the decreased anthropogenic and biomass burning VOC emissions in North America and Europe. Similar BVOC emission changes are found under SSP3-7.0 and SSP3-7.0-lowNTCF relative to the present day as the climate change signal and carbon dioxide concentrations under future pathways are the same.

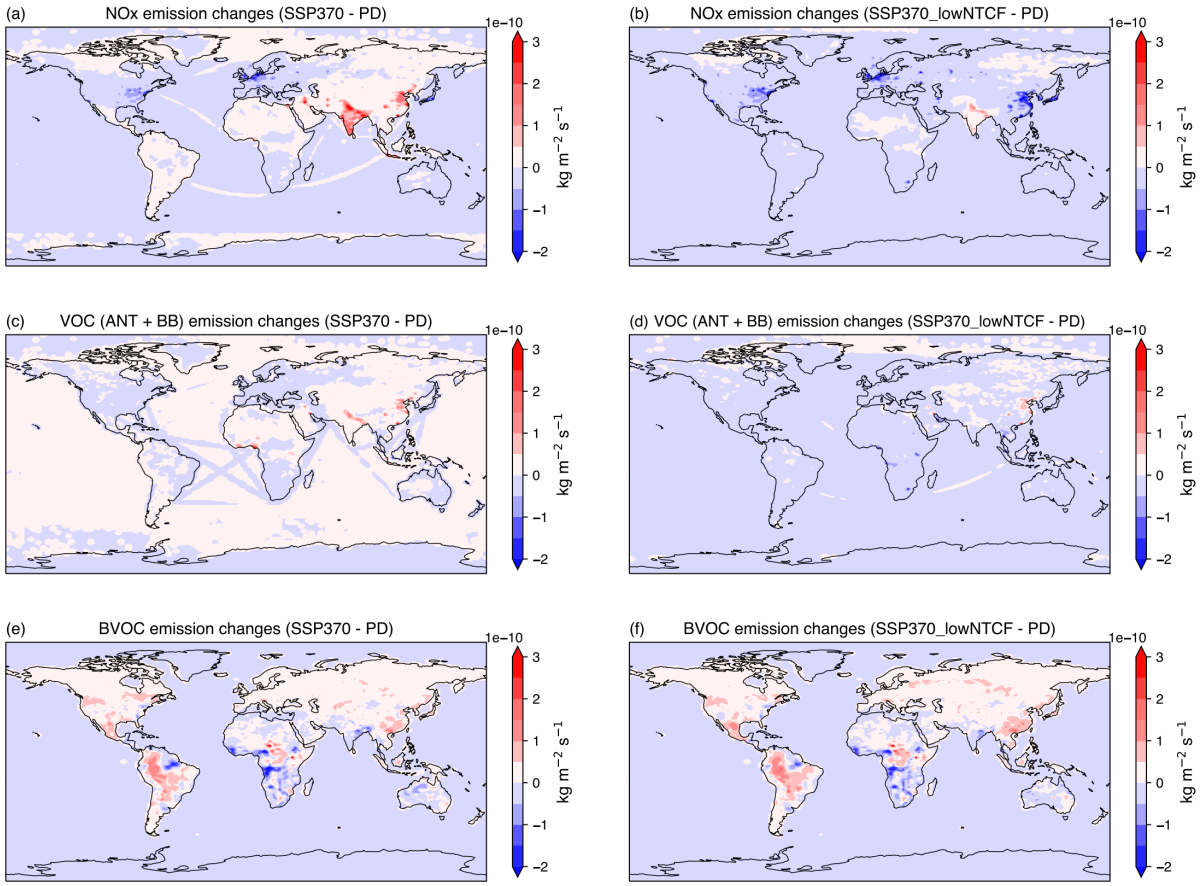


**Figure 3.3:** Differences in annual mean surface emissions of $NO_x$ **(a, b)**, anthropogenic and biomass burning VOCs **(c, d)** and total biogenic VOCs **(e, f)** between the present day (PD; 2004–2014) and SSP3-7.0 and SSP3-7.0-lowNTCF (2045–2055).

### 3.4.2 Tropospheric $O_3$ changes

Changes in tropospheric $O_3$ from the present day to the future are shown in Table 3.4. Changes in NTCF emissions control $O_3$ burden changes with a 4 % increase in the $O_3$ burden under SSP3-7.0 and a 7 % decrease under SSP3-7.0-lowNTCF relative to the present day. Changes in $O_3$ production rates are also controlled by changes in NTCF emissions, and there is higher $O_3$ production under SSP3-7.0 and lower $O_3$ production under SSP3-7.0-lowNTCF. The decrease in the $O_3$ burden (5 %) under SSP3-7.0-lowCH4 is slightly less than that under SSP3-7.0-lowNTCF (7 %), and shows that reductions in $CH_4$ concentrations effectively reduce the tropospheric $O_3$ burden despite high NTCF emissions under SSP3-7.0-lowCH4. $O_3$ production rates under SSP3-7.0-lowCH4 are slightly higher than in the present day partly due to higher hydroxyl radical (OH) concentrations that promote $O_3$ production. However, these higher $O_3$ production rates are offset by higher $O_3$ loss rates, and result in lower $O_3$ net production under SSP3-7.0 and SSP3-7.0-lowCH4. We find that the $O_3$ chemical lifetime decreases slightly by 0.4–1.6 days under future pathways partly due to decreased $O_3$ net production, and partly due to increased $O_3$ loss associated with higher temperature and humidity in a warmer climate (Young et al., 2018b). Changes in $O_3$ dry deposition rates principally reflect changes in surface $O_3$ concentrations, although high temperatures under a warmer climate may reduce $O_3$ deposition rates due to vegetation stress (Lin et al., 2020).

**Table 3.4:** Comparison of the tropospheric $O_3$ budget under present-day (2004–2014) and future conditions (2045–2055).

| | Present day | SSP3-7.0 | SSP3-7.0-lowNTCF | SSP3-7.0-lowCH4 |
|---|---|---|---|---|
| $O_3$ burden (Tg) | 376±3 | 393±5 | 351±7 | 357±6 |
| $O_3$ lifetime (days) | 22.5±0.2 | 20.9±0.1 | 22.1±0.1 | 21.1±0.2 |
| $O_3$ net production (Tg year$^{-1}$) | 996±40 | 934±38 | 638±60 | 869±32 |
| $O_3$ production (Tg year$^{-1}$) | 6080±66 | 6728±43 | 5536±108 | 6108±65 |
| $O_3$ loss (Tg year$^{-1}$) | 5084±59 | 5795±45 | 4898±78 | 5239±56 |
| $O_3$ dry deposition (Tg year$^{-1}$) | 936±9 | 961±9 | 810±19 | 856±14 |

### 3.4.3 Surface seasonal $O_3$ changes

Seasonal differences in simulated surface $O_3$ concentrations between the present day (2004–2014) and future pathways (2045–2055) are shown in Fig. 3.4a–f, along with a comparison between SSP3-7.0 and SSP3-7.0-lowCH4 (Fig. 3.4g, h). SSP3-7.0 represents less stringent emission control policies, and has slightly higher global mean $O_3$ mixing ratios (0.7–0.9 ppb; Fig. 3.4a, b) than the present day. In contrast, tightened emission controls under SSP3-7.0-lowNTCF reduce surface $O_3$ mixing ratios substantially across many parts of the world (3.3–5.2 ppb; Fig. 3.4c, d). The reduction in $CH_4$ mixing ratios from 1803 to 1364 ppb under SSP3-7.0-lowCH4 relative to the present day successfully reduces $O_3$ mixing ratios (2.7–3.5 ppb; Fig. 3.4e, f) for regions that show $O_3$ increases under SSP3-7.0. SSP3-7.0-lowCH4 with reduced $CH_4$ concentrations alone shows uniform $O_3$ decreases across the globe (3.4–4.4 ppb; Fig. 3.4g, h) compared with SSP3-7.0, where mean $CH_4$ mixing ratios are 2472 ppb, and this offsets high $O_3$ levels in regions with high NTCF emissions. This demonstrates the importance of $CH_4$ in governing surface $O_3$ concentrations, and the need to account for $CH_4$ in mitigating $O_3$ pollution in future (Fiore et al., 2008; Allen et al., 2021). We highlight that $O_3$ changes vary by season. From Fig. 3.4a, c we can see that $O_3$ concentrations generally increase in winter in continental areas such as North America and Europe under SSP3-7.0 and SSP3-7.0-lowNTCF. These regions have large reductions in NTCF emissions under future pathways, and thus there is less $O_3$ titration due to lower $NO_x$ emissions in these regions. Since $NO_x$ emissions decrease in East Asia under SSP3-7.0-lowNTCF, we also see $O_3$ increases in winter in this region. This highlights that $NO_x$ emission reductions are not beneficial for reducing surface $O_3$ concentrations in winter. Conversely, $NO_x$ emission increases under SSP3-7.0 lead to $O_3$ decreases in winter in South

and East Asia for the same reason. The situation is different in summer, with $O_3$ decreases in North America and Europe, but $O_3$ increases in South and East Asia under SSP3-7.0 (Fig. 3.4b). This reflects a shift in $O_3$ sensitivity from VOC limitation in winter to $NO_x$ limitation in summer. $O_3$ changes in summer and winter are generally consistent in South America and Africa, and reflect $NO_x$ limitation in these regions throughout the year. $O_3$ mixing ratios in the Arctic increase in winter likely due to the transport of $NO_x$ reservoir i.e. PAN from continental areas under low temperature. For regions that are projected to have lower $NO_x$ emissions in SSP3-7.0-lowNTCF, such as eastern China, we note that $O_3$ concentrations increase in both winter and summer. The industrial regions of China are in VOC limited regimes throughout the year, and thus decreased $NO_x$ emissions increase $O_3$ concentrations (Jin and Holloway, 2015; Wang et al., 2021; Liu et al., 2021). This suggests that reductions in both $NO_x$ and VOC emissions may be needed to reduce $O_3$ in these regions.

Surface $O_3$ concentrations are also influenced by climate change, reflecting changing natural emissions, $O_3$ production and destruction rates and $O_3$ deposition rates (Doherty et al., 2013, 2017). Global annual mean surface $O_3$ mixing ratios decrease by 1 ppb with a 1.5 °C temperature rise, but show little change in continental areas (Naik et al., 2021). This is principally due to increased humidity and greater $O_3$ destruction in oceanic areas, but in continental areas these effects may be offset by $O_3$ increases due to higher soil $NO_x$ (Romer et al., 2018) and BVOC emissions, and by decreased $O_3$ deposition rates (Lin et al., 2020). $O_3$ concentrations can also be impacted by more frequent and intense heat waves under a warmer climate (Schnell and Prather, 2017; Ma et al., 2019). We find that the resulting changes in surface $O_3$ concentrations in continental regions due to climate change are

relatively small, and reduction in anthropogenic emissions is the dominant factor governing surface $O_3$ concentrations in the near future.

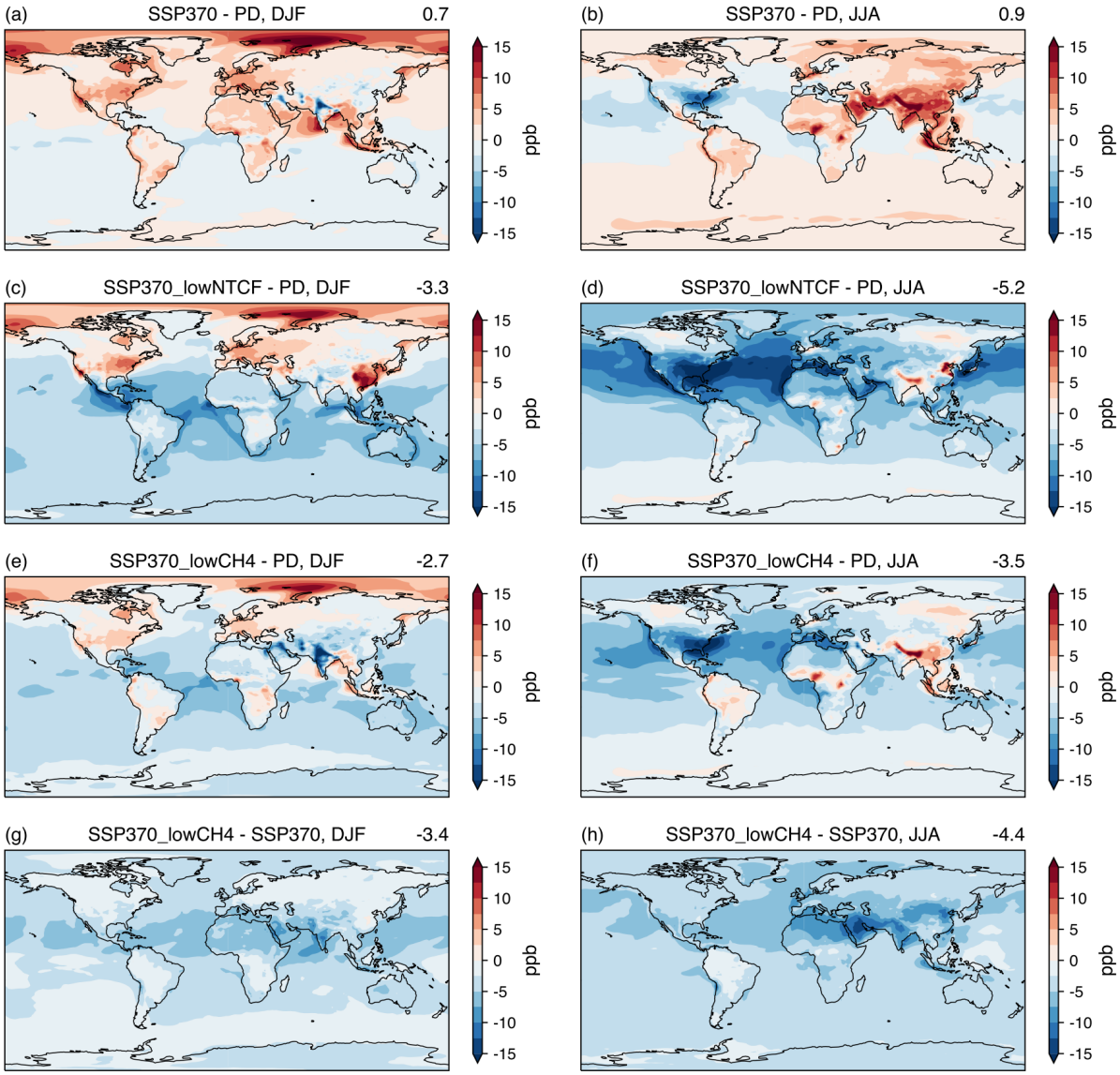


**Figure 3.4:** Differences in seasonal mean surface $O_3$ concentrations between the present day (PD; 2004–2014) and the future SSP3-7.0 **(a, b)**, SSP3-7.0-lowNTCF **(c, d)** and SSP3-7.0-lowCH4 **(e, f)** (2045–2055) in winter (DJF) and summer (JJA). Differences between SSP3-7.0 and SSP3-7.0-lowCH4 are shown **(g, f)** to isolate the impacts of reduced $CH_4$ concentrations. Absolute global mean $O_3$ changes (ppb) are shown at the right top of each panel.

We also examine daytime and nighttime $O_3$ changes for different regions under future pathways because daytime $O_3$ concentrations are typically more relevant for human health. For daytime $O_3$ concentrations we consider the maximum daily average 8h $O_3$ concentration (MDA8), an important metric used to evaluate $O_3$ impacts on human health. Nighttime $O_3$ concentrations are correspondingly given by the minimum daily average 8h $O_3$ concentration (MIN8). We show a comparison of the changes in these metrics in Fig. 5.

In general, differences in global mean $O_3$ changes are relatively small in both daytime and nighttime under all pathways. However, in South and East Asia with increased $NO_x$ emissions under SSP3-7.0 and SSP3-7.0-lowCH4, $O_3$ concentrations tend to increase in daytime but show smaller increases or reduction at night. This demonstrates the impact of $O_3$ titration by NO at nighttime in high-$NO_x$ environments. In North America and Europe that have lower $NO_x$ emissions in the future, daytime $O_3$ concentrations decrease greatly in summer, but daytime and nighttime changes are similar in winter, demonstrating the large influence of $NO_x$ emissions on summer daytime $O_3$ concentrations. The substantial differences between daytime and nighttime $O_3$ changes suggest that the underlying impacts of $O_3$ changes on human health are likely to be larger than those estimated using seasonal mean $O_3$ concentrations, and this is particularly important for high-emission areas with increased $NO_x$ emissions in the future.

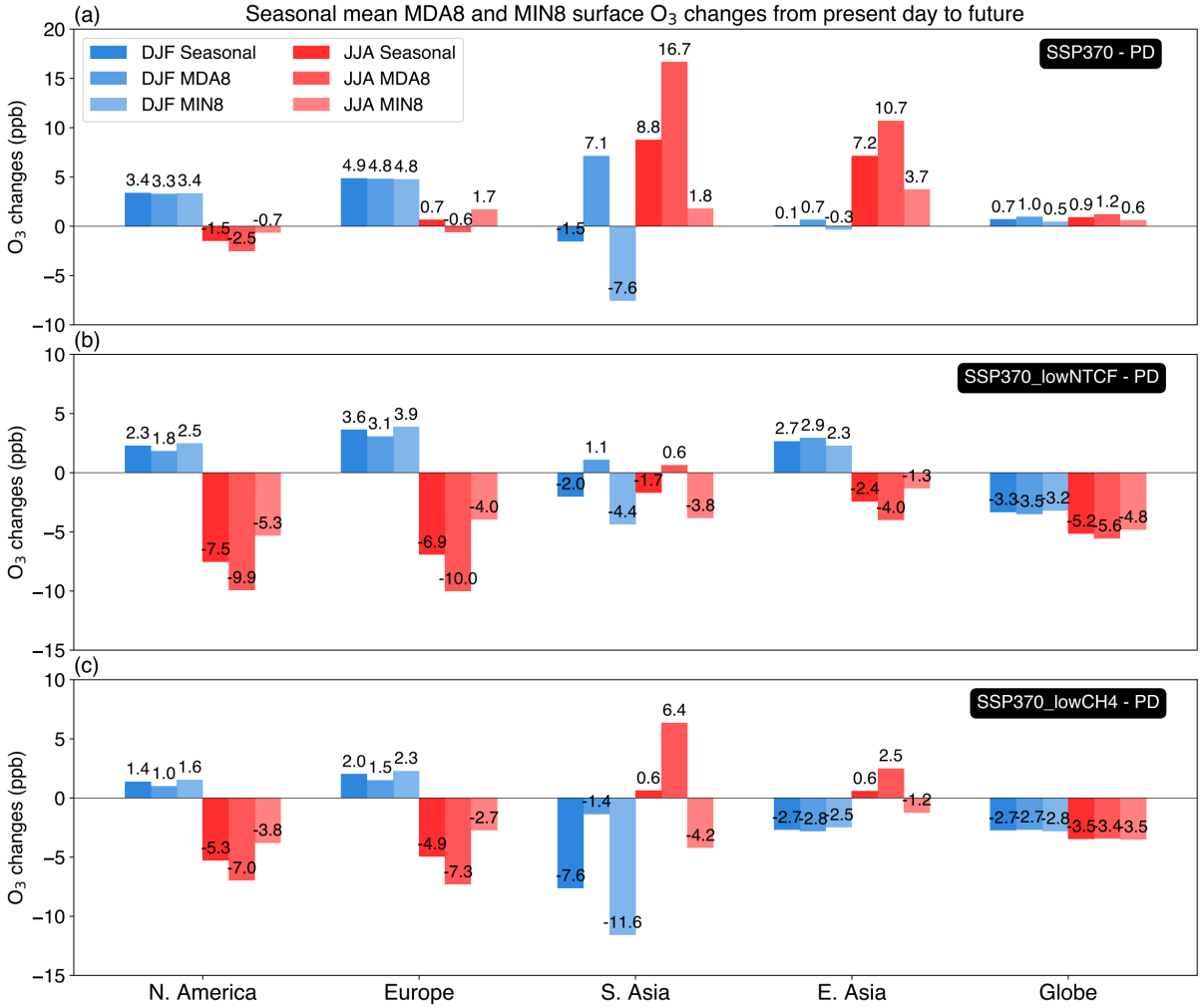


**Figure 3.5:** Seasonal mean maximum daily average 8h (MDA8) and minimum daily average 8h (MIN8) surface $O_3$ changes for North America, Europe, South Asia, East Asia and the globe from the present day (PD; 2004–2014) to SSP3-7.0 **(a)**, SSP3-7.0-lowNTCF **(b)** and SSP3-7.0-lowCH4 **(c)** (2045–2055). DJF and JJA situations are shown with blue and red bars, respectively.

## 3.5 $O_3$ sensitivity in the present day and the future

Non-linearity in chemical $O_3$ formation can result in differences in the effectiveness of emission control strategies regionally, and may even aggravate $O_3$ pollution issues. We therefore investigate $O_3$ sensitivity for the present day and the future, as it is important to understand how $O_3$ concentrations will respond to changing emissions. Ratios of $NO_x$ and VOC concentrations provide a useful indicator of regional $O_3$ sensitivity regimes. Here we quantify the critical $NO_x$/VOC ratio that distinguishes VOC-limited and $NO_x$-limited regimes by examining monthly mean surface $O_3$ concentrations and net chemical production rates as a function of monthly mean $NO_x$ and VOC concentrations, see Fig. 3.6. Monthly mean $O_3$ mixing ratios and net production rates in the lowest model layer from all months and all scenarios are used to plot the figure. For $NO_x$ we use the sum of NO and $NO_2$ mixing ratios, and for total VOC we use the sum of the mixing ratios of primary emitted VOC species. CO and $CH_4$ are not included due to their relatively low reactivity. We classify $NO_x$ and VOC mixing ratios in each model grid cell into 150 bins on a logarithmic scale ranging from 0.01 ppb to 100 ppb, and calculate mean $O_3$ mixing ratios and mean $O_3$ net chemical production rates in each $NO_x$-VOC bin. Approximate thresholds of monthly mean $NO_x$/VOC ratios for $O_3$ sensitivity are shown in Fig. 3.6, ranging from 0.6 to 1 with a central value of 0.8. This value can be applied for both the $O_3$ mixing ratio isopleth and the $O_3$ net chemical production rate isopleth, suggesting that it is robust in distinguishing $O_3$ sensitivity regimes. We hence apply a threshold value of 0.8 to distinguish $O_3$ sensitivity regimes hereafter. Areas above the threshold represent VOC-limited regimes in which increased $NO_x$

emissions reduce $O_3$ concentrations and $O_3$ production rates, and areas below the threshold represent $NO_x$-limited regimes. We find the highest $O_3$ concentrations and $O_3$ production close to the threshold line, demonstrating that the threshold values are consistent and that the approach is robust.

We further investigate $O_3$ sensitivity for different regions. The regions considered here are those defined for the Task Force on Hemispheric Transport of Air Pollutants Phase 2 (TF HTAP2; Janssens-Maenhout et al., 2015), see Fig. 3.7a; the regions dominating each part of the $NO_x$-VOC concentration space are shown in Fig. 3.7b, c. We determine the dominant region contributing to each bin in $NO_x$-VOC space based on the region contributing the greatest number of model grid cells to that bin. This approach reveals differences in regional $O_3$ sensitivity. We also show the shift in $O_3$ sensitivity in different regions between the present day (Fig. 3.7b) and the future (SSP3-7.0-lowNTCF; Fig. 3.7c) to demonstrate the impacts of decreased NTCF emissions on the evolution of $O_3$ sensitivity on a regional basis.

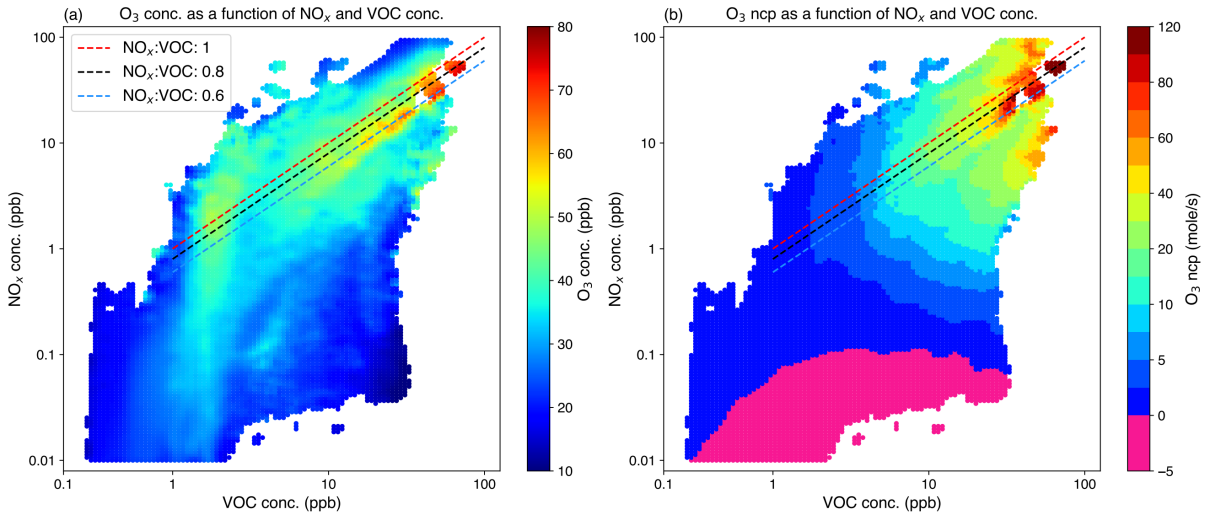


**Figure 3.6:** Surface $O_3$ mixing ratios **(a)** and $O_3$ net chemical production (ncp) rates **(b)** as a function of monthly mean $NO_x$ and VOC mixing ratios. Monthly mean data for all months and all scenarios are used. The straight lines show the approximate thresholds of $NO_x$/VOC to distinguish VOC-limited (above the line) and $NO_x$-limited (below the line) regimes.

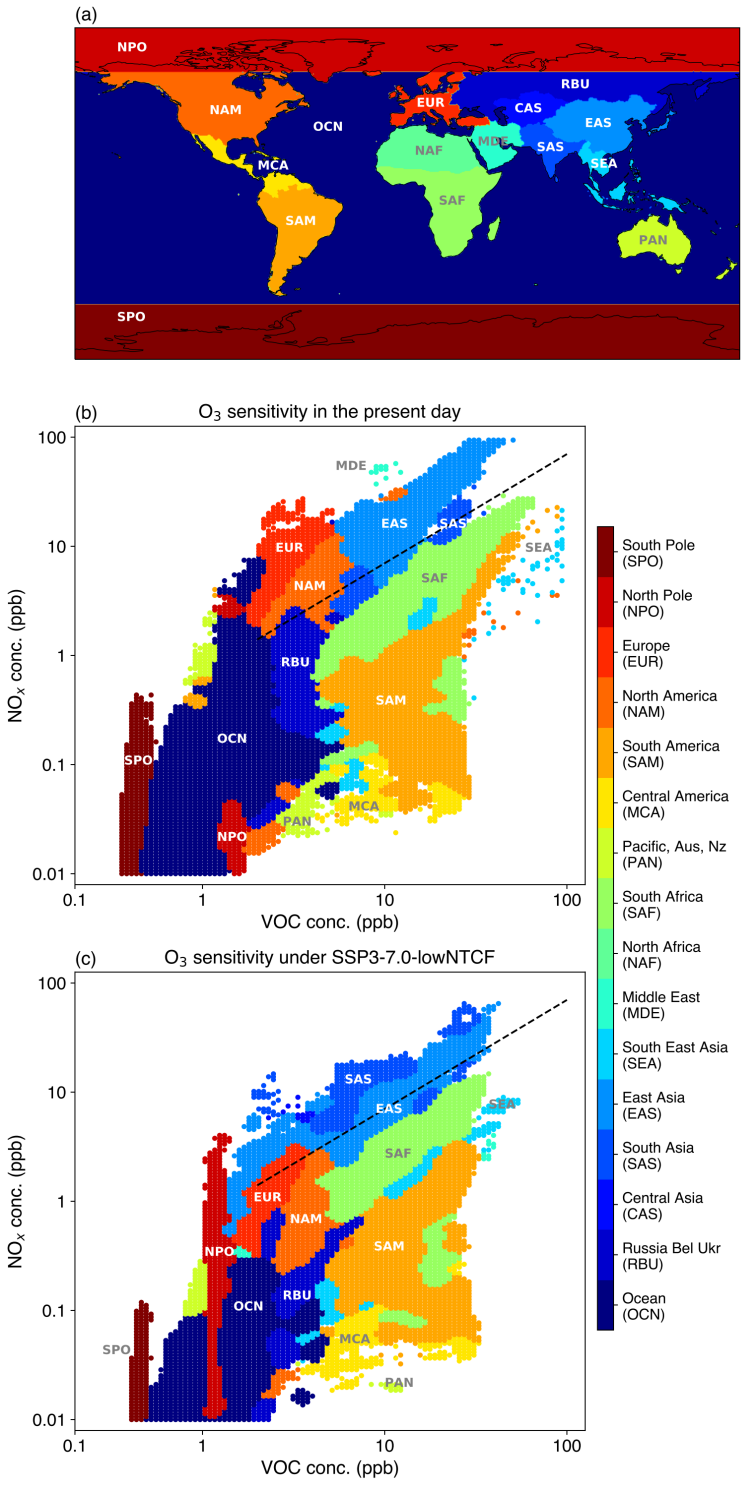


**Figure 3.7:** Geographical regions defined in the Task Force on Hemispheric Transport of Air Pollutants Phase 2 (TF HTAP2) **(a)**. Regions that have the largest number of grid points in each part of $NO_x$-VOC concentration space are shown in the present day **(b)** and under SSP3-7.0-lowNTCF **(c)**. The straight line shows the $NO_x$/VOC threshold of 0.8. Monthly mean data for all months under each pathway are used to plot **(b)** and **(c)**.

Figure 3.7b clearly shows that low-$NO_x$ and low-VOC environments are most common in oceanic and polar regions where surface $O_3$ levels are typically low and where $O_3$ production is $NO_x$-limited. In contrast, Europe, North America and East Asia dominate the high-$NO_x$ and high-VOC environments in the present day where $O_3$ levels are high and $O_3$ production is VOC-limited. Europe and North America have similar VOC concentrations but $NO_x$ concentrations are generally higher in Europe than in North America, which results in Europe lying further above the $NO_x$/VOC threshold. This demonstrates that stricter controls on $NO_x$ emissions are required for Europe to shift from VOC-limited to $NO_x$-limited regimes than for North America. East Asia dominates VOC-limited regimes due to much higher $NO_x$ and VOC concentrations than other regions. Parts of South Asia and Middle East are also VOC-limited. Major biogenic emission source regions such as South America, South Africa and South East Asia have high VOC concentrations but moderate levels of $NO_x$, and the chemical environment is therefore $NO_x$-limited.

The impacts of reductions in NTCF emissions are shown in Fig. 3.7c. We find that Europe and North America are no longer the most dominant VOC-limited regimes due to decreased $NO_x$ concentrations. East Asia is still a dominant VOC-limited region under SSP3-7.0-lowNTCF, but reduced $NO_x$ emissions shift parts of East Asia into $NO_x$-limitation. South Asia becomes the main VOC-limited region with relatively high $NO_x$ concentrations. South America, South Africa and South East Asia are still $NO_x$-limited because there are no large $NO_x$ increases in these regions.

$O_3$ sensitivity in major present-day VOC-limited regions under different scenarios are shown in Fig. 3.8. Reductions in $NO_x$ emissions are important and effective in transforming VOC-limitation to $NO_x$-limitation, reflected in

large $NO_x$-limited areas in Europe and North America under all scenarios. In contrast, most parts of East Asia are VOC-limited under SSP3-7.0 and SSP3-7.0-lowCH4 due to increased $NO_x$ emissions. Since changes in VOC concentrations are relatively small for all scenarios, they have little substantial influence on $O_3$ sensitivity. Under future climate, increased biogenic VOC emissions in Europe and North America partly offset decreased anthropogenic VOC emissions, and are hence beneficial to maintain a $NO_x$-limited environment. We note that South Asia is the only region that is substantially VOC-limited in the future due to increased $NO_x$ emissions. Reductions in $CH_4$ concentrations have relatively little impact on $O_3$ sensitivity, although they greatly reduce surface $O_3$ concentrations (Sect. 3.4.3).

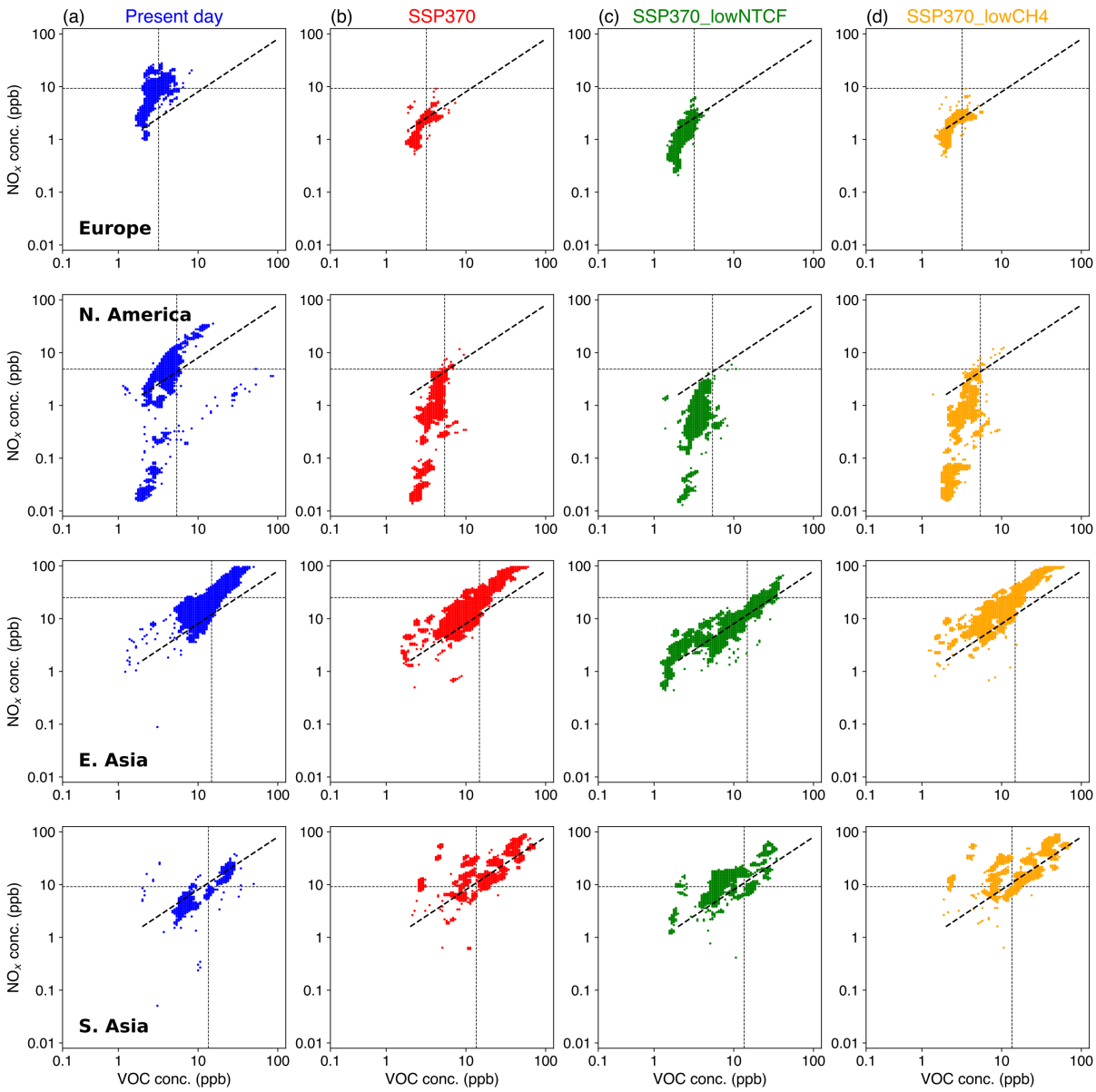


**Figure 3.8:** $O_3$ sensitivity across Europe, North America, East Asia and South Asia in the present day **(a)** and under SSP3-7.0 **(b)**, SSP3-7.0-lowNTCF **(c)** and SSP3-7.0-lowCH4 **(d)**. The $NO_x$/VOC threshold of 0.8 is shown. Horizontal and vertical lines indicate regional mean $NO_x$ and VOC concentrations in the present day.

## 3.6 Spatial distributions of $O_3$ sensitivity

Global spatial distributions of annual $O_3$ sensitivity in the present day and the future are shown in Fig. 3.9. VOC-limited regimes are represented by high $NO_x$/VOC ratios, reflecting relatively high $NO_x$ or low VOC concentrations. In the present day, high $NO_x$ emissions contribute to VOC-limitation in large areas of North America, Western and Central Europe and East Asia. While North America and Europe have lower $NO_x$ concentrations than East Asia, lower VOC concentrations still lead to VOC-limitation. Only southwest parts of India are VOC-limited. In the future, $O_3$ production in more areas of North America and Europe becomes $NO_x$-limited. However, VOC limited regimes in East Asia, particularly China, are persistent due to projected increases in $NO_x$ emissions until 2055 under SSP3-7.0 and SSP3-7.0-lowCH4. We find that reductions in $CH_4$ concentrations have relatively little influence on $O_3$ sensitivity over continental regions (Fig. 3.9b vs 3.9d). We note that SSP3-7.0-lowNTCF shows the smallest VOC-limited areas across the globe. East Asia is still partly VOC-limited under this scenario, particularly in northern China (Fig. 3.9c), which indicates that further reductions in $NO_x$ emissions are required in addition to those expected in this region in the future (Fig. 3.3b).

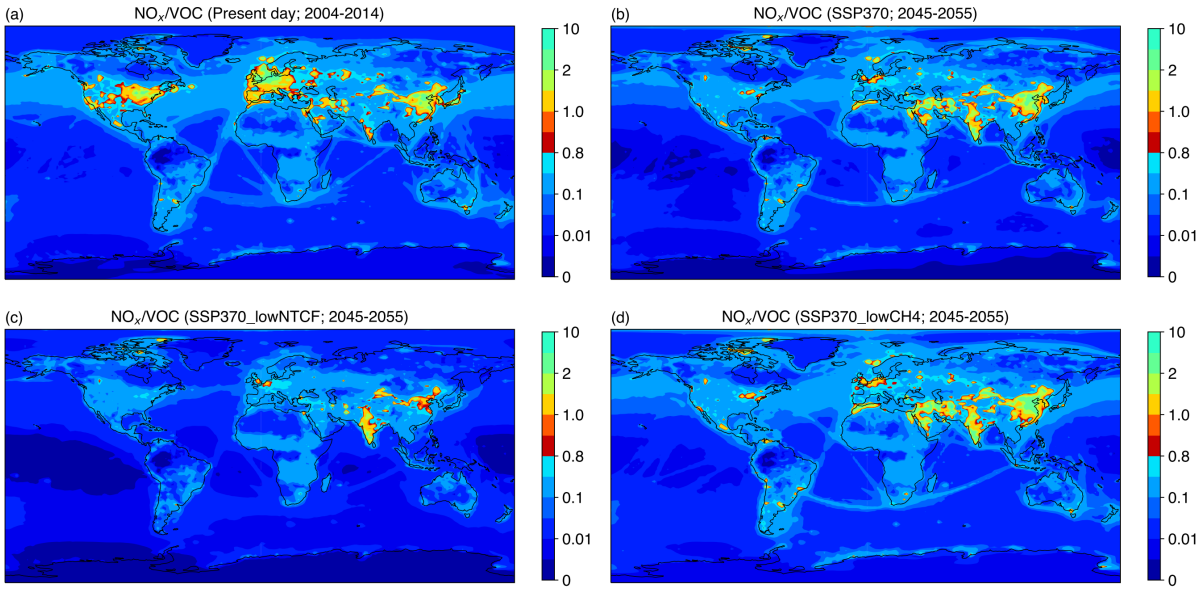


**Figure 3.9:** Spatial distributions of annual mean $NO_x$/VOC in the present day (2004–2014; **a**) and under SSP3-7.0 **(b)**, SSP3-7.0-lowNTCF **(c)** and SSP3-7.0-lowCH4 **(d)** (2045–2055). A $NO_x$/VOC threshold ratio of 0.8 is used here to distinguish $O_3$ sensitivity regimes.

We contrast regional $O_3$ sensitivities for winter and summer seasons in Fig. 3.10, as we note that $O_3$ responses in different seasons can be substantially different in high-emission regions. This suggests that static emission control strategies throughout the year may not be the best way to lower annual-mean $O_3$ pollution, and adjustments may be needed according to seasonal $O_3$ sensitivities. More extensive VOC-limited areas are found in winter than in summer under both present day and future conditions, but these account for less than 7 % of the total area of the world in the present day (Table 3.5). Over 50 % of North America, Europe and East Asia are VOC-limited in winter in the present day. This explains why North America and Europe show $O_3$ increases in winter (Fig. 3.4) despite reduced $NO_x$ emissions. How-

ever, there are fewer VOC-limited regions across the globe under all future pathways (Fig. 3.10). About 1 % of North America is VOC-limited in summer, and less than 7 % of Europe. In contrast, over 48 % (winter) and 39 % (summer) of South Asia is VOC-limited in future. Slightly more areas are VOC-limited under SSP3-7.0-lowCH4 than under SSP3-7.0 (Fig 3.10c, d) principally due to decreased $CH_4$ mixing ratios. Overall, reductions in $NO_x$ emissions are important to reduce $O_3$ production in high-emission regions and shift VOC-limited areas to $NO_x$-limitation but this may lead to higher $O_3$ concentrations in winter without further emission controls on VOC and $CH_4$.

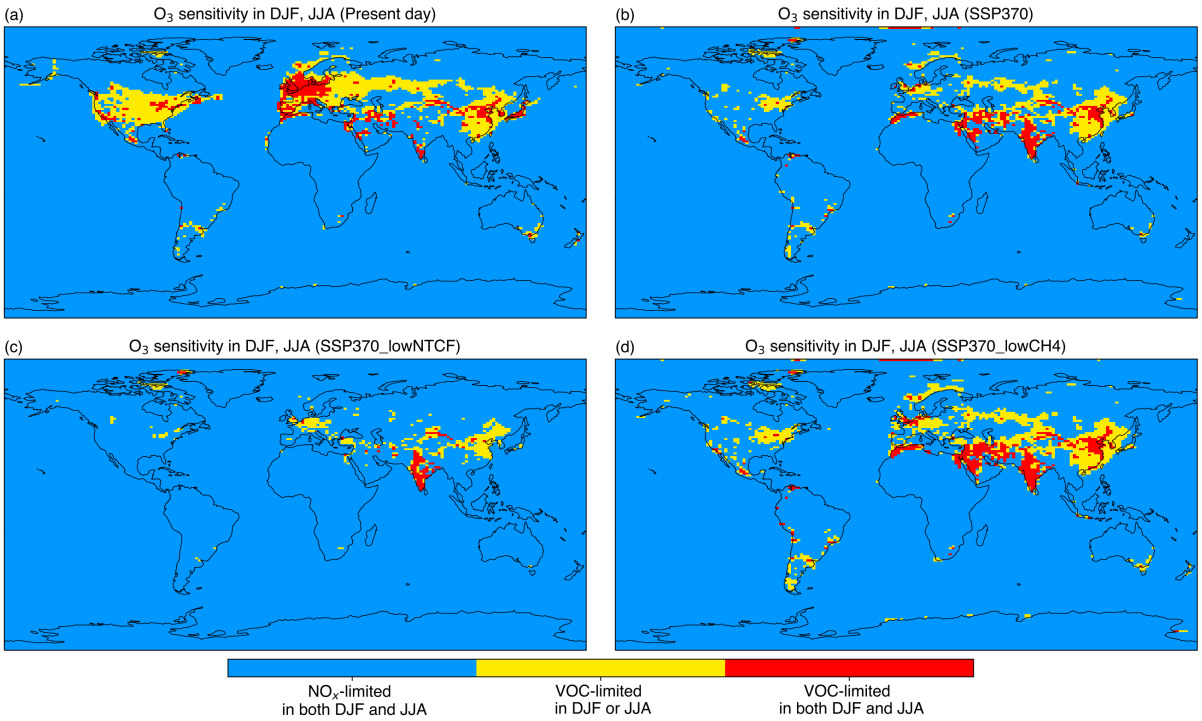


**Figure 3.10:** Seasonal differences in $O_3$ sensitivity regimes for the present day (2004–2014; **a**) and under SSP3-7.0 **(b)**, SSP3-7.0-lowNTCF **(c)**, SSP3-7.0-lowCH4 **(d)** (2045–2055). A $NO_x$/VOC threshold ratio of 0.8 is used here to distinguish $O_3$ sensitivity regimes.

## 3.7 Conclusions

We use a global chemistry-climate model, UKESM1, to assess the impacts of changing near-term climate forcer (NTCF) emissions and $CH_4$ concentrations in the context of climate change on tropospheric $O_3$ in the present day (2004–2014) and the near future (2045–2055). CMIP6 future scenarios including SSP3-7.0, SSP3-7.0-lowNTCF and SSP3-7.0-lowCH4 are used from the AerChemMIP project. We have examined $O_3$ changes from the present day to the future and investigated regional $O_3$ sensitivities to explain contrasting $O_3$ changes in different seasons.

**Table 3.5:** The percentage of VOC-limited areas (%) in different regions under different pathways in winter (DJF) and in summer (JJA).

| | Present day | | SSP3-7.0 | | SSP3-7.0-lowNTCF | | SSP3-7.0-lowCH4 | |
|---|---|---|---|---|---|---|---|---|
| | DJF | JJA | DJF | JJA | DJF | JJA | DJF | JJA |
| N. America | 50.4 | 6.4 | 12.5 | 0.4 | 2.4 | 0 | 16.9 | 1.0 |
| Europe | 79.8 | 37.4 | 27.0 | 2.6 | 27.5 | 0.9 | 41.6 | 6.1 |
| S. Asia | 15.1 | 15.3 | 54.8 | 49.6 | 48.1 | 39.5 | 60.4 | 56.7 |
| E. Asia | 60.3 | 18.3 | 63.3 | 15.8 | 37.7 | 3.5 | 68.7 | 19.3 |
| Globe | 6.9 | 2.7 | 4.8 | 2.0 | 2.0 | 0.6 | 5.9 | 3.0 |

An extended chemistry scheme incorporating more reactive VOC species is used to permit representation of more active photochemical environments for $O_3$ production. This shows higher surface $O_3$ concentrations in high-emission regions and a 5 % higher tropospheric $O_3$ burden. While simulated surface $O_3$ concentrations are biased low in winter and high in summer, these systematic model biases are similar to those using the original chemistry scheme as well as a more comprehensive chemistry scheme. This indicates that other factors in the model are likely to be responsible for the biases but the extended chemistry scheme permits representation of a more appropriate chemical environment for $O_3$ production in high anthropogenic emission areas.

From the present day to the future, the tropospheric $O_3$ burden increases by 4 % under SSP3-7.0 and decreases by 7 % and 5 % under SSP3-7.0-lowNTCF and SSP3-7.0-lowCH4. The tropospheric $O_3$ chemical lifetime remains similar (21–22 days) under all scenarios, and this is similar to previous estimates. Seasonal global mean surface $O_3$ mixing ratios increase by 0.7–0.9 ppb under SSP3-7.0, and decrease by 3.3–5.2 ppb under SSP3-7.0-lowNTCF and

by 2.7–3.5 ppb under SSP3-7.0-lowCH4. We find that reductions in NTCF emissions are effective in reducing surface $O_3$ concentrations, and reductions in $CH_4$ concentrations are also important. We also find that both the magnitude and direction of seasonal, daytime and nighttime $O_3$ changes relative to the present day can vary greatly across different regions especially South and East Asia.

$O_3$ sensitivity is quantified using monthly mean $NO_x$/VOC concentration ratios to give a broad assessment of regional $O_3$ sensitivity. The estimated monthly mean $NO_x$/VOC thresholds range from 0.6 to 1.0, and 0.8 is used to distinguish $O_3$ sensitivity regimes. Most VOC limited regimes occur in high-emission regions across the northern hemisphere, such as North America, Europe, the Middle East, South Asia and East Asia. More areas in North America and Europe become $NO_x$-limited under all future pathways due to the projected decrease in $NO_x$ emissions. There are more VOC-limited areas in East Asia under SSP3-7.0 and SSP3-7.0-lowCH4 due to the projected increase in $NO_x$ emissions, although there are fewer VOC-limited areas in East Asia under SSP3-7.0-lowNTCF. South Asia becomes the dominant region for VOC-limited $O_3$ production in the future. Projections of regional $O_3$ sensitivity demonstrate that reductions in $NO_x$ emissions are the most important factor to shift VOC-limited regimes to $NO_x$-limitation.

We highlight that $O_3$ sensitivity varies by season. There are more VOC-limited regimes in winter (7 %) than in summer (3 %) in both hemispheres. Reductions in $NO_x$ emissions increase surface $O_3$ concentrations in high-emission areas particularly in winter, and reductions in VOC emissions should be targeted. In the future, reductions in $NO_x$ and VOC emissions should both be effective in mitigating $O_3$ pollution in most areas of North America and Europe in summer because there are only 1 % and 7 % VOC-limited areas in

these two regions. However, further reductions in $NO_x$ emissions are needed for parts of East Asia and South Asia to convert most VOC-limited areas to $NO_x$-limited. While anthropogenic and biomass emissions may be controlled in the future, more biogenic emissions under a warmer climate would hinder the impacts of VOCs on $O_3$ mitigation. Reductions in $CH_4$ concentrations are also important to reduce surface $O_3$ pollution. $NO_x$ decreases are important to reduce surface $O_3$ concentrations from a global perspective but will lead to increased $O_3$ concentrations in some regions, and hence emission controls on VOC and $CH_4$ are necessary to mitigate regional $O_3$ pollution during the transition from VOC- to $NO_x$-limitation.

# Chapter 4

# Correcting ozone biases in a global chemistry-climate model: implications for future ozone

This chapter has been submitted to the open-access journal Atmospheric Chemistry and Physics (ACP). It is finished in collaboration with Prof. Ruth Doherty, Prof. Oliver Wild, Dr. Fiona O'Connor and Dr. Steven T. Turnock. ZL, RD, OW designed the study. ZL built the model, conducted model simulations and performed the analysis with input from OW, RD, FO'C and ST. ZL, RD and OW prepared the paper, with contributions from all co-authors.

## 4.1 Introduction

Atmospheric chemical transport models have been developed over several decades with the principal purpose of simulating the composition of the atmosphere (Zhang, 2008), and chemistry schemes have been incorporated in chemistry-climate and Earth system models to investigate the interactions between atmospheric composition and climate change (Flato, 2011). However, current chemistry-climate models are imperfect in simulating the concentration of atmospheric chemical species, even though they represent our latest understanding of the governing physical and chemical processes. Biases obtained through comparison with observations indicate that not all relevant processes can be adequately represented in models, and there are uncertainties associated with emissions, chemistry, transport, deposition, clouds, and aerosols in addition to structural errors associated with model resolution (Knutti and Sedláček, 2013; Archibald et al., 2020b). Representation of these processes may be biased due to poor understanding and simplified parameterisation, and the errors may propagate in complex Earth system models.

While some models reproduce observed concentrations relatively well, this does not confirm that they represent the governing processes well because biases arising from different processes may offset each other. Different models apply differing parameterisations of key processes, and even where these reflect current understanding there may be large differences in model responses to changing conditions (Wild et al., 2020). This may lead to unreliable projections of changes in atmospheric composition under future emission and climate scenarios. However, it is difficult to identify the origin of the biases in models, and this severely hinders model improvement and prevents a full

understanding of the interactions between chemistry and climate through the Earth system.

Tropospheric ozone ($O_3$) is an important greenhouse gas affecting climate, and is a photochemical air pollutant at the Earth's surface, damaging human health and ecosystems (Archibald et al., 2020a). Many studies show that the magnitude of the tropospheric $O_3$ burden and surface $O_3$ concentrations in remote areas can be simulated relatively well (Young et al., 2018b; Griffiths et al., 2021). However, large differences still exist in simulated surface $O_3$ concentrations in high-emission areas (Turnock et al., 2020), and there are large uncertainties in temporal trends (Tarasick et al., 2019) that cannot be captured well by global chemistry-climate models (Parrish et al., 2021). In addition, structural biases in $O_3$ caused by coarse model resolution are hard to eliminate, and typically lead to higher surface $O_3$ concentrations in polluted areas (Wild and Prather, 2006; Stock et al., 2014). Given the difficulty in resolving the $O_3$ biases in a complex chemistry-climate model, the aim of this study is to correct simulations of present day surface $O_3$ concentrations across the globe, and to generate more reliable $O_3$ projections under future scenarios.

Machine learning provides a valuable approach to correct $O_3$ biases. Appropriate algorithms can be applied to identify the relationships between model responses and the driving variables based on extensive training. Deep learning approaches apply algorithms with more complex architectures and larger parameter spaces based on artificial neural networks (Goodfellow et al., 2016). In atmospheric science, machine learning has been successfully applied in some fields such as the prediction of precipitation (Sønderby et al., 2020; Ravuri et al., 2021) and air pollution (Kleinert et al., 2021). Numerical approaches used in solving ordinary and partial differential equations in

chemical and dynamic systems (Han et al., 2018; Keller and Evans, 2019), and in parameterising subgrid processes for clouds in climate models (Rasp et al., 2018) can also be replaced by machine learning to reduce computational costs. However, reliance on machine learning approaches to make predictions may lead to loss of interpretability of the results, and we therefore choose to apply a deep learning model to the output from a chemistry-climate model to gain greater physical insight.

In this study, we explore the application of deep learning to correct surface $O_3$ biases in a global chemistry-climate model for the first time, and apply it to improve projections of changes in $O_3$ under future scenarios. We identify the dominant factors leading to $O_3$ biases with the aim of guiding future model development. We introduce the chemistry-climate model, present-day and future scenarios and the deep learning model in Sect. 4.2. We demonstrate the performance of the deep learning model in Sect. 4.3. We show the importance of different variables to $O_3$ biases in Sect. 4.4, and how these vary by region in Sect. 4.5. We quantify surface $O_3$ biases in the present day and future in Sect. 4.6, and show the importance for assessment of future $O_3$ changes in Sect. 4.7. We present our conclusions in Sect. 4.8.

## 4.2 Approach

### 4.2.1 Chemistry-climate model and experiments

The chemistry-climate model, UKESM1 is used in this chapter. Model description and development are fully introduced in section 1.3. Only necessary information of the model set-up and the model application for this chapter is described below, the same as in section 3.2. We use UKESM1 (Sellar et al., 2019) to simulate present-day (2004–2014) and future (2045–2055) surface $O_3$ concentrations under different emission and climate pathways.

For present day simulations, we use the Coupled-Model Intercomparison Project Phase 6 (CMIP6; Eyring et al., 2016) historical anthropogenic and biomass emissions from Hoesly et al. (2018) and van Marle et al. (2017) respectively. Biogenic VOC emissions are calculated interactively in the Joint UK Land Environmental Simulator (JULES) land-surface scheme (Pacifico et al., 2011) which is coupled to UKCA. For future simulations, we use the shared socio-economic pathways (SSPs; O'Neill et al., 2014) which represent different pathways of emission and climate policies in the future accounting for social, economic and environmental development (Rao et al., 2017). We choose the SSP3-7.0 and SSP3-7.0-lowNTCF pathways to demonstrate the impacts of weak and strong air pollutant emission controls in the future, respectively. Both pathways lead to a warmer and more humid climate, but SSP3-7.0-lowNTCF has large reductions in anthropogenic emissions of near-term climate forcer (NTCF) species that include $O_3$ precursors and aerosols. Details of the present-day and future emissions under SSP3-7.0 and SSP3-7.0-lowNTCF can be found in Liu et al. (2022). Other emissions used here are the same as described in Turnock et al. (2020).

### 4.2.2 Deep artificial neural network

We develop a deep learning model using a multilayer perceptron as it is a fundamental approach to build artificial neural networks and easy to apply. More complex approaches such as convolutional or attention-based neural networks could be applied (LeCun et al., 2015; Vaswani et al., 2017), but multilayer perceptron neural networks are competitive and show good performance compared with other approaches (Tolstikhin et al., 2021). We hence choose a classic artificial neural network as an initial step to explore the possibility of $O_3$ bias correction; more complex approaches could be explored in future.

The multilayer perceptron neural network consists of an input layer, several hidden layers and an output layer, shown in Fig. 4.1. In the hidden layers, we use three independent modules – a densely-connected layer, a batch-normalisation layer (Ioffe and Szegedy, 2015) and a rectified linear unit (Relu; Glorot et al., 2011). Each layer has neurons that store data and associated weights. Neurons in densely connected layers connect to each neuron in the following layer. The batch-normalisation layers make the model training faster and more stable. The rectified linear unit is a non-linear activation function applied to the output of the previous layer. The deep learning model developed here is applied to correct surface $O_3$ mixing ratios solely simulated by UKESM1.

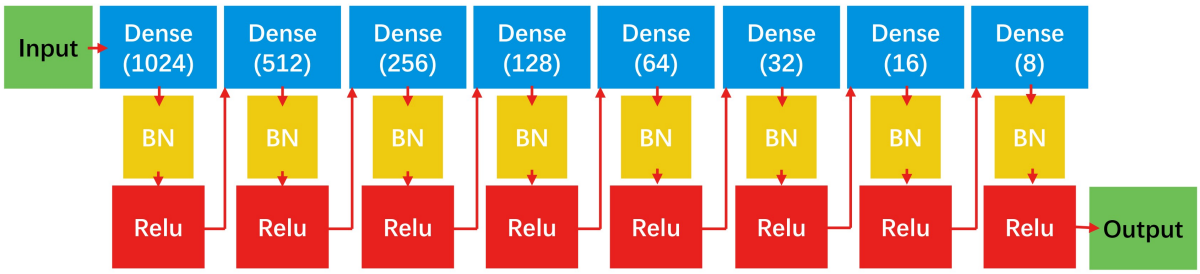


**Figure 4.1:** The structure of the deep artificial neural network built in this study. Each box represents one layer with neurons and weights to be passed to the next layer. In the densely-connected layer ('Dense') all neurons connect with neurons in the next layer, and the number of neurons is shown in brackets. In the batch-normalisation layer ('BN') the data is normalised and passed to the next layer. The rectified linear unit ('Relu') acts as a non-linear activation function. The arrows show the computation path from input to output.

### 4.2.3 Deep learning model application

Previous studies have shown that there are systematic seasonal biases in surface $O_3$ mixing ratios simulated with many chemistry-climate models (Young et al., 2018a), including UKESM1 (Turnock et al., 2020). We compare present-day UKESM1 results with monthly mean surface $O_3$ reanalysis data from the European Centre for Medium-Range Weather Forecasts (ECMWF) Atmospheric Composition Reanalysis 4 (EAC4) under the Copernicus Atmosphere Monitoring Service (CAMS; Inness et al., 2019). These reanalysis data are generated from chemical assimilation of observations into a chemical transport model, and we choose to use these rather than sparse observations directly as they provide global coverage, which is important for training the deep learning model. The CAMS $O_3$ reanalysis data have been shown to be generally in good agreement with Tropospheric Ozone Assessment Report (TOAR) observations for North America, Europe and parts of Asia where available, although CAMS surface $O_3$ concentrations show some positive biases, particularly in East and Southeast Asia (Huijnen et al., 2020).

We find that the mean surface $O_3$ mixing ratios over 2004-2014 simulated by UKESM1 are underestimated in the Northern Hemisphere in winter (December, January, February) and overestimated across most continental areas in summer (June, July, August), as shown in Fig. 4.2. Surface $O_3$ mixing ratios are overestimated by 4 ppb on an annual mean basis and the biases show a strong seasonal variation in the Northern Hemisphere. The deep learning model is trained to reproduce these biases so that the original UKESM1 $O_3$ mixing ratios can be corrected to match the observation-based reanalysis.

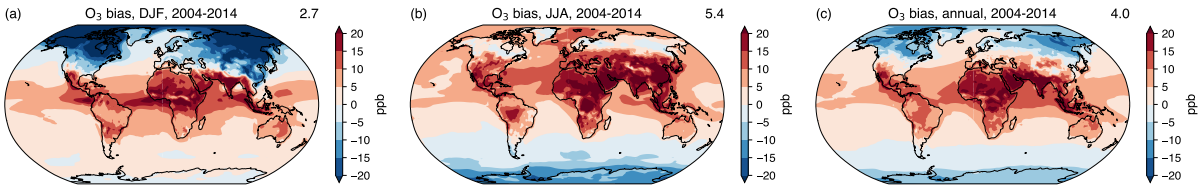


**Figure 4.2:** Seasonal mean biases in surface $O_3$ mixing ratios simulated with UKESM1 compared with CAMS reanalysis data (UKESM1 minus CAMS) in **(a)** December-January-February (DJF) and **(b)** June-July-August (JJA), and **(c)** annual mean biases, all averaged over 2004–2014. Global area-weighted average surface $O_3$ mixing ratio biases (ppb) are shown in the top right of each panel.

### 4.2.4 Deep learning model input

Earth system models have numerous variables influencing surface $O_3$ mixing ratios, but including all variables as inputs for the deep learning model is impractical due to the heavy computation burden. It may also lead to overfitting, a common issue in machine learning associated with including more variables than can be justified by the limited volume of training data. Limiting the number of variables used as inputs also makes the results easier to interpret. In this exploratory study, we investigated more than 30 key input variables that represent the major large-scale influences on $O_3$ chemistry and transport, and settled on 20 variables that show the strongest relationships.

We consider major geographical and temporal variables including latitude, longitude, elevation, land cover and month. We define latitude from the equator to the pole, and month from midwinter to midsummer in each hemisphere. Meteorological variables such as temperature, pressure, humidity, zonal and

meridional wind are considered as they strongly influence $O_3$ chemical formation and transport. The sensitivity of $O_3$ to temperature is of particular interest, and has been shown to be a substantial source of uncertainty in current studies (Archibald et al., 2020c). Temperature and humidity have also been shown to influence $O_3$ variability on both regional and synoptic scales (Han et al., 2020; Shi et al., 2020). Two fundamental photolysis rates j($NO_2$) and jO($^1$D) governing $O_3$ production and destruction are considered. Photolysis rates are strongly dependent on clouds, but there are large uncertainties in simulated cloud cover in current models (Wu et al., 2007; Voulgarakis et al., 2009; Hall et al., 2018). $O_3$ deposition rates and boundary layer height (BLH) are considered as they influence $O_3$ concentrations near the surface (O'Connor et al., 2014; Clifton et al., 2020). Concentrations of $O_3$ precursors such as nitric oxide (NO), VOCs (primary VOC species) and biogenic isoprene are considered, as these govern $O_3$ chemical production. The concentrations of hydroxyl radical (OH) and the oxidative nitrogen species such as nitric acid ($HNO_3$) and peroxyacyl nitrates (PAN) are also considered because they reflect the general oxidation capacity of the atmosphere. $HNO_3$ and PAN are important nitrogen sinks that may transport nitrogen and affect $O_3$ formation over a wide area. Between them, the 20 variables selected represent some of the key drivers of uncertainty in simulating surface $O_3$, although we note that they are not independent of each other and that other factors may also be important under some conditions. We use $O_3$ mixing ratios from the lowest model layer of UKESM1 and normalise values of each input variable from zero to one.

### 4.2.5 Model training

The deep learning model is trained to reproduce the $O_3$ bias in each UKESM1 grid cell based on the corresponding values of the input variables. We train the deep learning model using the biases of monthly mean surface $O_3$ mixing ratios from each model grid cell over 2004–2014 (192 longitudes $\times$ 144 latitudes $\times$ 12 months $\times$ 11 years = 3.6 million data samples). We randomly split the data into training data (80 %), validation data (10 %) and testing data (10 %). Training data are only used to train the model. The validation data provide an evaluation of model performance for each iteration of training, and the testing data are used to provide an independent evaluation once model training is complete.

The performance of the deep learning model is dependent on the volume of data and the settings used, and we experiment with a range of different settings to keep a balance between training speed and accuracy. We choose an Adam optimiser for the training algorithm (Kingma and Ba, 2014), and use mean absolute error for the loss function in this study. We use 0.01 as the model learning rate, and 1024 grid boxes as the training batch size for stochastic gradient descent. Among these settings, we find that the batch size is the most important factor influencing the model performance. 1024 randomly sampled data points account for about 4 % of the data from all grid cells in one month in each training iteration, and we find that this is adequate to represent different situations of $O_3$ biases and is found to be sufficient to train the model well.

## 4.3 Deep learning model performance

We determine the deep learning model performance in predicting surface $O_3$ biases using the testing data to give an independent evaluation (Fig. 4.3). The model reproduces the surface $O_3$ biases well with a high correlation coefficient of 0.99 and with a mean bias error of 0.1 ppb and root-mean-square error of 1.9 ppb. The frequency distribution of surface $O_3$ biases predicted by the deep learning model is very similar to that calculated using the $O_3$ reanalysis data. The tails of the distribution also match well, indicating that large biases can be reproduced well. The evaluation demonstrates that the input variables selected are sufficient to predict surface $O_3$ biases well.

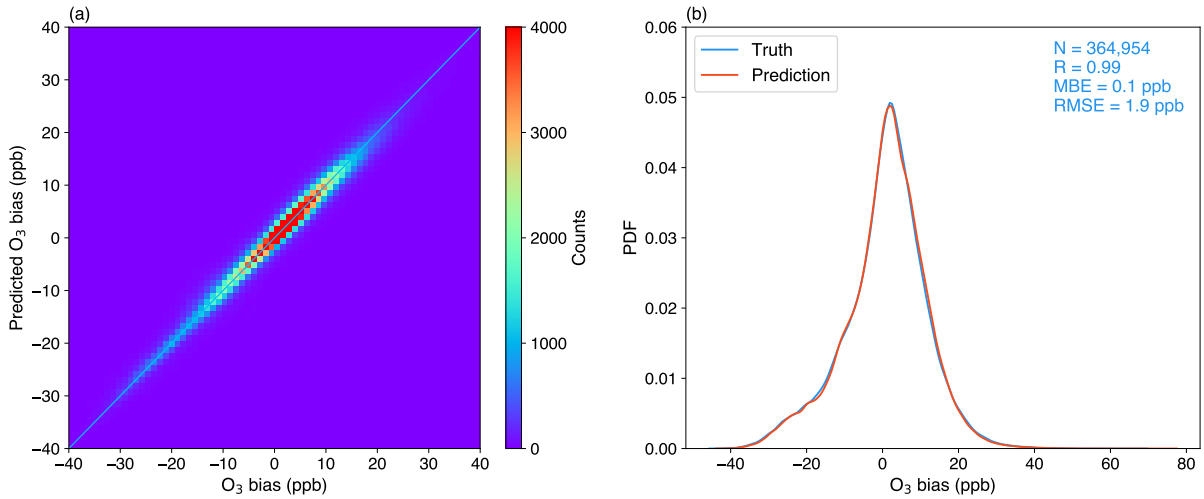


**Figure 4.3:** Evaluation of the deep learning model in simulating monthly mean surface $O_3$ biases at each UKESM1 grid point based on testing data. **(a)** $O_3$ biases (UKESM1 minus CAMS) and biases predicted by the deep learning model. **(b)** Probability density function of $O_3$ biases (labelled here as Truth) and predicted $O_3$ biases. Statistics are shown in the top right corner.

To investigate the spatial and temporal behaviour of the model performance, we focus on surface $O_3$ biases in the present-day high-emission regions of North America, Europe, East Asia and South Asia (Fig. 4.4). North America, Europe and East Asia all show systematic negative surface $O_3$ biases in winter and positive biases in summer (Fig. 4.4a–c). South Asia shows different behaviour, with consistent positive biases for all months (Fig. 4.4d). $O_3$ biases in South Asia show more fluctuations over the annual cycle than those in other regions, but these fluctuations are also captured well by the deep learning model. We note that the magnitudes of $O_3$ biases are simulated well, and that the differences from year to year are also captured accurately. These four regions demonstrate that the deep learning model is able to predict regional differences and their respective magnitudes well.

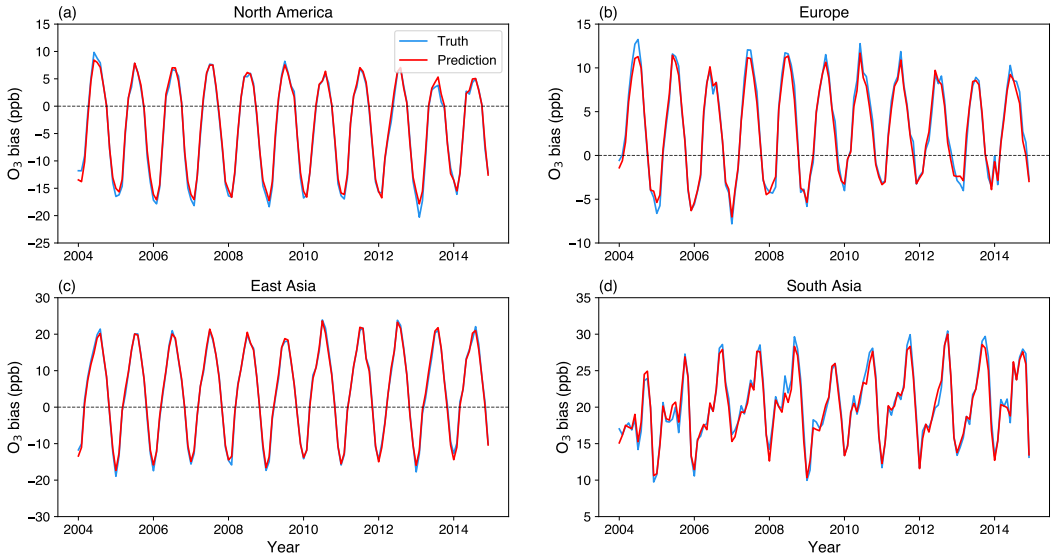


**Figure 4.4:** Monthly mean surface $O_3$ biases (UKESM1 minus CAMS; Truth) and $O_3$ biases predicted by the deep learning model in **(a)** North America, **(b)** Europe, **(c)** East Asia and **(d)** South Asia from January, 2004 to December, 2014.

## 4.4 Feature importance

While all input variables contribute to the prediction of $O_3$ biases, their relative contributions are different and can be estimated to determine which ones are dominant. An advanced unified framework for interpreting predictions of machine learning models, Shapley additive explanations (SHAP; Lundberg and Lee, 2017) is used to calculate the contribution of different variables to the predicted biases. The feature importance is represented by the SHAP value, which provides a quantitative measure of the variable contribution, shown in Fig. 4.5. We calculate SHAP values for each variable using 100 sets of 100 data points randomly selected from the full distribution and show their mean values and one standard deviation. The colours indicate the underlying relationships between the $O_3$ biases and the selected variables based on the correlation between the calculated SHAP values and variable values. Red represents a strong positive relationship ($r > 0.7$), blue represents a strong negative relationship ($r < -0.7$), and green shows weaker relationships.

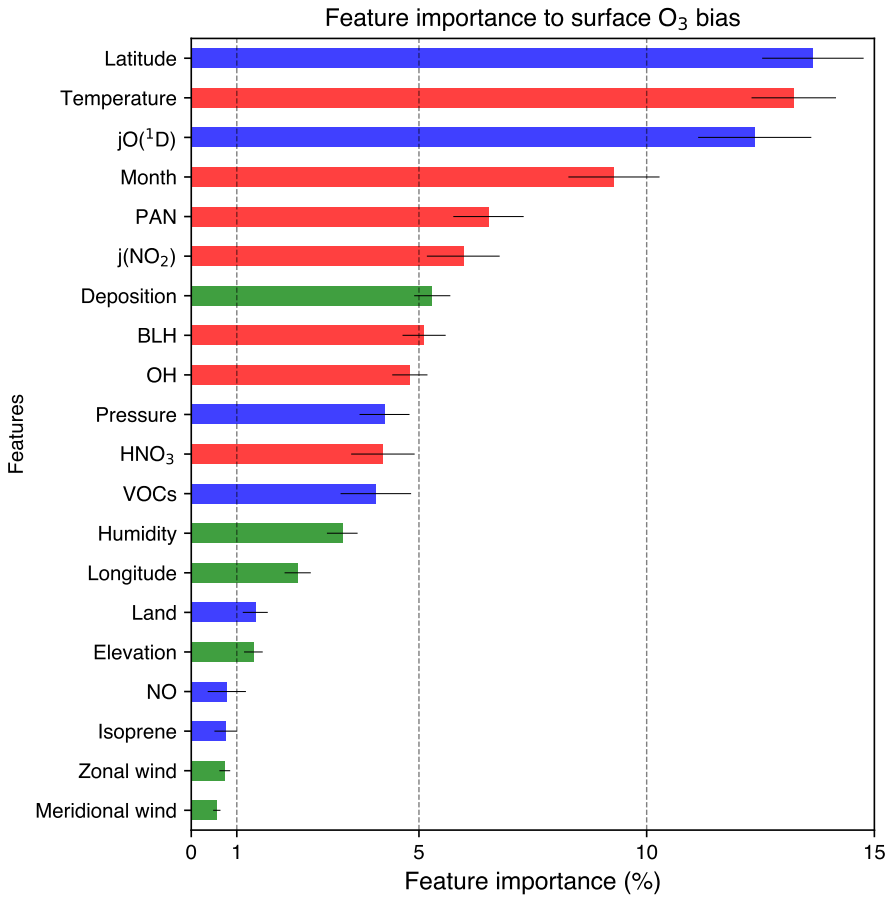


**Figure 4.5:** Importance of different variables to surface $O_3$ biases calculated by the Shapley additive explanations framework (SHAP) for the deep learning model. Strong positive (r > 0.7) and negative (r < -0.7) relationships between $O_3$ biases and variable values are shown in red and blue, respectively, while weaker relationships are shown in green. The error bars show one standard deviation of feature importance for each variable.

We find that latitude and month are important to $O_3$ biases, and show negative and positive relationships to surface $O_3$ biases, respectively. This reflects more positive biases in Tropical regions than at the Poles, and more positive biases in summer than winter. Temperature also shows a strong positive relationship, and this may partly reinforce the influence of latitude and month. Photolysis rates are also important for $O_3$ biases, with $jO(^1D)$ associated with $O_3$ destruction and $j(NO_2)$ with $O_3$ production. The concentrations of PAN, OH and $HNO_3$ all show positive relationships to $O_3$ biases. This may indicate that there are large uncertainties in $O_3$ production under high-oxidation and high-$NO_x$ environments. However, we find that VOCs and short-lived NO concentrations are less important to $O_3$ biases. This highlights the systematic regional and global-scale nature of the $O_3$ biases in UKESM1, and indicates that the biases are not strongly associated with precursor abundance on a regional level. Similarly, isoprene concentrations show little contribution to $O_3$ biases. We note that while $O_3$ deposition rates and BLH are both important to $O_3$ biases, this may partly reflect their similar seasonality. We note that the relationships derived between the variables and $O_3$ biases reflect association, not direct causation.

The relationships between variables with highest feature importance and the $O_3$ biases are generally directly interpretable, demonstrating that the deep learning model may be capturing the internal relationships between inputs and outputs in a physically realistic way. This provides some insight into the sources of $O_3$ biases in UKESM1. We emphasise that the high importance of a variable does not indicate that the variable itself is not simulated well by the chemistry-climate model, or that it is the direct cause of the bias. Since temperature is generally represented well in UKESM1 (Sellar et al., 2019), the importance of temperature thus indicates that $O_3$ biases may be caused

by the representation of physical and chemical processes that are sensitive to temperature changes, such as chemical reaction rates (Coates et al., 2016; Newsome and Evans, 2017), or to other processes for which temperature is a proxy, and this explains the seasonality of the reversal in $O_3$ biases from winter to summer in the Northern hemisphere.

## 4.5 Spatial $O_3$ bias sensitivity

The sensitivity of surface $O_3$ biases to specific variables differs across regions, and we show the spatial sensitivity to variables with high feature importance and strong correlation to $O_3$ biases in Fig. 4.6. Since each variable is considered independent in the deep learning model, we use the change in annual mean $O_3$ bias caused by changes in each variable in each UKESM1 grid cell independently to represent the spatial sensitivity. We perform an experiment for each variable where we increase the value of that variable by a small amount (0.5 standard derivations of its temporal variability over 2004-2014) and calculate the corresponding change in surface $O_3$.

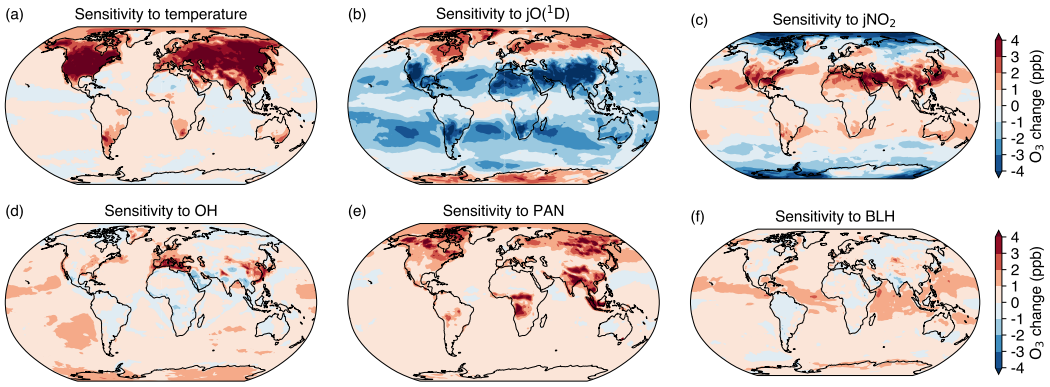


**Figure 4.6:** Sensitivity of annual mean surface $O_3$ bias to increases in **(a)** temperature, **(b)** $jO(^1D)$, **(c)** $j(NO_2)$, **(d)** OH, **(e)** PAN and **(f)** BLH. Variable values are increased by 0.5 standard deviation of their temporal variability for each UKESM1 grid cell independently.

Surface $O_3$ biases are most sensitive to temperature, particularly in continental areas in the Northern hemisphere where higher temperatures are associated with higher $O_3$ (Fig. 4.6a). There is a strong relationship with photolysis rates across a large area, particularly in continental areas at mid and high latitudes (Fig. 4.6b, c), and there is a larger influence from $jO(^1D)$ than from $j(NO_2)$. The chemical environment is important for $O_3$ biases on a regional scale. OH concentrations show a strong association with $O_3$ biases in North America, Europe and East Asia, indicating that high biases in these high-emission regions may be associated with high atmospheric oxidation capacity (Fig. 4.6d). There is also a strong sensitivity to the concentrations of PAN in South Africa, South Asia and South East Asia (Fig. 4.6e). This may indicate uncertainty in the $NO_x$ emission inventory in these regions or the large impacts of nitrogen reservoirs on $O_3$ production. Given the long

lifetime of PAN, it is also associated with $O_3$ biases in remote areas such as the Arctic, indicating that the transport of air pollutants may be important to surface $O_3$ in these areas. BLH is associated with $O_3$ biases in tropical oceanic areas (Fig. 4.6f), and this may reveal the importance of greater $O_3$ mixing and downward transport when the boundary layer is relatively deep.

The spatial sensitivity of surface $O_3$ biases to different variables is helpful to guide future improvement of the UKESM1 model. There are substantial changes in annual mean surface $O_3$ biases associated with adjusting variables values. Increasing temperature, $jO(^1D)$, $j(NO_2)$, OH and PAN concentrations by 0.5 standard deviation changes annual mean surface $O_3$ biases from 4.0 ppb to 4.8 ppb (20 %), 3.0 ppb (-25 %), 4.3 ppb (8 %), 4.5 ppb (13 %) and 4.7 ppb (18 %), respectively. However, we note that UKESM1 generally reproduces temperature and photolysis rates well compared with observations (Telford et al., 2013; Sellar et al., 2019), although there are large differences in simulated concentrations of OH and PAN (O'Connor et al., 2014; Nicely et al., 2020). Our results suggest that chemical processes associated with temperature and oxidation capacity, and cloud and aerosols influencing photolysis rates may be important sources of $O_3$ biases in UKESM1, and that improved representation of these processes may reduce current biases in surface $O_3$.

## 4.6 Assessing biases in modelled future surface $O_3$

We can apply the relationships between variables and surface $O_3$ biases derived from present day simulations to assess the biases in future $O_3$ projections with UKESM1 and to correct our estimates of future $O_3$ concentrations. We demonstrate how surface $O_3$ biases change for two future emission and climate scenarios, SSP3-7.0 and SSP3-7.0-lowNTCF. These pathways are associated with a warmer and more humid climate than the present day. While increased temperature might be expected to increase surface $O_3$ biases, we find that annual mean $O_3$ biases decrease from 4.0 ppb to 3.6 ppb (11 %) under SSP3-7.0 and to 1.3 ppb (67 %) under SSP3-7.0-lowNTCF. This is principally due to the changes in the chemical environment reflected by decreases in the concentrations of OH (-15 % and -13 %) and PAN (-30 % and -38 %) under SSP3-7.0 and SSP3-7.0-lowNTCF, respectively. In continental areas where surface $O_3$ concentrations are overestimated, the UKESM1 model performance is likely to improve under these less polluted future conditions. Since SSP3-7.0-lowNTCF represents a more stringent emission control pathway than SSP3-7.0, there are larger decreases in $O_3$ biases under this scenario.

We investigate the spatial distribution of annual mean changes in surface $O_3$ biases in future scenarios. We find that $O_3$ biases decrease in most oceanic areas under both future scenarios, see Fig. 4.7. However, $O_3$ biases increase in some continental areas especially in the Middle East, South Asia and East Asia under SSP3-7.0. This is due to less stringent emission controls in these regions and hence higher concentrations of $O_3$ precursors and their oxidation products under SSP3-7.0 (Turnock et al., 2020). Under SSP3-

7.0-lowNTCF, there are widespread decreases in $O_3$ biases except over East Asia, where anthropogenic VOC emissions increase substantially and there is a corresponding increase in PAN concentrations and an increase in $O_3$ biases. In high-emission regions, the performance of UKESM1 in future $O_3$ simulations largely depends on changes in $O_3$ precursor emissions given that changes in temperature and photolysis rates are small under future scenarios. The performance of UKESM1 in high-emission regions is expected to improve under scenarios with clean air quality policies, but is likely to become worse under scenarios with increasing future pollutant emissions.

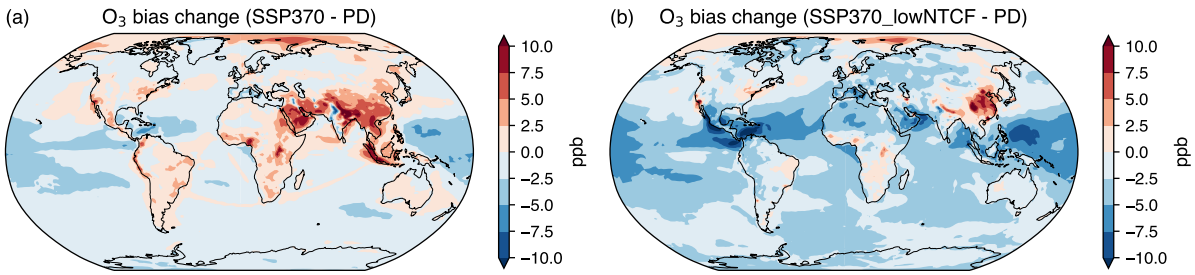


**Figure 4.7:** Annual mean change in surface $O_3$ biases (ppb) between the present day (PD) and 2045-2055 under **(a)** SSP3-7.0 and **(b)** SSP3-7.0-lowNTCF pathways.

## 4.7 Bias correction in future $O_3$ projections

We can provide more reliable projections of future $O_3$ by subtracting the calculated surface $O_3$ biases from surface $O_3$ mixing ratios simulated with UKESM1 under future scenarios (Fig. 4.8). The simulated surface $O_3$ mixing ratios vary in the different scenarios due to different emissions and climate (Fig. 4.8a-c), but the spatial distributions are generally similar, with the highest $O_3$ levels in the Middle East and South Asia. The spatial patterns of

surface $O_3$ biases are also similar under the different scenarios, with biases highest in the Tropics (Fig. 4.8d-f). High $O_3$ mixing ratios in the Middle East and South Asia are reduced greatly after $O_3$ bias correction (Fig. 4.8g-h). There are also large decreases in surface $O_3$ mixing ratios in high-emission regions e.g. North America and East Asia, and continental outflow regions e.g. North Atlantic. The corrected global annual mean surface $O_3$ mixing ratios are lower than those simulated under all scenarios, and are highest under SSP3-7.0 and lowest under SSP3-7.0-lowNTCF, which is consistent with the uncorrected UKESM1 results.

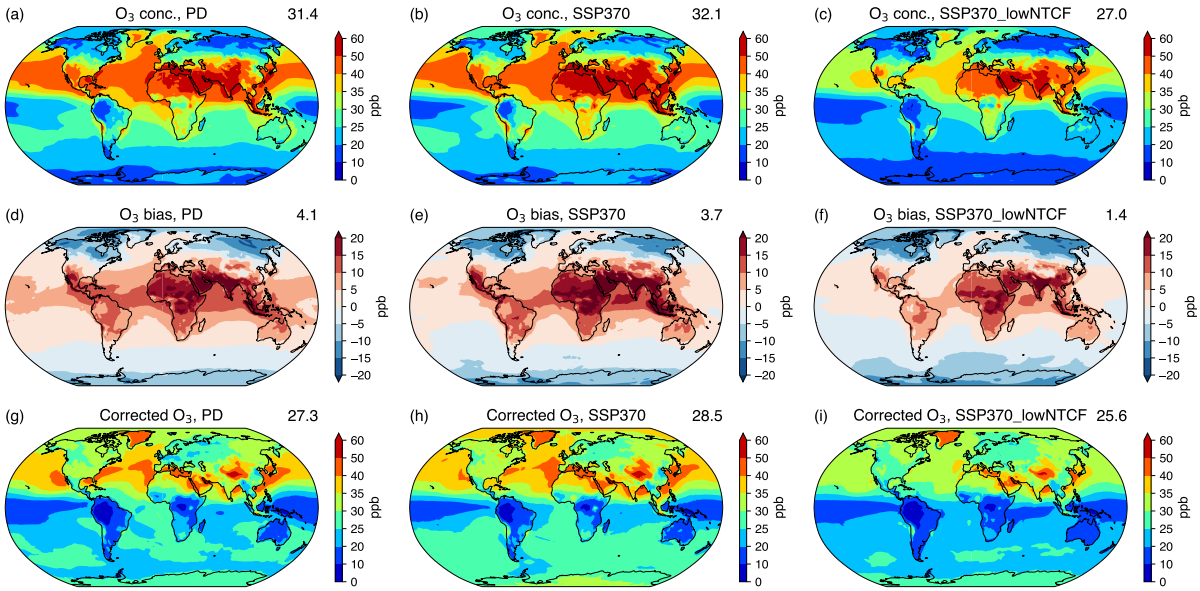


**Figure 4.8:** Annual mean surface $O_3$ mixing ratios (ppb) from UKESM1 simulations for **(a)** the present day (PD), **(b)** SSP3-7.0 and **(c)** SSP3-7.0-lowNTCF. The corresponding surface $O_3$ biases predicted with the deep learning model are shown in **(d-f)** and corrected surface $O_3$ mixing ratios are shown in **(g-h)**. Annual global mean mixing ratios are shown in the top right of each panel.

We show the changes in seasonal mean surface $O_3$ mixing ratios in North America, Europe, South Asia, East Asia and the globe from the present day to the future in Fig. 4.9, comparing the original assessments using UKESM1 with the bias-corrected values. Under SSP3-7.0, the corrected changes in global mean surface $O_3$ are slightly larger than the uncorrected UKESM1 results. However, in high-emissions regions the corrected changes are generally smaller than those originally simulated under both SSP3-7.0 and SSP3-7.0-lowNTCF. In summer, corrected surface $O_3$ mixing ratios increase in all regions considered here under SSP3-7.0, and decrease under SSP3-7.0-lowNTCF. Corrected $O_3$ increases in South and East Asia under SSP3-7.0 are 6-8 ppb smaller than those simulated, and this indicates that $O_3$ air quality degradation due to future emission growth and climate change may not be as severe as the uncorrected UKESM1 simulations suggest. Similarly, under SSP3-7.0-lowNTCF, corrected $O_3$ decreases are smaller in all regions, and this indicates that the impacts of emission controls on $O_3$ mitigation may be smaller than those expected. This can be confirmed by the smaller global mean $O_3$ decreases under SSP3-7.0-lowNTCF in the bias-corrected assessment ($< 2$ ppb) than in the original UKESM1 simulation ($> 3$ ppb). In winter, the corrected changes in surface $O_3$ mixing ratios are smaller than those simulated with UKESM1, whether these changes are positive or negative.

These results highlight that the influence of changing emissions and climate on $O_3$ may not be as large as those simulated with UKESM1 and thus projections of future surface $O_3$ changes may be overestimated. UKESM1 shows a strong seasonality in surface $O_3$ likely due to strong $O_3$ sensitivity to temperature and chemical environment, and this leads to large changes in future $O_3$. UKESM1 typically overestimates future surface $O_3$ changes, and other

chemistry-climate models are likely to display similar behaviour. Therefore, the impacts of changes in emissions and climate on future $O_3$ should be re-assessed in light of the underlying surface $O_3$ biases. We demonstrate the successful application of a deep learning model to address this issue, and it would be valuable to take a similar approach with the output of other chemistry-climate models to provide a more reliable assessment of future surface $O_3$ changes.

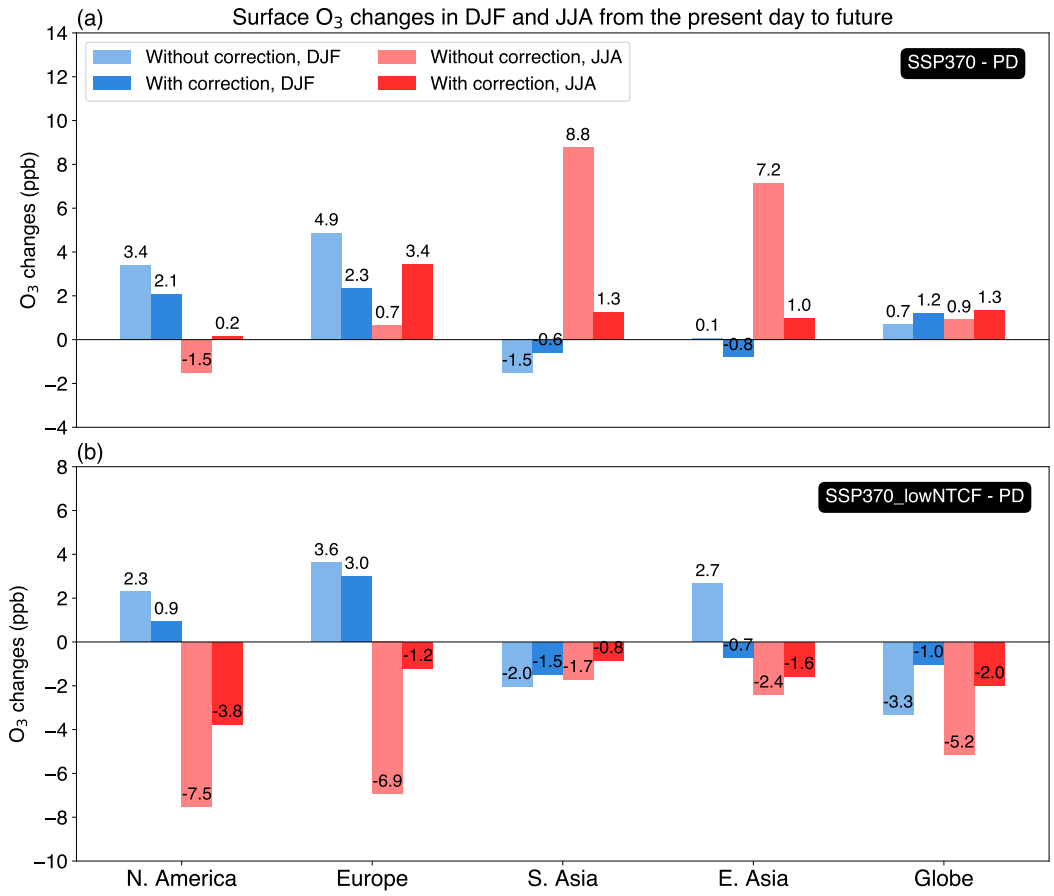


**Figure 4.9:** Changes in seasonal mean surface $O_3$ mixing ratios (ppb) with and without corrections in DJF (blue bars) and JJA (red bars) from the present day (PD) to **(a)** SSP3-7.0 and **(b)** SSP3-7.0-lowNTCF in North America, Europe, South Asia, East Asia and the globe.

## 4.8 Conclusions

There are large uncertainties in the simulation of surface $O_3$ in current chemistry-climate models, but it is difficult to identify the causes of biases and improve representation of the key processes. In this study, we have demonstrated the feasibility of correcting surface $O_3$ biases for a chemistry-climate model, UKESM1, using a machine learning technique. A deep artificial neural network is built with input variables important for $O_3$ chemistry and dynamics. The deep learning model shows good performance in predicting surface $O_3$ biases, with a high correlation coefficient of 0.99 and small mean bias errors of 0.1 ppb. Application of the deep learning model to the results from the process-based UKESM1 model shows promise for predicting future $O_3$ concentrations under different climate and emission trajectories with greater confidence.

This study has also explored the key factors governing $O_3$ biases, which provide valuable insight for model improvement. We find that temperature is an important factor governing $O_3$ biases, especially for continental areas in the Northern hemisphere, indicating that physical and chemical processes influenced by temperature may be not represented well. Photolysis rates also contribute to $O_3$ biases across the globe, indicating that simulated clouds and aerosols may be an important source of $O_3$ biases. Chemical species such as PAN and OH are closely associated with $O_3$ biases on a regional scale, suggesting that weaknesses in representation of key chemical processes remains a substantial issue.

We have applied a deep learning model to generate a correction to the projections of surface $O_3$ mixing ratios for the present day and under future SSP3-7.0 and SSP3-7.0-lowNTCF pathways. We find that global annual

mean $O_3$ biases (4.0 ppb) decrease by 0.4 ppb (11 %) and 2.7 ppb (67 %) under these scenarios, respectively. However, $O_3$ biases in high-emissions areas may increase due to increased $O_3$ precursors. We use this approach to demonstrate that seasonal changes in surface $O_3$ mixing ratios from the present day to the future may be overestimated by as much as 6 ppb with UKESM1, especially in high-emission areas, and this highlights a strong $O_3$ sensitivity to changes in future emissions and climate in the model. A similar overestimation of future $O_3$ changes is likely in other chemistry-climate models, and the influence of emission controls on surface $O_3$ mixing ratios may thus be smaller than suggested by current model simulations. This suggests that emission control policies may be less effective in improving regional air quality than global model simulations indicate.

The deep learning model employed here is a valuable tool to obtain more reliable predictions of the magnitude and spatial distribution of surface $O_3$ mixing ratios. We acknowledge that the choice of input variables is likely to influence the sensitivity of $O_3$ biases derived from the deep learning model, and the relationships between $O_3$ biases and input variables are not always readily interpretable, which is common in machine learning. However, we demonstrate that the relationships between the variables with the highest feature importance and surface $O_3$ biases are intuitive, e.g. with temperature and photolysis rates, and this provides useful insight for further model improvement. The approach applied here provides a valuable opportunity to examine the uncertainties in a chemistry-climate model, and helps improve assessment of the impacts of changing emissions and climate on future air quality.

# Chapter 5

# Conclusions

## 5.1 Overview of thesis

Controlling high surface $O_3$ levels is important for human and ecosystem health. Tropospheric $O_3$ is also important to climate change. By using chemistry-climate models, present-day $O_3$ concentrations can be reproduced to help tackle regional air pollution, such as increasingly severe $O_3$ pollution in industrial regions of China. Future $O_3$ changes can be also quantified to understand the impacts of changing climate and emissions on $O_3$ evolution. Highly $O_3$ polluted regions often occur in high-emission regions, and a more comprehensive chemistry scheme is hence implemented to provide an improved representation of urban and regional $O_3$ production. However, simulated $O_3$ is inherently uncertain because it depends on many chemical and physical processes and their interaction. Due to large uncertainties in such processes and their underlying variables, $O_3$ biases can be corrected with a deep learning model. This approach is also applied to provide a more accurate assessment of $O_3$ responses to changing emissions and climate in

the future.

First, regarding the effectiveness of emission controls in $O_3$ mitigation in industrial regions of China, reductions in $NO_x$ emissions will increase surface $O_3$ concentrations in most high-emission regions of China due to their VOC-limited regimes for $O_3$ production. This also explains the increased surface $O_3$ concentrations in China in recent years despite stringent emission controls. However, reductions in $NO_x$ emissions alone of more than 70 % are required to transform the VOC-limited regimes to $NO_x$-limited regimes for these regions. To address increased $O_3$ concentrations caused by decreased $NO_x$ emissions, reductions in VOC emissions are found to be important because combined $NO_x$ and VOC emission controls can effectively suppress $O_3$ increases.

Subsequently, $O_3$ changes from the present day to the future are investigated for all regions across the globe. The changes in anthropogenic emissions of $O_3$ precursors can largely explain the tropospheric $O_3$ burden changes. However, surface $O_3$ concentrations vary substantially in different regions and seasons, principally due to varying regional $O_3$ sensitivity. VOC-limited regimes are more extensive in winter than in summer across the globe, leading to increased surface $O_3$ concentrations in winter in contrast to decreased $O_3$ concentrations in summer in North America and Europe. In the future, South Asia will become the dominant VOC-limited region, and most areas in North America, Europe and East Asia will become $NO_x$-limited regimes if $NO_x$ emissions decrease.

Lastly, the deep learning model demonstrates the advantages and capabilities of machine learning in correcting surface $O_3$ biases. Temperature, photolysis rates, concentrations of OH, PAN and $HNO_3$ all show strong relationships to $O_3$ biases, which provides some insights for future model development.

Changes in future surface $O_3$ concentrations after $O_3$ bias corrections are found to be smaller than those without corrections, indicating that $O_3$ responses to changing climate and emissions may be stronger simulated with climate-chemistry models than in the real atmosphere, which provides a valuable assessment of future $O_3$ evolution.

## 5.2 Major results of the research

### 5.2.1 Emission control strategies in China

**Aim: To assess the effectiveness of emission control strategies in reducing $O_3$ levels in industrial regions of China.**

The national Air Pollution Prevention and Control Action Plan was released in 2013 as the most influential environmental policy in China. Many pollutants such as $PM_{2.5}$, $NO_x$ and $SO_2$ have been effectively controlled especially in industrial regions due to stringent emission controls. However, increased surface $O_3$ concentrations are observed in these regions in recent years.

The capabilities of an extended chemistry scheme with diurnal and vertical emission profiles are demonstrated when simulating surface $O_3$ concentrations in the industrial regions of China: Beijing and Shijiazhuang on the North China Plain, Shanghai and Nanjing in the Yangtze River Delta, Guangzhou in the Pearl River Delta and Chongqing in the Sichuan Basin. Simulated $O_3$ concentrations are highest in Beijing and Shijiazhuang, lower in Shanghai and Nanjing, and lowest in Guangzhou despite the highest daytime $O_3$ production rates in Guangzhou. $NO_x$/VOC and $H_2O_2$/$HNO_3$ ratios indicate that $O_3$ production across all regions except Chongqing is VOC

limited.

In VOC-limited regions, reducing $NO_x$ emissions by 20 % leads to a substantial $O_3$ increase (11 %) in Shanghai. Reductions in $NO_x$ emissions alone of more than 70 % are required to decrease $O_3$ concentrations across all regions. Reductions in VOC emissions alone of 20 % produce the largest decrease (–11 %) in $O_3$ levels in Shanghai and Guangzhou and the smallest decrease (–1 %) in Chongqing. These responses are substantially different from those currently found in highly populated regions in other parts of the world, likely due to higher $NO_x$ emission levels in these Chinese regions. The work emphasises that combined $NO_x$ and VOC emission controls play a pivotal role in effectively offsetting high $O_3$ levels.

### 5.2.2 Ozone changes across the globe from present-day to future

**Aim: To investigate the evolution of tropospheric $O_3$ from the present day to the future under different emission and climate scenarios.**

Projections of future $O_3$ are influenced by changing emissions and climate, and the evolution of tropospheric $O_3$ is quantified under the shared socioeconomic pathways (SSPs) for emissions and for a warmer climate. The tropospheric $O_3$ burden increases by 4 % under a development pathway with higher $NO_x$ and VOC emissions (SSP3-7.0), but decreases by 7 % under the same pathway if $NO_x$ and VOC emissions are reduced (SSP3-7.0-lowNTCF) and by 5 % if atmospheric $CH_4$ concentrations are reduced (SSP3-7.0-lowCH4). Global mean surface $O_3$ mixing ratios are reduced by 3–5 ppb

under SSP3-7.0-lowNTCF and by 2–3 ppb under SSP3-7.0-lowCH4.

Surface $O_3$ changes vary in different seasons and regions, typically with decreased $O_3$ concentrations in summer and increased $O_3$ concentrations in winter when $NO_x$ emissions are reduced. Monthly mean, daytime mean and nighttime mean $O_3$ changes are substantially different as well, demonstrating the generally stronger daytime $O_3$ responses to emissions in summer.

North America, Europe and East Asia are the dominant VOC-limited regions in the present day but North America and Europe become more $NO_x$-limited in the future mainly due to reductions in $NO_x$ emissions. The impacts of VOC emissions on $O_3$ sensitivity are limited in North America and Europe because reduced anthropogenic VOC emissions are partly offset by higher biogenic VOC emissions. $O_3$ sensitivity is not greatly influenced by changing $CH_4$ concentrations. South Asia becomes the dominant VOC-limited region under these future pathways. The work highlights the importance of reducing VOC and $CH_4$ concentrations to mitigate regional $O_3$ pollution in the future.

### 5.2.3 Surface ozone bias correction

**Aim: To quantify and correct the $O_3$ biases in a chemistry-climate model and to explore the potential reasons causing the model biases.**

Chemistry climate models are imperfect in simulating accurate surface $O_3$ concentrations due to the difficulty in representing all physical and chemical processes in models. Biases in $O_3$ simulations are also associated with uncertainty in emissions and structural errors which arise from coarse model resolutions. Such biases are hard to eliminate. Therefore, a deep learning model

is developed to quantify and correct surface $O_3$ biases using present-day reanalyse data, and to provide more accurate predictions of future $O_3$.

The deep learning model implemented shows capabilities in predicting surface $O_3$ biases in different regions. In addition, it also provides some insights about underlying biased processes in the model. Temperature and the related geographic variables latitude and month show the strongest relationship with $O_3$ biases. This indicates that $O_3$ biases are sensitive to temperature and suggests weakness in the representation of temperature-sensitive physical or chemical processes. Photolysis rates are shown to be important for $O_3$ biases given large uncertainty in simulated cloud cover and insolation in chemistry-climate models. Chemical species such as OH, $HNO_3$ and PAN all show great positive relationships to $O_3$ biases.

Global annual mean $O_3$ biases in both future scenarios (SSP3-7.0 and SSP3-7.0-lowNTCF) are smaller than that in the present day. The corrected seasonal $O_3$ changes in high-emission regions in the future may be not as large as those simulated with UKESM1. This demonstrates that the $O_3$ sensitivity to future emissions and climate in UKESM1 may be stronger than the real atmosphere.

Therefore, the value of deep learning is reflected in providing a more reliable and improved assessment of $O_3$ evolution under different climate emission scenarios in the future, and in the exploration of underlying causes of surface $O_3$ biases in a global chemistry climate model.

## 5.3 Synthesis of research findings

It is the first time that an extended gas-phase chemistry scheme is implemented in UKESM1, with more reactive VOC species to represent a more realistic $O_3$ production environment for high-emission regions. This permits the application of a global chemistry-climate model to investigate current regional $O_3$ pollution issues, as well as regional $O_3$ evolution in the future.

Both Chapter 2 and 3 investigating $O_3$ pollution in China and tropospheric $O_3$ changes in the future respectively, demonstrate the important role of controlling anthropogenic emissions in $O_3$ mitigation. Changes in anthropogenic emissions can largely explain substantial differences between surface $O_3$ changes and surface $PM_{2.5}$ changes in China in recent years. Tropospheric $O_3$ changes from the present day to the future can also largely be explained by anthropogenic emission changes in the context of climate change.

The effectiveness of emission controls will differ by region and even may differ within a region, depending on local chemical environments. In most industrial regions of China where $O_3$ production is VOC-limited, combined $NO_x$ and VOC emission controls are necessary to offset increased $O_3$ concentrations due to decreased $NO_x$ emissions. However, large reductions in $NO_x$ emissions alone of more than 70 % are required to transform their VOC-limited regimes to $NO_x$-limited regimes. Summer daytime $O_3$ responses to changing $NO_x$ emissions in these Chinese regions are substantially different from those in other highly populated regions across the globe, likely due to much higher $NO_x$ emissions in China despite great reductions in recent years.

$O_3$ sensitivity is also explored in Chapter 3 but considering monthly $O_3$ concentrations for present-day and into the future. From a global perspective,

there are relatively few studies characterising surface $O_3$ sensitivity. Thus, a consistent $O_3$ sensitivity indicator approach is applied to investigate regional $O_3$ sensitivity across the globe. Most high-emission regions across the globe are still VOC-limited in winter. However, most areas of North America, Europe and East Asia would become $NO_x$-limited regimes in the future as more $NO_x$ emissions are reduced, in contrast to South Asia that is the dominant VOC-limited region in the future. Reductions in $CH_4$ concentrations are also an effective approach to offset high $O_3$ concentrations. Daytime mean and monthly mean $O_3$ sensitivity is investigated for Chapter 2 and 3 respectively, and the later accounts for nighttime $O_3$ sensitivity that tends to be VOC-limited in high-emission regions due to the accumulation of $NO_x$ in the boundary layer at nighttime. Therefore, monthly mean $O_3$ sensitivity in some regions of North America and Europe in summer are VOC-limited, but their daytime $O_3$ sensitivity may differ, suggesting that emission control strategies may be required to target different i.e. daytime or monthly mean $O_3$ metrics.

Accurate projections of future $O_3$ are constrained to uncertainty from different sources in models. Deep learning models provide opportunities to explore underlying reasons causing $O_3$ biases, and to correct future $O_3$ projections. The deep learning results shows that temperature, photolysis rates, OH and oxidative nitrogen species (i.e. PAN and $HNO_3$) are the most important variables to $O_3$ biases. Biases are associated with temperature, reflected by positive biases in summer but negative biases in winter, and much higher $O_3$ biases in tropical regions, as shown in Chapter 3. The impacts of photolysis rates and OH on $O_3$ biases are also reflected in Chapter 2, for the Chongqing region in which surface $O_3$ concentrations are largely overestimated. The chemical environment in Chongqing is different from other industrial regions

of China, reflected by its highest photolysis rates and concentrations of OH, which strongly suggests the $O_3$ overestimation may be caused by these factors. However, these factors could also be influenced by coarse model grid cells, and the impacts of model resolution is discussed in Chapter 2. PAN and $HNO_3$ are also important variables worthy being evaluated along with $O_3$ evaluations as they may give some insights to understand the complex impacts of nitrogen species on $O_3$. After $O_3$ bias corrections, future surface $O_3$ shows weaker responses to changing climate and emissions than those in UKESM1 simulations, highlighting that the impacts of climate and emissions on $O_3$ may be overestimated by UKESM1.

Overall, reductions in anthropogenic emissions help reduce the tropospheric $O_3$ burden but regional surface $O_3$ sensitivity should be paid attention to because there are still many regions that are located in VOC-limited regimes. Changes in anthropogenic emissions are a dominant factor controlling tropospheric $O_3$ for present-day $O_3$ pollution issues and for future $O_3$ evolution in the context of climate change. However, the findings of $O_3$ bias corrections leading to lower future $O_3$ suggests that the impacts of climate and emission changes on surface $O_3$ may be overestimated by chemistry climate models, or at least in UKESM1, due to these different uncertain sources.

## 5.4 Limitations

While UKESM1 is a state-of-the-art global chemistry climate model, there is still uncertainty in tropospheric $O_3$ simulations. Firstly, apart from internal errors in the model itself, such as uncertainties in the comprehensive representation of physical and chemical processes, there is external uncertainty that mainly lies in emissions. The impacts of increased anthropogenic emis-

sions have been studied well, principally leading to the degradation of air quality and to climate change due to long-lived chemical species. Emissions are hence the important inputs of models. The deep learning results also demonstrate that surface $O_3$ sensitivity to emissions and climate is larger in UKESM1 than in the real atmosphere, as shown in Chapter 4. The Multi-resolution Emission Inventory for China (MEIC) is used to provide emissions over China in Chapter 2. This is a regional emission inventory but the available latest version was only for the year of 2013. The approach adopted in Chapter 2 is to adjust emissions to the year of 2016 according to emission scaling factors in China from 2013 to 2016, to fit rapid changes in emissions in recent years in China. Since the present-day (2004-2014) $O_3$ is examined across the globe in Chapter 3 and 4, a global emission inventory is used, obtained from the Community Emissions Data System (CEDS). However, Archibald et al. (2020a) shows large differences between regional and global emission inventories especially in China. Therefore, the problem exists of updating emission inventories to reflect rapid real world changes but this is required for an improved assessment of the effectiveness of emission control strategies.

Secondly, UKESM1 is a global model with coarse model resolution, leading to structural errors in $O_3$ simulations, which is a common issue in climate chemistry models (Young et al., 2018b). Surface $O_3$ concentrations are typically higher in a coarse model grid box than in a fine grid box especially in polluted areas (Wild and Prather, 2006). The dilution of $O_3$ precursors in a coarse model grid box not only influences $O_3$ concentrations, but also $O_3$ sensitivity. $NO_x$ is very reactive so can be rapidly consumed when confined locally but the dilution of $NO_x$ in a regional scale may lead to an inaccurate simulation of the regional $O_3$ production regime i.e. VOC-limited when in

reality is $NO_x$-limited.

Thirdly, some studies show that interactions between aerosols and gas-phase chemistry are important, although these studies mainly focus on specific regions and cases, and are not comprehensive from a global perspective. Heterogeneous uptake of radicals (Li et al., 2019a) and $HNO_3$ (Akimoto et al., 2019) on aerosol surfaces is shown to reduce $O_3$ concentrations, even though Tan et al. (2020) argues that there are no significant impacts of radical uptake on decreases in $O_3$ concentrations. High aerosol concentrations will also influence $O_3$ formation through altering the photolysis rates (Hollaway et al., 2019; Qu et al., 2021). Clearly, more measurement data and process-based studies are needed to confirm the importance of aerosols to $O_3$ formation. In the current UKESM1 version, there are few reactions accounting for heterogeneous processes and no coupling between the interactive aerosol scheme and the gas-phase chemistry scheme. The inclusion of these reactions may reduce surface $O_3$ concentrations, leading to decreases in $O_3$ biases and more accurate model performance, especially in polluted regions that may have relatively large impacts of heterogeneous reactions due to high aerosol concentrations.

Lastly, a simple artificial neural network has been built to correct surface $O_3$ biases for each individual UKESM1 grid cell. However, a limitation is that $O_3$ biases caused by transport cannot be captured by the deep learning model, even though the current deep learning model has shown good performance. The inclusion of transport process in the deep learning model may help distinguish local and transport impacts to provide a clear interpretation of results. In addition, a limited number of input variables are chosen to feed into the deep learning model to avoid overfitting the targeted $O_3$ biases. The sensitivity of predicted $O_3$ biases may vary with different input

variables, influencing the conclusion of the key process causing $O_3$ biases. Therefore, more sensitivity tests are needed to enhance the robustness of the interpretation of deep learning model results.

## 5.5 Future work

Future developments for chemistry-climate modelling at the community level should involve the development of emission inventories, higher resolution modelling, the development of comprehensive chemistry schemes that can be optimally included in a chemistry-climate model. Despite development needed, there is still some interesting work that can be performed in relation to the combination between deep learning models and atmospheric models to resolve complex but practical problems.

In Chapter 4, surface reanalysis data sets are used to train the deep learning model because they assimilate observed data and modelled data to provide relatively 'correct' surface $O_3$ concentrations. This fits supervised learning because pre-labelled outputs are known. Supervised learning provides great opportunities to obtain more accurate spatial distributions and magnitudes of surface $O_3$ concentrations in the future through $O_3$ bias corrections, according to the relationships learned from historical data. While this helps reassess the impacts of changing climate and emissions on future $O_3$, no information can be gained about what the most optimal approach is to reduce $O_3$ pollution. Chemistry-climate models provide tools to quantify the effectiveness of emission controls, but actions in reality are constrained by many social factors accounting for economic costs and practical difficulties when implementing emission controls in different sectors. Human health and crop yields are positive aspects of air quality improvement but emission controls

are still not of a high priority if local air quality is relatively good compared with surrounding regions. This indicates that the relationships between these factors and air quality are not linear. Therefore, improving air quality is a complex problem with multi-dimensions in benefits and drawbacks of emission controls, and the key is to resolve how to maximise the improvement of air quality and its related benefits, and to minimise the adverse impacts of emission controls. The multi-dimensions of this problem not only reflect in local effects, but also in global effects because local air pollution can be influenced by other regions over a large scale. The balance between these aspects hence represents the most optimal emission control strategies.

This complicated problem may be potentially resolved by reinforcement learning, another class of machine learning, as introduced in section 1.4.1. The changes in air pollutants due to emissions can be calculated by chemistry-climate models, and they provide the approximate directions of emission controls. If relationships between different social factors and emission controls are known, optimal emission control strategies can be calculated by reinforcement learning models. It will be interesting to see a broad picture of emission control strategies in different regions across the globe with the maximum social and environmental benefits.

# Bibliography

Agathokleous, E., Feng, Z., Oksanen, E., Sicard, P., Wang, Q., Saitanis, C. J., Araminiene, V., Blande, J. D., Hayes, F., Calatayud, V., et al.: Ozone affects plant, insect, and soil microbial communities: A threat to terrestrial ecosystems and biodiversity, Science advances, https://doi.org/10.1126/sciadv.abc1176, 2020.

Akimoto, H., Nagashima, T., Li, J., Fu, J. S., Ji, D., Tan, J., and Wang, Z.: Comparison of surface ozone simulation among selected regional models in MICS-Asia III–effects of chemistry and vertical transport for the causes of difference, Atmospheric Chemistry and Physics, 19, 603–615, https://doi.org/10.5194/acp-19-603-2019, 2019.

Allen, R. J., Horowitz, L. W., Naik, V., Oshima, N., O'Connor, F. M., Turnock, S., Shim, S., Le Sager, P., van Noije, T., Tsigaridis, K., Bauer, S. E., Sentman, L. T., John, J. G., Broderick, C., Deushi, M., Folberth, G. A., Fujimori, S., and Collins, W. J.: Significant climate benefits from near-term climate forcer mitigation in spite of aerosol reductions, Environmental Research Letters, 16, https://doi.org/10.1088/1748-9326/abe06b, 2021.

Alléon, A., Jauvion, G., Quennehen, B., and Lissmyr, D.: PlumeNet: Large-

scale air quality forecasting using a convolutional LSTM network, arXiv preprint arXiv:2006.09204, https://arxiv.org/abs/2006.09204, 2020.

André, J., De Moor, G., Lacarrere, P., and Du Vachat, R.: Modeling the 24-hour evolution of the mean and turbulent structures of the planetary boundary layer, Journal of Atmospheric Sciences, 35, 1861–1883, https://doi.org/10.1175/1520-0469(1978)035⟨1861:MTHEOT⟩2.0.CO;2, 1978.

Archer-Nicholls, S., Abraham, N. L., Shin, Y. M., Weber, J., Russo, M. R., Lowe, D., Utembe, S., O'Connor, F. M., Kerridge, B., Latter, B., et al.: The Common Representative Intermediates Mechanism version 2 in the United Kingdom Chemistry and Aerosols Model, Journal of Advances in Modeling Earth Systems, https://doi.org/10.1029/2020MS002420, 2020.

Archibald, A., Neu, J., Elshorbany, Y., Cooper, O., Young, P., Akiyoshi, H., Cox, R., Coyle, M., Derwent, R., Deushi, M., et al.: Tropospheric Ozone Assessment ReportA critical review of changes in the tropospheric ozone burden and budget from 1850 to 2100, Elementa: Science of the Anthropocene, 8, https://doi.org/10.1525/elementa.2020.034, 2020a.

Archibald, A. T., O'Connor, F. M., Abraham, N. L., Archer-Nicholls, S., Chipperfield, M. P., Dalvi, M., Folberth, G. A., Dennison, F., Dhomse, S. S., Griffiths, P. T., et al.: Description and evaluation of the UKCA stratosphere–troposphere chemistry scheme (StratTrop vn 1.0) implemented in UKESM1, Geoscientific Model Development, 13, 1223–1266, https://doi.org/10.5194/gmd-13-1223-2020, 2020b.

Archibald, A. T., Turnock, S. T., Griffiths, P. T., Cox, T., Derwent, R. G., Knote, C., and Shin, M.: On the changes in surface ozone over the twenty-first century: sensitivity to changes in surface temperature and chemi-

cal mechanisms, Philosophical Transactions of the Royal Society A, 378, 20190 329, https://doi.org/10.1098/rsta.2019.0329, 2020c.

Atkinson, R., Baulch, D., Cox, R., Crowley, J., Hampson, R., Hynes, R., Jenkin, M., Rossi, M., Troe, J., and Subcommittee, I.: Evaluated kinetic and photochemical data for atmospheric chemistry: Volume II–gas phase reactions of organic species, Atmospheric chemistry and physics, 6, 3625–4055, https://doi.org/10.5194/acp-6-3625-2006, 2006.

Ayzel, G., Scheffer, T., and Heistermann, M.: RainNet v1. 0: a convolutional neural network for radar-based precipitation nowcasting, Geoscientific Model Development, 13, 2631–2644, https://doi.org/10.5194/gmd-13-2631-2020, 2020.

Berner, C., Brockman, G., Chan, B., Cheung, V., Debiak, P., Dennison, C., Farhi, D., Fischer, Q., Hashme, S., Hesse, C., et al.: Dota 2 with large scale deep reinforcement learning, arXiv preprint, https://arxiv.org/abs/1912.06680v1, 2019.

Bieser, J., Aulinger, A., Matthias, V., Quante, M., and Van Der Gon, H. D.: Vertical emission profiles for Europe based on plume rise calculations, Environmental Pollution, 159, 2935–2946, https://doi.org/10.1016/j.envpol.2011.04.030, 2011.

Biggart, M., Stocker, J., Doherty, R. M., Wild, O., Hollaway, M., Carruthers, D., Li, J., Zhang, Q., Wu, R., Kotthaus, S., et al.: Street-scale air quality modelling for Beijing during a winter 2016 measurement campaign, Atmospheric Chemistry and Physics, 20, 2755–2780, https://doi.org/10.5194/acp-20-2755-2020, 2020.

Cardelino, C. and Chameides, W.: An observation-based model for analyzing

ozone precursor relationships in the urban atmosphere, Journal of the Air & Waste Management Association, 45, 161–180, https://doi.org/10.1080/10473289.1995.10467356, 1995.

Carter, W. P. and Atkinson, R.: Computer modeling study of incremental hydrocarbon reactivity, Environmental science & technology, 23, 864–880, https://doi.org/10.1021/es00065a017, 1989.

Chameides, W. and Walker, J. C.: A photochemical theory of tropospheric ozone, Journal of Geophysical Research, 78, 8751–8760, https://doi.org/10.1029/JC078i036p08751, 1973.

Chameides, W., Lindsay, R., Richardson, J., and Kiang, C.: The role of biogenic hydrocarbons in urban photochemical smog: Atlanta as a case study, Science, 241, 1473–1475, https://doi.org/10.1126/science.3420404, 1988.

Cheng, J., Su, J., Cui, T., Li, X., Dong, X., Sun, F., Yang, Y., Tong, D., Zheng, Y., Li, Y., et al.: Dominant role of emission reduction in PM 2.5 air quality improvement in Beijing during 2013–2017: a model-based decomposition analysis, Atmospheric Chemistry and Physics, 19, 6125–6146, https://doi.org/10.5194/acp-19-6125-2019, 2019.

Clifton, O. E., Fiore, A. M., Massman, W. J., Baublitz, C. B., Coyle, M., Emberson, L., Fares, S., Farmer, D. K., Gentine, P., Gerosa, G., et al.: Dry deposition of ozone over land: processes, measurement, and modeling, Reviews of Geophysics, 58, e2019RG000 670, https://doi.org/10.1029/2019RG000670, 2020.

Coates, J., Mar, K. A., Ojha, N., and Butler, T. M.: The influence of temperature on ozone production under varying NO x conditions–a

modelling study, Atmospheric Chemistry and Physics, 16, 11 601–11 615, https://doi.org/10.5194/acp-16-11601-2016, 2016.

Colette, A., Aas, W., Banin, L., Braban, C. F., Ferm, M., Gonzalez Ortiz, A., Ilyin, I., Mar, K., Pandolfi, M., Putaud, J.-P., et al.: Air pollution trends in the EMEP region between 1990 and 2012, EMEP Co-operative Programme for Monitoring and Evaluation of the Long-range Transmission of Air Pollutants in Europe, https://unece.org/environment-policy/publications/air-pollution-trends-emep-region-between-1990-and-2012, 2016.

Collins, W. J., Lamarque, J. F., Schulz, M., Boucher, O., Eyring, V., Hegglin, M. I., Maycock, A., Myhre, G., Prather, M., Shindell, D., and Smith, S. J.: AerChemMIP: quantifying the effects of chemistry and aerosols in CMIP6, Geoscientific Model Development, 10, 585–607, https://doi.org/10.5194/gmd-10-585-2017, 2017.

Cooper, O. R., Parrish, D., Ziemke, J., Balashov, N., Cupeiro, M., Galbally, I., Gilge, S., Horowitz, L., Jensen, N., Lamarque, J.-F., et al.: Global distribution and trends of tropospheric ozone: An observation-based review-Global distribution and trends of tropospheric ozone, Elementa: Science of the Anthropocene, 2, https://doi.org/10.12952/journal.elementa.000029, 2014.

Council, N. R.: Rethinking the ozone problem in urban and regional air pollution, National Academies Press, https://doi.org/10.17226/1889, 1992.

Crutzen, P. J.: Photochemical reactions initiated by and influencing ozone in unpolluted tropospheric air, Tellus, 26, 47–57, https://doi.org/10.3402/tellusa.v26i1-2.9736, 1974.

Dee, D. P., Uppala, S. M., Simmons, A., Berrisford, P., Poli, P., Kobayashi,

S., Andrae, U., Balmaseda, M., Balsamo, G., Bauer, d. P., et al.: The ERA-Interim reanalysis: Configuration and performance of the data assimilation system, Quarterly Journal of the royal meteorological society, 137, 553–597, https://doi.org/10.1002/qj.828, 2011.

Doherty, R. M., Wild, O., Shindell, D. T., Zeng, G., MacKenzie, I. A., Collins, W. J., Fiore, A. M., Stevenson, D. S., Dentener, F. J., Schultz, M. G., Hess, P., Derwent, R. G., and Keating, T. J.: Impacts of climate change on surface ozone and intercontinental ozone pollution: A multi-model study, Journal of Geophysical Research-Atmospheres, 118, 3744–3763, https://doi.org/10.1002/jgrd.50266, 2013.

Doherty, R. M., Orbe, C., Zeng, G., Plummer, D. A., Prather, M. J., Wild, O., Lin, M., Shindell, D. T., and Mackenzie, I. A.: Multi-model impacts of climate change on pollution transport from global emission source regions, Atmospheric Chemistry and Physics, 17, 14 219–14 237, https://doi.org/10.5194/acp-17-14219-2017, 2017.

Dunker, A. M., Yarwood, G., Ortmann, J. P., and Wilson, G. M.: Comparison of source apportionment and source sensitivity of ozone in a three-dimensional air quality model, Environmental science & technology, 36, 2953–2964, https://doi.org/10.1021/es011418f, 2002.

Ehhalt, D., Prather, M., Dentener, F., Derwent, R., Dlugokencky, E. J., Holland, E., Isaksen, I., Katima, J., Kirchhoff, V., Matson, P., et al.: Atmospheric chemistry and greenhouse gases, Tech. rep., Pacific Northwest National Lab (PNNL), https://www.ipcc.ch/report/ar3/wg1/chapter-4-atmospheric-chemistry-and-greenhouse-gases/, 2001.

El Hihi, S. and Bengio, Y.: Hierarchical recurrent neural networks for long-term dependencies, in: Advances in neural information process-

ing systems, pp. 493–499, https://proceedings.neurips.cc/paper/1995/file/c667d53acd899a97a85de0c201ba99be-Paper.pdf, 1996.

Emberson, L.: Effects of ozone on agriculture, forests and grasslands, Philosophical Transactions of the Royal Society A, 378, 20190 327, https://doi.org/10.1098/rsta.2019.0327, 2020.

Eyring, V., Bony, S., Meehl, G. A., Senior, C. A., Stevens, B., Stouffer, R. J., and Taylor, K. E.: Overview of the Coupled Model Intercomparison Project Phase 6 (CMIP6) experimental design and organization, Geoscientific Model Development, 9, 1937–1958, https://doi.org/10.5194/gmd-9-1937-2016, 2016.

Fenech, S., Doherty, R. M., Heaviside, C., Vardoulakis, S., Macintyre, H. L., and O'Connor, F. M.: The influence of model spatial resolution on simulated ozone and fine particulate matter for Europe: implications for health impact assessments, Atmospheric Chemistry and Physics, 18, 5765–5784, https://doi.org/10.5194/acp-18-5765-2018, 2018.

Feng, L. Y., Smith, S. J., Braun, C., Crippa, M., Gidden, M. J., Hoesly, R., Klimont, Z., van Marle, M., van den Berg, M., and van der Werf, G. R.: The generation of gridded emissions data for CMIP6, Geoscientific Model Development, 13, 461–482, https://doi.org/10.5194/gmd-13-461-2020, 2020.

Fiore, A. M., West, J. J., Horowitz, L. W., Naik, V., and Schwarzkopf, M. D.: Characterizing the tropospheric ozone response to methane emission controls and the benefits to climate and air quality, Journal of Geophysical Research-Atmospheres, 113, https://doi.org/10.1029/2007JD009162, 2008.

Fiore, A. M., Naik, V., Spracklen, D. V., Steiner, A., Unger, N., Prather, M., Bergmann, D., Cameron-Smith, P. J., Cionni, I., Collins, W. J., Dalsøren, S., Eyring, V., Folberth, G. A., Ginoux, P., Horowitz, L. W., Josse, B., Lamarque, J.-F., MacKenzie, I. A., Nagashima, T., O'Connor, F. M., Righi, M., Rumbold, S. T., Shindell, D. T., Skeie, R. B., Sudo, K., Szopa, S., Takemura, T., and Zeng, G.: Global air quality and climate, Chemical Society Reviews, 41, 6663–6683, https://doi.org/10.1039/c2cs35095e, 2012.

Fiore, A. M., Naik, V., and Leibensperger, E. M.: Air quality and climate connections, Journal of the Air & Waste Management Association, 65, 645–685, https://doi.org/10.1080/10962247.2015.1040526, 2015.

Fischer, E., Jacob, D. J., Yantosca, R. M., Sulprizio, M. P., Millet, D., Mao, J., Paulot, F., Singh, H., Roiger, A., Ries, L., et al.: Atmospheric peroxyacetyl nitrate (PAN): a global budget and source attribution, Atmospheric Chemistry and Physics, 14, 2679–2698, https://doi.org/10.5194/acp-14-2679-2014, 2014.

Fishman, J. and Crutzen, P. J.: The origin of ozone in the troposphere, Nature, 274, 855–858, https://doi.org/10.1038/274855a0, 1978.

Flato, G. M.: Earth system models: an overview, Wiley Interdisciplinary Reviews: Climate Change, 2, 783–800, https://doi.org/10.1002/wcc.148, 2011.

Fleming, Z. L., Doherty, R. M., Von Schneidemesser, E., Malley, C. S., Cooper, O. R., Pinto, J. P., Colette, A., Xu, X., Simpson, D., Schultz, M. G., et al.: Tropospheric Ozone Assessment Report: Present-day ozone distribution and trends relevant to human health, Elementa: Science of the Anthropocene, 6, https://doi.org/10.1525/elementa.273, 2018.

Folberth, G. A., Hauglustaine, D., Lathière, J., and Brocheton, F.: Interactive chemistry in the Laboratoire de Météorologie Dynamique general circulation model: model description and impact analysis of biogenic hydrocarbons on tropospheric chemistry, Atmospheric Chemistry and Physics, 6, 2273–2319, https://doi.org/10.5194/acp-6-2273-2006, 2006.

Fujimori, S., Hasegawa, T., Masui, T., Takahashi, K., Herran, D. S., Dai, H. C., Hijioka, Y., and Kainuma, M.: SSP3: AIM implementation of Shared Socioeconomic Pathways, Global Environmental Change-Human and Policy Dimensions, 42, 268–283, https://doi.org/10.1016/j.gloenvcha.2016.06.009, 2017.

Fuks, K. B., Hüls, A., Sugiri, D., Altug, H., Vierkötter, A., Abramson, M. J., Goebel, J., Wagner, G. G., Demuth, I., Krutmann, J., et al.: Tropospheric ozone and skin aging: Results from two German cohort studies, Environment international, 124, 139–144, https://doi.org/10.1016/j.envint.2018.12.047, 2019.

Gao, M., Gao, J., Zhu, B., Kumar, R., Lu, X., Song, S., Zhang, Y., Jia, B., Wang, P., Beig, G., Hu, J., Ying, Q., Zhang, H., Sherman, P., and McElroy, M. B.: Ozone pollution over China and India: seasonality and sources, Atmospheric Chemistry and Physics, 20, 4399–4414, https://doi.org/10.5194/acp-20-4399-2020, 2020.

Gaudel, A., Cooper, O., Ancellet, G., Barret, B., Boynard, A., Burrows, J., Clerbaux, C., Coheur, P.-F., Cuesta, J., Cuevas, E., et al.: Tropospheric Ozone Assessment Report: Present-day distribution and trends of tropospheric ozone relevant to climate and global atmospheric chemistry model evaluation, Elementa: Science of the Anthropocene, 6, https://doi.org/10.1525/elementa.291, 2018.

Glorot, X., Bordes, A., and Bengio, Y.: Deep sparse rectifier neural networks, in: Proceedings of the fourteenth international conference on artificial intelligence and statistics, pp. 315–323, JMLR Workshop and Conference Proceedings, http://proceedings.mlr.press/v15/glorot11a/glorot11a.pdf, 2011.

Gong, C. and Liao, H.: A typical weather pattern for ozone pollution events in North China, Atmospheric Chemistry and Physics, 19, 13 725–13 740, https://doi.org/10.5194/acp-19-13725-2019, 2019.

Goodfellow, I., Bengio, Y., and Courville, A.: Deep learning, MIT press, http://www.deeplearningbook.org, 2016.

Griffiths, P. T., Murray, L. T., Zeng, G., Shin, Y. M., Abraham, N. L., Archibald, A. T., Deushi, M., Emmons, L. K., Galbally, I. E., Hassler, B., et al.: Tropospheric ozone in CMIP6 simulations, Atmospheric Chemistry and Physics, 21, 4187–4218, https://doi.org/10.5194/acp-21-4187-2021, 2021.

Grulke, N. E. and Heath, R.: Ozone effects on plants in natural ecosystems, Plant Biology, 22, 12–37, https://doi.org/10.1111/plb.12971, 2020.

Hakim, Z. Q., Archer-Nicholls, S., Beig, G., Folberth, G. A., Sudo, K., Abraham, N. L., Ghude, S., Henze, D. K., and Archibald, A. T.: Evaluation of tropospheric ozone and ozone precursors in simulations from the HTAPII and CCMI model intercomparisons–a focus on the Indian subcontinent, Atmospheric Chemistry and Physics, 19, 6437–6458, https://doi.org/10.5194/acp-19-6437-2019, 2019.

Hall, S. R., Ullmann, K., Prather, M. J., Flynn, C. M., Murray, L. T., Fiore, A. M., Correa, G., Strode, S. A., Steenrod, S. D., Lamarque,

J.-F., et al.: Cloud impacts on photochemistry: building a climatology of photolysis rates from the Atmospheric Tomography mission, Atmospheric Chemistry and Physics, 18, 16 809–16 828, https://doi.org/10.5194/acp-18-16809-2018, 2018.

Han, H., Liu, J., Shu, L., Wang, T., and Yuan, H.: Local and synoptic meteorological influences on daily variability in summertime surface ozone in eastern China, Atmospheric Chemistry and Physics, 20, 203–222, https://doi.org/10.5194/acp-20-203-2020, 2020.

Han, J., Jentzen, A., and Weinan, E.: Solving high-dimensional partial differential equations using deep learning, Proceedings of the National Academy of Sciences, 115, 8505–8510, https://doi.org/10.1073/pnas.1718942115, 2018.

Hinton, G., Deng, L., Yu, D., Dahl, G. E., Mohamed, A.-r., Jaitly, N., Senior, A., Vanhoucke, V., Nguyen, P., Sainath, T. N., et al.: Deep neural networks for acoustic modeling in speech recognition: The shared views of four research groups, IEEE Signal processing magazine, 29, 82–97, https://doi.org/10.1109/MSP.2012.2205597, 2012.

Hochreiter, S. and Schmidhuber, J.: Long short-term memory, Neural computation, 9, 1735–1780, https://doi.org/10.1162/neco.1997.9.8.1735, 1997.

Hodnebrog, Ø., Stordal, F., and Berntsen, T. K.: Does the resolution of megacity emissions impact large scale ozone?, Atmospheric environment, 45, 6852–6862, https://doi.org/10.1016/j.atmosenv.2011.01.012, 2011.

Hoesly, R. M., Smith, S. J., Feng, L., Klimont, Z., Janssens-Maenhout, G., Pitkanen, T., Seibert, J. J., Vu, L., Andres, R. J., Bolt, R. M., et al.: Historical (1750–2014) anthropogenic emissions of reactive gases

and aerosols from the Community Emissions Data System (CEDS), Geoscientific Model Development, 11, 369–408, https://doi.org/10.5194/gmd-11-369-2018, 2018.

Hollaway, M., Wild, O., Yang, T., Sun, Y., Xu, W., Xie, C., Whalley, L., Slater, E., Heard, D., and Liu, D.: Photochemical impacts of haze pollution in an urban environment, Atmospheric Chemistry and Physics, 19, 9699–9714, https://doi.org/10.5194/acp-19-9699-2019, 2019.

Horowitz, L. W., Liang, J., Gardner, G. M., and Jacob, D. J.: Export of reactive nitrogen from North America during summertime: Sensitivity to hydrocarbon chemistry, Journal of Geophysical Research: Atmospheres, 103, 13 451–13 476, https://doi.org/10.1029/97JD03142, 1998.

Huang, G., Brook, R., Crippa, M., Janssens-Maenhout, G., Schieberle, C., Dore, C., Guizzardi, D., Muntean, M., Schaaf, E., and Friedrich, R.: Speciation of anthropogenic emissions of non-methane volatile organic compounds: a global gridded data set for 1970–2012, Atmospheric Chemistry and Physics, 17, 7683–7701, https://doi.org/10.5194/acp-17-7683-2017, 2017.

Huijnen, V., Miyazaki, K., Flemming, J., Inness, A., Sekiya, T., and Schultz, M. G.: An intercomparison of tropospheric ozone reanalysis products from CAMS, CAMS interim, TCR-1, and TCR-2, Geoscientific model development, 13, 1513–1544, https://doi.org/10.5194/gmd-13-1513-2020, 2020.

Inness, A., Ades, M., Agusti-Panareda, A., Barré, J., Benedictow, A., Blechschmidt, A.-M., Dominguez, J. J., Engelen, R., Eskes, H., Flemming, J., et al.: The CAMS reanalysis of atmospheric composition, Atmospheric Chemistry and Physics, 19, 3515–3556, https://doi.org/10.5194/acp-19-3515-2019, 2019.

Ioffe, S. and Szegedy, C.: Batch normalization: Accelerating deep network training by reducing internal covariate shift, in: International conference on machine learning, pp. 448–456, PMLR, https://arxiv.org/abs/1502.03167, 2015.

IPCC: 2021: Climate Change 2021: The Physical Science Basis. Contribution of Working Group I to the Sixth Assessment Report of the Intergovernmental Panel on Climate Change, IPCC, https://www.ipcc.ch/report/sixth-assessment-report-working-group-i/, 2021.

Ivatt, P. D. and Evans, M. J.: Improving the prediction of an atmospheric chemistry transport model using gradient-boosted regression trees, Atmospheric Chemistry and Physics, 20, 8063–8082, https://doi.org/10.5194/acp-20-8063-2020, 2020.

Janssens-Maenhout, G., Crippa, M., Guizzardi, D., Dentener, F., Muntean, M., Pouliot, G., Keating, T., Zhang, Q., Kurokawa, J., Wankmüller, R., et al.: HTAP_v2. 2: a mosaic of regional and global emission grid maps for 2008 and 2010 to study hemispheric transport of air pollution, Atmospheric Chemistry and Physics, 15, 11 411–11 432, https://doi.org/10.5194/acp-15-11411-2015, 2015.

Jin, X. and Holloway, T.: Spatial and temporal variability of ozone sensitivity over China observed from the Ozone Monitoring Instrument, Journal of Geophysical Research: Atmospheres, 120, 7229–7246, https://doi.org/10.1002/2015JD023250, 2015.

Keller, C. A. and Evans, M. J.: Application of random forest regression to the calculation of gas-phase chemistry within the GEOS-Chem chemistry model v10, Geoscientific Model Development, 12, 1209–1225, https://doi.org/10.5194/gmd-12-1209-2019, 2019.

Keller, C. A., Evans, M. J., Knowland, K. E., Hasenkopf, C. A., Modekurty, S., Lucchesi, R. A., Oda, T., Franca, B. B., Mandarino, F. C., Díaz Suárez, M. V., et al.: Global impact of COVID-19 restrictions on the surface concentrations of nitrogen dioxide and ozone, Atmospheric Chemistry and Physics, 21, 3555–3592, https://doi.org/10.5194/acp-21-3555-2021, 2021.

Kingma, D. P. and Ba, J.: Adam: A method for stochastic optimization, arXiv preprint arXiv:1412.6980, https://arxiv.org/abs/1412.6980, 2014.

Kleinert, F., Leufen, L. H., and Schultz, M. G.: IntelliO3-ts v1. 0: a neural network approach to predict near-surface ozone concentrations in Germany, Geoscientific Model Development, 14, 1–25, https://doi.org/10.5194/gmd-14-1-2021, 2021.

Kleinman, L. I.: Low and high NOx tropospheric photochemistry, Journal of Geophysical Research: Atmospheres, 99, 16 831–16 838, https://doi.org/10.1029/94JD01028, 1994.

Kleinman, L. I., Daum, P. H., Lee, J. H., Lee, Y.-N., Nunnermacker, L. J., Springston, S. R., Newman, L., Weinstein-Lloyd, J., and Sillman, S.: Dependence of ozone production on NO and hydrocarbons in the troposphere, Geophysical Research Letters, 24, 2299–2302, https://doi.org/10.1029/97GL02279, 1997.

Kleinman, L. I., Daum, P. H., Lee, Y.-N., Nunnermacker, L. J., Springston, S. R., Weinstein-Lloyd, J., and Rudolph, J.: Sensitivity of ozone production rate to ozone precursors, Geophysical Research Letters, 28, 2903–2906, https://doi.org/10.1029/2000GL012597, 2001.

Kleinman, L. I., Daum, P. H., Lee, Y.-N., Nunnermacker, L. J., Springston, S. R., Weinstein-Lloyd, J., and Rudolph, J.: Ozone production efficiency

in an urban area, Journal of Geophysical Research: Atmospheres, 107, ACH–23, https://doi.org/10.1029/2002JD002529, 2002.

Kleinman, L. I., Daum, P. H., Lee, Y.-N., Nunnermacker, L. J., Springston, S. R., Weinstein-Lloyd, J., and Rudolph, J.: A comparative study of ozone production in five US metropolitan areas, Journal of Geophysical Research: Atmospheres, 110, https://doi.org/10.1029/97GL02279, 2005.

Knutti, R. and Sedláček, J.: Robustness and uncertainties in the new CMIP5 climate model projections, Nature climate change, 3, 369–373, https://doi.org/10.1038/nclimate1716, 2013.

Kober, J., Bagnell, J. A., and Peters, J.: Reinforcement learning in robotics: A survey, The International Journal of Robotics Research, 32, 1238–1274, https://doi.org/10.1177/0278364913495721, 2013.

Krizhevsky, A., Sutskever, I., and Hinton, G. E.: Imagenet classification with deep convolutional neural networks, Advances in neural information processing systems, 25, 1097–1105, https://doi.org/10.1145/3065386, 2012.

Kuhlbrodt, T., Jones, C. G., Sellar, A., Storkey, D., Blockley, E., Stringer, M., Hill, R., Graham, T., Ridley, J., Blaker, A., et al.: The low-resolution version of HadGEM3 GC3. 1: Development and evaluation for global climate, Journal of Advances in Modeling Earth Systems, 10, 2865–2888, https://doi.org/10.1029/2018MS001370, 2018.

Lamarque, J.-F., Bond, T. C., Eyring, V., Granier, C., Heil, A., Klimont, Z., Lee, D., Liousse, C., Mieville, A., Owen, B., et al.: Historical (1850–2000) gridded anthropogenic and biomass burning emissions of reactive gases and aerosols: methodology and application, Atmospheric Chemistry and Physics, 10, 7017–7039, https://doi.org/10.5194/acp-10-7017-2010, 2010.

LeCun, Y., Boser, B., Denker, J., Henderson, D., Howard, R., Hubbard, W., and Jackel, L.: Handwritten digit recognition with a back-propagation network, Advances in neural information processing systems, 2, 396–404, https://proceedings.neurips.cc/paper/1989/file/53c3bce66e43be4f209556518c2fcb54-Paper.pdf, 1989.

LeCun, Y., Bengio, Y., and Hinton, G.: Deep learning, nature, 521, 436–444, https://doi.org/10.1038/nature14539, 2015.

Lefohn, A. S., Shadwick, D., and Oltmans, S. J.: Characterizing long-term changes in surface ozone levels in the United States (1980-2005), Atmospheric Environment, 42, 8252–8262, https://doi.org/10.1016/j.atmosenv.2008.07.060, 2008.

Lefohn, A. S., Malley, C. S., Smith, L., Wells, B., Hazucha, M., Simon, H., Naik, V., Mills, G., Schultz, M. G., Paoletti, E., et al.: Tropospheric ozone assessment report: Global ozone metrics for climate change, human health, and crop/ecosystem research, Elementa: Science of the Anthropocene, 6, https://doi.org/10.1525/elementa.279, 2018.

Lelieveld, J. and Dentener, F. J.: What controls tropospheric ozone?, JGR: Atmospheres, 105, 3531–3551, https://doi.org/10.1029/1999JD901011, 2000.

Lelieveld, J., Evans, J. S., Fnais, M., Giannadaki, D., and Pozzer, A.: The contribution of outdoor air pollution sources to premature mortality on a global scale, Nature, 525, 367–371, https://doi.org/10.1038/nature15371, 2015.

Levelt, P. F., Joiner, J., Tamminen, J., Veefkind, J. P., Bhartia, P. K., Stein Zweers, D. C., Duncan, B. N., Streets, D. G., Eskes, H., McLinden,

C., et al.: The Ozone Monitoring Instrument: overview of 14 years in space, Atmospheric Chemistry and Physics, 18, 5699–5745, https://doi.org/10.5194/acp-18-5699-2018, 2018.

Li, K., Jacob, D. J., Liao, H., Shen, L., Zhang, Q., and Bates, K. H.: Anthropogenic drivers of 2013–2017 trends in summer surface ozone in China, Proceedings of the National Academy of Sciences, 116, 422–427, https://doi.org/10.1073/pnas.1812168116, 2019a.

Li, K., Jacob, D. J., Liao, H., Zhu, J., Shah, V., Shen, L., Bates, K. H., Zhang, Q., and Zhai, S.: A two-pollutant strategy for improving ozone and particulate air quality in China, Nature Geoscience, 12, 906–910, https://doi.org/10.1038/s41561-019-0464-x, 2019b.

Li, K., Jacob, D. J., Shen, L., Lu, X., De Smedt, I., and Liao, H.: Increases in surface ozone pollution in China from 2013 to 2019: anthropogenic and meteorological influences, Atmospheric Chemistry and Physics, 20, 11 423–11 433, https://doi.org/10.5194/acp-20-11423-2020, 2020.

Li, L., Chen, Y., and Xie, S.: Spatio-temporal variation of biogenic volatile organic compounds emissions in China, Environmental pollution, 182, 157–168, https://doi.org/10.1016/j.envpol.2013.06.042, 2013.

Li, M., Zhang, Q., Kurokawa, J.-i., Woo, J.-H., He, K., Lu, Z., Ohara, T., Song, Y., Streets, D. G., Carmichael, G. R., et al.: MIX: a mosaic Asian anthropogenic emission inventory under the international collaboration framework of the MICS-Asia and HTAP, Atmospheric Chemistry and Physics, 17, 935–963, https://doi.org/10.5194/acp-17-935-2017, 2017.

Li, S., Wang, T., Huang, X., Pu, X., Li, M., Chen, P., Yang, X.-Q., and Wang, M.: Impact of East Asian summer monsoon on surface ozone pat-

tern in China, Journal of Geophysical Research: Atmospheres, 123, 1401–1411, https://doi.org/10.1002/2017JD027190, 2018.

Liao, H., Chen, W.-T., and Seinfeld, J. H.: Role of climate change in global predictions of future tropospheric ozone and aerosols, Journal of Geophysical Research: Atmospheres, 111, https://doi.org/10.1029/2005JD006852, 2006.

Lim, C. C., Hayes, R. B., Ahn, J., Shao, Y., Silverman, D. T., Jones, R. R., Garcia, C., Bell, M. L., and Thurston, G. D.: Long-term exposure to ozone and cause-specific mortality risk in the United States, American journal of respiratory and critical care medicine, 200, 1022–1031, https://doi.org/10.1164/rccm.201806-1161OC, 2019.

Lin, M., Fiore, A. M., Horowitz, L. W., Langford, A. O., Oltmans, S. J., Tarasick, D., and Rieder, H. E.: Climate variability modulates western US ozone air quality in spring via deep stratospheric intrusions, Nature communications, 6, 1–11, https://doi.org/10.1038/ncomms8105, 2015.

Lin, M., Horowitz, L. W., Xie, Y., Paulot, F., Malyshev, S., Shevliakova, E., Finco, A., Gerosa, G., Kubistin, D., and Pilegaard, K.: Vegetation feedbacks during drought exacerbate ozone air pollution extremes in Europe, Nature Climate Change, 10, 444–451, https://doi.org/10.1038/s41558-020-0743-y, 2020.

Lin, X., Trainer, M., and Liu, S.: On the nonlinearity of the tropospheric ozone production, Journal of Geophysical Research: Atmospheres, 93, 15 879–15 888, https://doi.org/10.1029/JD093iD12p15879, 1988.

Liu, G., Liu, J., Tarasick, D., Fioletov, V., Jin, J., Moeini, O., Liu, X., Sioris, C., and Osman, M.: A global tropospheric ozone climatology from

trajectory-mapped ozone soundings, Atmospheric Chemistry and Physics, 13, 10 659–10 675, https://doi.org/10.5194/acp-13-10659-2013, 2013.

Liu, H., ZHANG, M., and HAN, X.: A review of surface ozone source apportionment in China, Atmospheric and Oceanic Science Letters, 13, 470–484, https://doi.org/10.1080/16742834.2020.1768025, 2020.

Liu, S., Trainer, M., Fehsenfeld, F., Parrish, D., Williams, E., Fahey, D. W., Hübler, G., and Murphy, P. C.: Ozone production in the rural troposphere and the implications for regional and global ozone distributions, Journal of Geophysical Research: Atmospheres, 92, 4191–4207, https://doi.org/10.1029/JD092iD04p04191, 1987.

Liu, X.-H., Zhang, Y., Xing, J., Zhang, Q., Wang, K., Streets, D. G., Jang, C., Wang, W.-X., and Hao, J.-M.: Understanding of regional air pollution over China using CMAQ, part II. Process analysis and sensitivity of ozone and particulate matter to precursor emissions, Atmospheric Environment, 44, 3719–3727, https://doi.org/10.1016/j.atmosenv.2010.03.036, 2010.

Liu, Y. and Wang, T.: Worsening urban ozone pollution in China from 2013 to 2017–Part 1: The complex and varying roles of meteorology, Atmospheric Chemistry and Physics, 20, 6305–6321, https://doi.org/10.5194/acp-20-6305-2020, 2020.

Liu, Z., Doherty, R. M., Wild, O., Hollaway, M., and O'Connor, F. M.: Contrasting chemical environments in summertime for atmospheric ozone across major Chinese industrial regions: the effectiveness of emission control strategies, Atmospheric Chemistry and Physics, 21, 10 689–10 706, https://doi.org/10.5194/acp-21-10689-2021, 2021.

Liu, Z., Doherty, R. M., Wild, O., O'Connor, F. M., and Turnock, S. T.: Tro-

pospheric ozone changes and ozone sensitivity from the present day to the future under shared socio-economic pathways, Atmospheric Chemistry and Physics, 22, 1209–1227, https://doi.org/10.5194/acp-22-1209-2022, 2022.

Lowe, D., Archer-Nicholls, S., Morgan, W., Allan, J., Utembe, S., Ouyang, B., Aruffo, E., Le Breton, M., Zaveri, R. A., Di Carlo, P., et al.: WRF-Chem model predictions of the regional impacts of N 2 O 5 heterogeneous processes on night-time chemistry over north-western Europe, Atmospheric Chemistry and Physics, 15, 1385–1409, https://doi.org/10.5194/acp-15-1385-2015, 2015.

Lu, X., Hong, J., Zhang, L., Cooper, O. R., Schultz, M. G., Xu, X., Wang, T., Gao, M., Zhao, Y., and Zhang, Y.: Severe surface ozone pollution in China: a global perspective, Environmental Science & Technology Letters, 5, 487–494, https://doi.org/10.1021/acs.estlett.8b00366, 2018a.

Lu, X., Zhang, L., Liu, X., Gao, M., Zhao, Y., and Shao, J.: Lower tropospheric ozone over India and its linkage to the South Asian monsoon, Atmospheric Chemistry and Physics, 18, 3101–3118, https://doi.org/10.5194/acp-18-3101-2018, 2018b.

Lu, X., Zhang, L., Chen, Y., Zhou, M., Zheng, B., Li, K., Liu, Y., Lin, J., Fu, T.-M., and Zhang, Q.: Exploring 2016–2017 surface ozone pollution over China: source contributions and meteorological influences, Atmospheric Chemistry and Physics, 19, 8339–8361, https://doi.org/10.5194/acp-19-8339-2019, 2019.

Lu, X., Zhang, L., Wang, X., Gao, M., Li, K., Zhang, Y., Yue, X., and Zhang, Y.: Rapid increases in warm-season surface ozone and resulting health impact in China since 2013, Environmental Science & Technology Letters, 7, 240–247, https://doi.org/10.1021/acs.estlett.0c00171, 2020.

Lundberg, S. M. and Lee, S.-I.: A unified approach to interpreting model predictions, in: Proceedings of the 31st international conference on neural information processing systems, pp. 4768–4777, https://arxiv.org/abs/1705.07874, 2017.

Ma, M., Gao, Y., Wang, Y., Zhang, S., Leung, L. R., Liu, C., Wang, S., Zhao, B., Chang, X., Su, H., et al.: Substantial ozone enhancement over the North China Plain from increased biogenic emissions due to heat waves and land cover in summer 2017, Atmospheric Chemistry and Physics, 19, 12 195–12 207, https://doi.org/10.5194/acp-19-12195-2019, 2019.

Mailler, S., Khvorostyanov, D., and Menut, L.: Impact of the vertical emission profiles on background gas-phase pollution simulated from the EMEP emissions over Europe, Atmospheric Chemistry and Physics, 13, 5987–5998, https://doi.org/10.5194/acp-13-5987-2013, 2013.

Mann, G., Carslaw, K., Spracklen, D., Ridley, D., Manktelow, P., Chipperfield, M., Pickering, S., and Johnson, C.: Description and evaluation of GLOMAP-mode: A modal global aerosol microphysics model for the UKCA composition-climate model, Geoscientific Model Development, 3, 519–551, https://doi.org/10.5194/gmd-3-519-2010, 2010.

Meinshausen, M., Vogel, E., Nauels, A., Lorbacher, K., Meinshausen, N., Etheridge, D. M., Fraser, P. J., Montzka, S. A., Rayner, P. J., Trudinger, C. M., Krummel, P. B., Beyerle, U., Canadell, J. G., Daniel, J. S., Enting, I. G., Law, R. M., Lunder, C. R., O'Doherty, S., Prinn, R. G., Reimann, S., Rubino, M., Velders, G. J. M., Vollmer, M. K., Wang, R. H. J., and Weiss, R.: Historical greenhouse gas concentrations for climate modelling (CMIP6), Geoscientific Model Development, 10, 2057–2116, https://doi.org/10.5194/gmd-10-2057-2017, 2017.

Meinshausen, M., Nicholls, Z. R. J., Lewis, J., Gidden, M. J., Vogel, E., Freund, M., Beyerle, U., Gessner, C., Nauels, A., Bauer, N., Canadell, J. G., Daniel, J. S., John, A., Krummel, P. B., Luderer, G., Meinshausen, N., Montzka, S. A., Rayner, P. J., Reimann, S., Smith, S. J., van den Berg, M., Velders, G. J. M., Vollmer, M. K., and Wang, R. H. J.: The shared socio-economic pathway (SSP) greenhouse gas concentrations and their extensions to 2500, Geoscientific Model Development, 13, 3571–3605, https://doi.org/10.5194/gmd-13-3571-2020, 2020.

Mertens, M., Kerkweg, A., Grewe, V., Jöckel, P., and Sausen, R.: Are contributions of emissions to ozone a matter of scale?–a study using MECO (n)(MESSy v2. 50), Geoscientific Model Development, 13, 363–383, https://doi.org/10.5194/gmd-13-363-2020, 2020.

Mills, G., Wagg, S., and Harmens, H.: Ozone pollution: impacts on ecosystem services and biodiversity, NERC/Centre for Ecology & Hydrology, http://nora.nerc.ac.uk/id/eprint/502675/, 2013.

Monks, P. S., Archibald, A., Colette, A., Cooper, O., Coyle, M., Derwent, R., Fowler, D., Granier, C., Law, K. S., Mills, G., et al.: Tropospheric ozone and its precursors from the urban to the global scale from air quality to short-lived climate forcer, Atmospheric Chemistry and Physics, 15, 8889–8973, https://doi.org/10.5194/acp-15-8889-2015, 2015.

Monks, S. A., Arnold, S. R., Hollaway, M. J., Pope, R. J., Wilson, C., Feng, W., Emmerson, K. M., Kerridge, B. J., Latter, B. L., Miles, G. M., et al.: The TOMCAT global chemical transport model v1. 6: Description of chemical mechanism and model evaluation, Geoscientific Model Development, 10, 3025–3057, https://doi.org/10.5194/gmd-10-3025-2017, 2017.

Moss, R. H., Babiker, M., Brinkman, S., Calvo, E., Carter, T., Edmonds,

J. A., Elgizouli, I., Emori, S., Lin, E., Hibbard, K., et al.: Towards new scenarios for analysis of emissions, climate change, impacts, and response strategies, IPCC, http://pure.iiasa.ac.at/id/eprint/8659/, 2008.

Mulcahy, J. P., Johnson, C., Jones, C. G., Povey, A. C., Scott, C. E., Sellar, A., Turnock, S. T., Woodhouse, M. T., Abraham, N. L., Andrews, M. B., et al.: Description and evaluation of aerosol in UKESM1 and HadGEM3-GC3. 1 CMIP6 historical simulations, Geoscientific Model Development, 13, 6383–6423, https://doi.org/10.5194/gmd-13-6383-2020, 2020.

Naik, V., Szopa, S., Adhikary, B., Artaxo, P., Berntsen, T., Collins, W., Fuzzi, S., Gallardo, L., Kiendler-Scharr, A., Klimont, Z., Liao, H., Unger, N., Zanis, P., et al.: Climate Change 2021: The Physical Science Basis. Contribution of Working Group I to the Sixth Assessment Report of the Intergovernmental Panel on Climate Change: Chapter 6: Short-Lived Climate Forcers, IPCC, https://www.ipcc.ch/report/ar6/wg1/, 2021.

Newsome, B. and Evans, M.: Impact of uncertainties in inorganic chemical rate constants on tropospheric composition and ozone radiative forcing, Atmospheric Chemistry and Physics, 17, 14 333–14 352, https://doi.org/10.5194/acp-17-14333-2017, 2017.

Nguyen, A., Yosinski, J., and Clune, J.: Deep neural networks are easily fooled: High confidence predictions for unrecognizable images, in: Proceedings of the IEEE conference on computer vision and pattern recognition, pp. 427–436, https://arxiv.org/abs/1412.1897, 2015.

Nicely, J. M., Duncan, B. N., Hanisco, T. F., Wolfe, G. M., Salawitch, R. J., Deushi, M., Haslerud, A. S., Jöckel, P., Josse, B., Kinnison, D. E., et al.: A machine learning examination of hydroxyl radical differences among model

simulations for CCMI-1, Atmospheric Chemistry and Physics, 20, 1341–1361, https://doi.org/10.5194/acp-20-1341-2020, 2020.

O'Connor, F., Johnson, C., Morgenstern, O., Abraham, N., Braesicke, P., Dalvi, M., Folberth, G., Sanderson, M., Telford, P., Voulgarakis, A., et al.: Evaluation of the new UKCA climate-composition model–Part 2: The Troposphere, Geoscientific Model Development, 7, 41–91, https://doi.org/10.5194/gmd-7-41-2014, 2014.

O'Connor, F. M., Abraham, N. L., Dalvi, M., Folberth, G. A., Griffiths, P. T., Hardacre, C., Johnson, B., Kahana, R., Keeble, J., Kim, B., Morgenstern, O., Mulcahy, J. P., Richardson, M., Robertson, E., Seo, J., Shim, S., Teixeira, J. C., Turnock, S. T., Williams, J., Wiltshire, A. J., Woodward, S., and Zeng, G.: Assessment of pre-industrial to present-day anthropogenic climate forcing in UKESM1, Atmospheric Chemistry and Physics, 21, 1211–1243, https://doi.org/10.5194/acp-21-1211-2021, 2021.

O'Neill, B. C., Kriegler, E., Riahi, K., Ebi, K. L., Hallegatte, S., Carter, T. R., Mathur, R., and van Vuuren, D. P.: A new scenario framework for climate change research: the concept of shared socioeconomic pathways, Climatic change, 122, 387–400, https://doi.org/10.1007/s10584-013-0905-2, 2014.

Pacifico, F., Harrison, S., Jones, C., Arneth, A., Sitch, S., Weedon, G., Barkley, M., Palmer, P., Serça, D., Potosnak, M., et al.: Evaluation of a photosynthesis-based biogenic isoprene emission scheme in JULES and simulation of isoprene emissions under present-day climate conditions, Atmospheric Chemistry and Physics, 11, 4371–4389, https://doi.org/10.5194/acp-11-4371-2011, 2011.

Parrish, D. D., Derwent, R. G., Turnock, S. T., O'Connor, F. M., Staehelin,

J., Bauer, S. E., Deushi, M., Oshima, N., Tsigaridis, K., Wu, T., et al.: Investigations on the anthropogenic reversal of the natural ozone gradient between northern and southern midlatitudes, Atmospheric Chemistry and Physics, 21, 9669–9679, https://doi.org/10.5194/acp-21-9669-2021, 2021.

Petersen, A. K., Brasseur, G. P., Bouarar, I., Flemming, J., Gauss, M., Jiang, F., Kouznetsov, R., Kranenburg, R., Mijling, B., Peuch, V.-H., et al.: Ensemble forecasts of air quality in eastern China–Part 2: Evaluation of the MarcoPolo–Panda prediction system, version 1, Geoscientific Model Development, 12, 1241–1266, https://doi.org/10.5194/gmd-12-1241-2019, 2019.

Pierce, T., Geron, C., Bender, L., Dennis, R., Tonnesen, G., and Guenther, A.: Influence of increased isoprene emissions on regional ozone modeling, Journal of Geophysical Research: Atmospheres, 103, 25 611–25 629, https://doi.org/10.1029/98JD01804, 1998.

Prather, M., Flato, G., Friedlingstein, P., Jones, C., Lamarque, J.-F., Liao, H., Rasch, P., et al.: Climate change 2013: the physical science basis: Working Group I contribution to the Fifth assessment report of the Intergovernmental Panel on Climate Change, Cambridge university press, https://www.ipcc.ch/report/ar5/wg1/, 2014.

Qu, Y., Voulgarakis, A., Wang, T., Kasoar, M., Wells, C., Yuan, C., Varma, S., and Mansfield, L.: A study of the effect of aerosols on surface ozone through meteorology feedbacks over China, Atmospheric Chemistry and Physics, 21, 5705–5718, https://doi.org/10.5194/acp-21-5705-2021, 2021.

Rao, S., Klimont, Z., Smith, S. J., Van Dingenen, R., Dentener, F., Bouwman, L., Riahi, K., Amann, M., Bodirsky, B. L., van Vuuren, D. P., Reis, L. A., Calvin, K., Drouet, L., Fricko, O., Fujimori, S., Gernaat,

D., Havlik, P., Harmsen, M., Hasegawa, T., Heyes, C., Hilaire, J., Luderer, G., Masui, T., Stehfest, E., Strefler, J., van der Sluis, S., and Tavoni, M.: Future air pollution in the Shared Socio-economic Pathways, Global Environmental Change-Human and Policy Dimensions, 42, 346–358, https://doi.org/10.1016/j.gloenvcha.2016.05.012, 2017.

Rasp, S., Pritchard, M. S., and Gentine, P.: Deep learning to represent subgrid processes in climate models, Proceedings of the National Academy of Sciences, 115, 9684–9689, https://doi.org/10.1073/pnas.1810286115, 2018.

Ravuri, S., Lenc, K., Willson, M., Kangin, D., Lam, R., Mirowski, P., Fitzsimons, M., Athanassiadou, M., Kashem, S., Madge, S., et al.: Skillful Precipitation Nowcasting using Deep Generative Models of Radar, arXiv preprint arXiv:2104.00954, https://doi.org/10.1038/s41586-021-03854-z, 2021.

Reid, N., Yap, D., and Bloxam, R.: The potential role of background ozone on current and emerging air issues: An overview, Air Quality, Atmosphere & Health, 1, 19–29, https://doi.org/10.1007/s11869-008-0005-z, 2008.

Reynolds, R. W., Smith, T. M., Liu, C., Chelton, D. B., Casey, K. S., and Schlax, M. G.: Daily high-resolution-blended analyses for sea surface temperature, Journal of climate, 20, 5473–5496, https://doi.org/10.1175/2007JCLI1824.1, 2007.

Romer, P. S., Duffey, K. C., Wooldridge, P. J., Edgerton, E., Baumann, K., Feiner, P. A., Miller, D. O., Brune, W. H., Koss, A. R., Gouw, J. A. d., et al.: Effects of temperature-dependent NO x emissions on continental ozone production, Atmospheric Chemistry and Physics, 18, 2601–2614, https://doi.org/10.5194/acp-18-2601-2018, 2018.

Rumelhart, D. E., Hinton, G. E., and Williams, R. J.: Learning representations by back-propagating errors, nature, 323, 533–536, https://doi.org/10.1038/323533a0, 1986.

Salawitch, R., Fahey, D., Hegglin, M., McBride, L., Tribett, W., and Doherty, S.: Twenty Questions and Answers About the Ozone Layer: 2018 Update, Scientific Assessment of Ozone Depletion, https://csl.noaa.gov/assessments/ozone/2018/twentyquestions/, 2019.

Schnell, J. L. and Prather, M. J.: Co-occurrence of extremes in surface ozone, particulate matter, and temperature over eastern North America, Proceedings of the National Academy of Sciences, 114, 2854–2859, https://doi.org/10.1073/pnas.1614453114, 2017.

Schultz, M., Betancourt, C., Gong, B., Kleinert, F., Langguth, M., Leufen, L., Mozaffari, A., and Stadtler, S.: Can deep learning beat numerical weather prediction?, Philosophical Transactions of the Royal Society A, 379, 20200 097, https://doi.org/10.1098/rsta.2020.0097, 2021.

Schultz, M. G., Akimoto, H., Bottenheim, J., Buchmann, B., Galbally, I. E., Gilge, S., Helmig, D., Koide, H., Lewis, A. C., Novelli, P. C., et al.: The Global Atmosphere Watch reactive gases measurement networkThe Global Atmosphere Watch reactive gases measurement network, Elementa: Science of the Anthropocene, 3, https://doi.org/10.12952/journal.elementa.000067, 2015.

Schultz, M. G., Schröder, S., Lyapina, O., Cooper, O. R., Galbally, I., Petropavlovskikh, I., Von Schneidemesser, E., Tanimoto, H., Elshorbany, Y., Naja, M., et al.: Tropospheric Ozone Assessment Report: Database and metrics data of global surface ozone observations, Elementa: Science of the Anthropocene, 5, https://doi.org/10.1525/elementa.244, 2017.

Seinfeld, J. and Pandis, S.: Atmospheric Chemistry and Physics: From Air Pollution to Climate Change, 1998.

Sellar, A. A., Jones, C. G., Mulcahy, J. P., Tang, Y., Yool, A., Wiltshire, A., O'connor, F. M., Stringer, M., Hill, R., Palmieri, J., et al.: UKESM1: Description and evaluation of the UK Earth System Model, Journal of Advances in Modeling Earth Systems, 11, 4513–4558, https://doi.org/10.1029/2019MS001739, 2019.

Shi, Z., Huang, L., Li, J., Ying, Q., Zhang, H., and Hu, J.: Sensitivity analysis of the surface ozone and fine particulate matter to meteorological parameters in China, Atmospheric Chemistry and Physics, 20, 13 455–13 466, https://doi.org/10.5194/acp-20-13455-2020, 2020.

Shore, S. A.: The metabolic response to ozone, Frontiers in immunology, 10, 2890, https://doi.org/10.3389/fimmu.2019.02890, 2019.

Sillman, S.: The use of NO y, H2O2, and HNO3 as indicators for ozone-NO x-hydrocarbon sensitivity in urban locations, Journal of Geophysical Research: Atmospheres, 100, 14 175–14 188, https://doi.org/10.1029/94JD02953, 1995.

Sillman, S.: The relation between ozone, NOx and hydrocarbons in urban and polluted rural environments, Atmospheric Environment, 33, 1821–1845, https://doi.org/10.1016/S1352-2310(98)00345-8, 1999.

Sillman, S. and He, D.: Some theoretical results concerning O3-NOx-VOC chemistry and NOx-VOC indicators, Journal of Geophysical Research: Atmospheres, 107, ACH–26, https://doi.org/10.1029/2001JD001123, 2002.

Sillman, S. and West, J.: Reactive nitrogen in Mexico City and its relation to ozone-precursor sensitivity: results from photochemical models, Atmo-

spheric Chemistry and Physics, 9, 3477–3489, https://doi.org/10.5194/acp-9-3477-2009, 2009.

Sillman, S., Logan, J. A., and Wofsy, S. C.: The sensitivity of ozone to nitrogen oxides and hydrocarbons in regional ozone episodes, Journal of Geophysical Research: Atmospheres, 95, 1837–1851, https://doi.org/10.1029/JD095iD02p01837, 1990.

Sillman, S., He, D., Cardelino, C., and Imhoff, R. E.: The use of photochemical indicators to evaluate ozone-NOx-hydrocarbon sensitivity: Case studies from Atlanta, New York, and Los Angeles, Journal of the Air & Waste Management Association, 47, 1030–1040, https://doi.org/10.1080/10962247.1997.11877500, 1997.

Silver, B., Reddington, C., Arnold, S., and Spracklen, D.: Substantial changes in air pollution across China during 2015–2017, Environmental Research Letters, 13, 114 012, https://doi.org/10.1088/1748-9326/aae718, 2018.

Silver, D., Huang, A., Maddison, C. J., Guez, A., Sifre, L., Van Den Driessche, G., Schrittwieser, J., Antonoglou, I., Panneershelvam, V., Lanctot, M., et al.: Mastering the game of Go with deep neural networks and tree search, nature, 529, 484–489, https://doi.org/10.1038/nature16961, 2016.

Simon, H., Reff, A., Wells, B., Xing, J., and Frank, N.: Ozone trends across the United States over a period of decreasing NOx and VOC emissions, Environmental science & technology, 49, 186–195, https://doi.org/10.1021/es504514z, 2015.

Sindelarova, K., Granier, C., Bouarar, I., Guenther, A., Tilmes, S., Stavrakou, T., Müller, J.-F., Kuhn, U., Stefani, P., and Knorr, W.: Global

data set of biogenic VOC emissions calculated by the MEGAN model over the last 30 years, Atmospheric Chemistry and Physics, 14, 9317–9341, https://doi.org/10.5194/acp-14-9317-2014, 2014.

Sofen, E., Bowdalo, D., Evans, M., Apadula, F., Bonasoni, P., Cupeiro, M., Ellul, R., Galbally, I., Girgzdiene, R., Luppo, S., et al.: Gridded global surface ozone metrics for atmospheric chemistry model evaluation, Earth System Science Data, 8, 41–59, https://doi.org/10.5194/essd-8-41-2016, 2016.

Sønderby, C. K., Espeholt, L., Heek, J., Dehghani, M., Oliver, A., Salimans, T., Agrawal, S., Hickey, J., and Kalchbrenner, N.: Metnet: A neural weather model for precipitation forecasting, arXiv preprint arXiv:2003.12140, https://arxiv.org/abs/2003.12140, 2020.

Stanaway, J. D., Afshin, A., Gakidou, E., Lim, S. S., Abate, D., Abate, K. H., Abbafati, C., Abbasi, N., Abbastabar, H., Abd-Allah, F., et al.: Global, regional, and national comparative risk assessment of 84 behavioural, environmental and occupational, and metabolic risks or clusters of risks for 195 countries and territories, 1990–2017: a systematic analysis for the Global Burden of Disease Study 2017, The Lancet, 392, 1923–1994, https://doi.org/10.1016/S0140-6736(18)32225-6, 2018.

Stevenson, D., Dentener, F., Schultz, M., Ellingsen, K., Van Noije, T., Wild, O., Zeng, G., Amann, M., Atherton, C., and Bell, N.: Multimodel ensemble simulations of present-day and near-future tropospheric ozone, Journal of Geophysical Research: Atmospheres, 111, https://doi.org/10.1029/2005JD006338, 2006.

Stevenson, D. S., Young, P. J., Naik, V., Lamarque, J. F., Shindell, D. T., Voulgarakis, A., Skeie, R. B., Dalsoren, S. B., Myhre, G., Berntsen, T. K.,

Folberth, G. A., Rumbold, S. T., Collins, W. J., MacKenzie, I. A., Doherty, R. M., Zeng, G., van Noije, T. P. C., Strunk, A., Bergmann, D., Cameron-Smith, P., Plummer, D. A., Strode, S. A., Horowitz, L., Lee, Y. H., Szopa, S., Sudo, K., Nagashima, T., Josse, B., Cionni, I., Righi, M., Eyring, V., Conley, A., Bowman, K. W., Wild, O., and Archibald, A.: Tropospheric ozone changes, radiative forcing and attribution to emissions in the Atmospheric Chemistry and Climate Model Intercomparison Project (ACCMIP), Atmospheric Chemistry and Physics, 13, 3063–3085, https://doi.org/10.5194/acp-13-3063-2013, 2013.

Stock, Z., Russo, M., and Pyle, J.: Representing ozone extremes in European megacities: the importance of resolution in a global chemistry climate model, Atmospheric Chemistry and Physics, 14, 3899–3912, https://doi.org/10.5194/acp-14-3899-2014, 2014.

Su, R., Lu, K., Yu, J., Tan, Z., Jiang, M., Li, J., Xie, S., Wu, Y., Zeng, L., Zhai, C., et al.: Exploration of the formation mechanism and source attribution of ambient ozone in Chongqing with an observation-based model, Science China Earth Sciences, 61, 23–32, https://doi.org/10.1007/s11430-017-9104-9, 2018.

Sun, Z. and Archibald, A. T.: Multi-stage ensemble-learning-based model fusion for surface ozone simulations: A focus on CMIP6 models, Environmental Science and Ecotechnology, 8, 100 124, https://doi.org/10.1016/j.ese.2021.100124, 2021.

Sutskever, I., Vinyals, O., and Le, Q. V.: Sequence to sequence learning with neural networks, in: Advances in neural information processing systems, pp. 3104–3112, https://arxiv.org/abs/1409.3215, 2014.

Tai, A. P., Sadiq, M., Pang, J., Yung, D. H., and Feng, Z.: Impacts of Sur-

face Ozone Pollution on Global Crop Yields: Comparing Different Ozone Exposure Metrics and Incorporating Co-effects of CO2, Frontiers in Sustainable Food Systems, 5, 63, https://doi.org/10.3389/fsufs.2021.534616, 2021.

Tan, Z., Lu, K., Jiang, M., Su, R., Wang, H., Lou, S., Fu, Q., Zhai, C., Tan, Q., Yue, D., et al.: Daytime atmospheric oxidation capacity in four Chinese megacities during the photochemically polluted season: a case study based on box model simulation, Atmospheric Chemistry and Physics, 19, 3493–3513, https://doi.org/10.5194/acp-19-3493-2019, 2019.

Tan, Z., Hofzumahaus, A., Lu, K., Brown, S. S., Holland, F., Huey, L. G., Kiendler-Scharr, A., Li, X., Liu, X., Ma, N., et al.: No evidence for a significant impact of heterogeneous chemistry on radical concentrations in the North China plain in summer 2014, Environmental science & technology, 54, 5973–5979, https://doi.org/10.1021/acs.est.0c00525, 2020.

Tarasick, D., Galbally, I. E., Cooper, O. R., Schultz, M. G., Ancellet, G., Leblanc, T., Wallington, T. J., Ziemke, J., Liu, X., Steinbacher, M., et al.: Tropospheric Ozone Assessment Report: Tropospheric ozone from 1877 to 2016, observed levels, trends and uncertainties, Elementa: Science of the Anthropocene, 7, https://doi.org/10.1525/elementa.376, 2019.

Telford, P., Abraham, N., Archibald, A., Braesicke, P., Dalvi, M., Morgenstern, O., O'Connor, F., Richards, N., and Pyle, J.: Implementation of the Fast-JX Photolysis scheme (v6. 4) into the UKCA component of the MetUM chemistry-climate model (v7. 3), Geoscientific Model Development, 6, 161–177, https://doi.org/10.5194/gmd-6-161-2013, 2013.

Tham, Y. J., Wang, Z., Li, Q., Wang, W., Wang, X., Lu, K., Ma, N., Yan, C., Kecorius, S., Wiedensohler, A., et al.: Heterogeneous N 2 O

5 uptake coefficient and production yield of ClNO 2 in polluted northern China: roles of aerosol water content and chemical composition, Atmospheric Chemistry and Physics, 18, 13 155–13 171, https://doi.org/10.5194/acp-18-13155-2018, 2018.

Thornhill, G., Collins, W. J., Kramer, R. J., Olivié, D., Skeie, R. B., O'Connor, F. M., Abraham, N. L., Checa-Garcia, R., Bauer, S. E., Deushi, M., Emmons, L. K., Forster, P. M., Horowitz, L. W., Johnson, B., Keeble, J., Lamarque, J. F., Michou, M., Mills, M. J., Mulcahy, J. P., Myhre, G., Nabat, P., Naik, V., Oshima, N., Schulz, M., Smith, C. J., Takemura, T., Tilmes, S., Wu, T., Zeng, G., and Zhang, J.: Effective radiative forcing from emissions of reactive gases and aerosols – a multimodel comparison, Atmospheric Chemistry and Physics, 21, 853–874, https://doi.org/10.5194/acp-21-853-2021, 2021a.

Thornhill, G., Collins, W., Olivié, D., Skeie, R. B., Archibald, A., Bauer, S., Checa-Garcia, R., Fiedler, S., Folberth, G., Gjermundsen, A., Horowitz, L., Lamarque, J. F., Michou, M., Mulcahy, J., Nabat, P., Naik, V., O'Connor, F. M., Paulot, F., Schulz, M., Scott, C. E., Séférian, R., Smith, C., Takemura, T., Tilmes, S., Tsigaridis, K., and Weber, J.: Climate-driven chemistry and aerosol feedbacks in CMIP6 Earth system models, Atmospheric Chemistry and Physics, 21, 1105–1126, https://doi.org/10.5194/acp-21-1105-2021, 2021b.

Thornton, J., Wooldridge, P., Cohen, R., Martinez, M., Harder, H., Brune, W., Williams, E., Roberts, J., Fehsenfeld, F., Hall, S., et al.: Ozone production rates as a function of NOx abundances and HOx production rates in the Nashville urban plume, Journal of Geophysical Research: Atmospheres, 107, ACH–7, https://doi.org/10.1029/2001JD000932, 2002.

Tolstikhin, I. O., Houlsby, N., Kolesnikov, A., Beyer, L., Zhai, X., Unterthiner, T., Yung, J., Steiner, A., Keysers, D., Uszkoreit, J., et al.: Mlp-mixer: An all-mlp architecture for vision, Advances in Neural Information Processing Systems, 34, https://doi.org/10.48550/arXiv.2105.01601, 2021.

Turnock, S. T., Allen, R. J., Andrews, M., Bauer, S. E., Deushi, M., Emmons, L., Good, P., Horowitz, L., John, J. G., Michou, M., et al.: Historical and future changes in air pollutants from CMIP6 models, Atmospheric Chemistry and Physics, 20, 14 547–14 579, https://doi.org/10.5194/acp-20-14547-2020, 2020.

Valari, M. and Menut, L.: Does an increase in air quality models' resolution bring surface ozone concentrations closer to reality?, Journal of Atmospheric and Oceanic Technology, 25, 1955–1968, https://doi.org/10.1175/2008JTECHA1123.1, 2008.

Van der Werf, G. R., Randerson, J. T., Giglio, L., Collatz, G., Mu, M., Kasibhatla, P. S., Morton, D. C., DeFries, R., Jin, Y. v., and van Leeuwen, T. T.: Global fire emissions and the contribution of deforestation, savanna, forest, agricultural, and peat fires (1997–2009), Atmospheric chemistry and physics, 10, 11 707–11 735, https://doi.org/10.5194/acp-10-11707-2010, 2010.

van Marle, M. J. E., Kloster, S., Magi, B. I., Marlon, J. R., Daniau, A. L., Field, R. D., Arneth, A., Forrest, M., Hantson, S., Kehrwald, N. M., Knorr, W., Lasslop, G., Li, F., Mangeon, S., Yue, C., Kaiser, J. W., and van der Werf, G. R.: Historic global biomass burning emissions for CMIP6 (BB4CMIP) based on merging satellite observations with proxies and fire models (1750-2015), Geoscientific Model Development, 10, 3329–3357, https://doi.org/10.5194/gmd-10-3329-2017, 2017.

Van Vuuren, D. P., Edmonds, J., Kainuma, M., Riahi, K., Thomson, A., Hibbard, K., Hurtt, G. C., Kram, T., Krey, V., Lamarque, J.-F., et al.: The representative concentration pathways: an overview, Climatic change, 109, 5–31, https://doi.org/10.1007/s10584-011-0148-z, 2011.

van Vuuren, D. P., Kriegler, E., O'Neill, B. C., Ebi, K. L., Riahi, K., Carter, T. R., Edmonds, J., Hallegatte, S., Kram, T., Mathur, R., and Winkler, H.: A new scenario framework for Climate Change Research: scenario matrix architecture, Climatic Change, 122, 373–386, https://doi.org/10.1007/s10584-013-0906-1, 2014.

Van Vuuren, D. P., Kriegler, E., O'Neill, B. C., Ebi, K. L., Riahi, K., Carter, T. R., Edmonds, J., Hallegatte, S., Kram, T., Mathur, R., et al.: A new scenario framework for climate change research: scenario matrix architecture, Climatic Change, 122, 373–386, https://doi.org/10.1007/s10584-013-0906-1, 2014.

Vaswani, A., Shazeer, N., Parmar, N., Uszkoreit, J., Jones, L., Gomez, A. N., Kaiser, Ł., and Polosukhin, I.: Attention is all you need, in: Advances in neural information processing systems, pp. 5998–6008, https://arxiv.org/abs/1706.03762, 2017.

Vicedo-Cabrera, A. M., Sera, F., Liu, C., Armstrong, B., Milojevic, A., Guo, Y., Tong, S., Lavigne, E., Kyselỳ, J., Urban, A., et al.: Short term association between ozone and mortality: global two stage time series study in 406 locations in 20 countries, bmj, 368, https://doi.org/10.1136/bmj.m108, 2020.

Von Schneidemesser, E., Monks, P. S., Allan, J. D., Bruhwiler, L., Forster, P., Fowler, D., Lauer, A., Morgan, W. T., Paasonen, P., Righi, M., et al.: Chemistry and the linkages between air quality and climate change,

Chemical Reviews, 115, 3856–3897, https://doi.org/10.1021/acs.chemrev.5b00089, 2015.

Voulgarakis, A., Wild, O., Savage, N., Carver, G., and Pyle, J.: Clouds, photolysis and regional tropospheric ozone budgets, Atmospheric Chemistry and Physics, 9, 8235–8246, https://doi.org/10.5194/acp-9-8235-2009, 2009.

Walters, D., Baran, A. J., Boutle, I., Brooks, M., Earnshaw, P., Edwards, J., Furtado, K., Hill, P., Lock, A., Manners, J., et al.: The Met Office Unified Model global atmosphere 7.0/7.1 and JULES global land 7.0 configurations, Geoscientific Model Development, 12, 1909–1963, https://doi.org/10.5194/gmd-12-1909-2019, 2019.

Wang, J., Ge, B., and Wang, Z.: Ozone production efficiency in highly polluted environments, Current Pollution Reports, 4, 198–207, https://doi.org/10.1007/s40726-018-0093-9, 2018.

Wang, N., Lyu, X., Deng, X., Huang, X., Jiang, F., and Ding, A.: Aggravating O3 pollution due to NOx emission control in eastern China, Science of the Total Environment, 677, 732–744, https://doi.org/10.1016/j.scitotenv.2019.04.388, 2019.

Wang, T., Xue, L., Brimblecombe, P., Lam, Y. F., Li, L., and Zhang, L.: Ozone pollution in China: A review of concentrations, meteorological influences, chemical precursors, and effects, Science of the Total Environment, 575, 1582–1596, 2017a.

Wang, T., Xue, L., Brimblecombe, P., Lam, Y. F., Li, L., and Zhang, L.: Ozone pollution in China: A review of concentrations, meteorological influ-

ences, chemical precursors, and effects, Science of the Total Environment, 575, 1582–1596, https://doi.org/10.1016/j.scitotenv.2016.10.081, 2017b.

Wang, W., van der A, R., Ding, J., van Weele, M., and Cheng, T.: Spatial and temporal changes of the ozone sensitivity in China based on satellite and ground-based observations, Atmospheric Chemistry and Physics, 21, 7253–7269, https://doi.org/10.5194/acp-21-7253-2021, 2021.

Whalley, L. K., Slater, E. J., Woodward-Massey, R., Ye, C., Lee, J. D., Squires, F., Hopkins, J. R., Dunmore, R. E., Shaw, M., Hamilton, J. F., et al.: Evaluating the sensitivity of radical chemistry and ozone formation to ambient VOCs and NO x in Beijing, Atmospheric Chemistry and Physics, 21, 2125–2147, https://doi.org/10.5194/acp-21-2125-2021, 2021.

WHO: Review of evidence on health aspects of air pollution: REVIHAAP project: technical report, Tech. rep., World Health Organization. Regional Office for Europe, https://www.euro.who.int/__data/assets/pdf_file/0004/193108/REVIHAAP-Final-technical-report-final-version.pdf, 2021.

Wild, O.: Modelling the global tropospheric ozone budget: exploring the variability in current models, Atmospheric Chemistry and Physics, 7, 2643–2660, https://doi.org/10.5194/acp-7-2643-2007, 2007.

Wild, O. and Prather, M. J.: Global tropospheric ozone modeling: Quantifying errors due to grid resolution, Journal of Geophysical Research: Atmospheres, 111, https://doi.org/10.1029/2005JD006605, 2006.

Wild, O., Voulgarakis, A., O'Connor, F., Lamarque, J.-F., Ryan, E. M., and Lee, L.: Global sensitivity analysis of chemistry–climate model budgets of tropospheric ozone and OH: exploring model diversity, Atmo-

spheric Chemistry and Physics, 20, 4047–4058, https://doi.org/10.5194/acp-20-4047-2020, 2020.

Williams, K., Copsey, D., Blockley, E., Bodas-Salcedo, A., Calvert, D., Comer, R., Davis, P., Graham, T., Hewitt, H., Hill, R., et al.: The Met Office global coupled model 3.0 and 3.1 (GC3. 0 and GC3. 1) configurations, Journal of Advances in Modeling Earth Systems, 10, 357–380, https://doi.org/10.1002/2017MS001115, 2018.

Wittig, V. E., Ainsworth, E. A., and Long, S. P.: To what extent do current and projected increases in surface ozone affect photosynthesis and stomatal conductance of trees? A meta-analytic review of the last 3 decades of experiments, Plant, cell & environment, 30, 1150–1162, https://doi.org/10.1111/j.1365-3040.2007.01717.x, 2007.

Wu, R. and Xie, S.: Spatial distribution of ozone formation in China derived from emissions of speciated volatile organic compounds, Environmental science & technology, 51, 2574–2583, https://doi.org/10.1021/acs.est.6b03634, 2017.

Wu, S., Mickley, L. J., Jacob, D. J., Logan, J. A., Yantosca, R. M., and Rind, D.: Why are there large differences between models in global budgets of tropospheric ozone?, Journal of Geophysical Research: Atmospheres, 112, https://doi.org/10.1029/2006JD007801, 2007.

Xing, J., Ding, D., Wang, S., Dong, Z., Kelly, J. T., Jang, C., Zhu, Y., and Hao, J.: Development and application of observable response indicators for design of an effective ozone and fine-particle pollution control strategy in China, Atmospheric chemistry and physics, 19, 13 627–13 646, https://doi.org/10.5194/acp-19-13627-2019, 2019.

Ye, L., Wang, X., Fan, S., Chen, W., Chang, M., Zhou, S., Wu, Z., and Fan, Q.: Photochemical indicators of ozone sensitivity: application in the Pearl River Delta, China, Frontiers of Environmental Science & Engineering, 10, 1–14, https://doi.org/10.1007/s11783-016-0887-1, 2016.

Young, P., Archibald, A., Bowman, K., Lamarque, J.-F., Naik, V., Stevenson, D., Tilmes, S., Voulgarakis, A., Wild, O., Bergmann, D., et al.: Pre-industrial to end 21st century projections of tropospheric ozone from the Atmospheric Chemistry and Climate Model Intercomparison Project (ACCMIP), Atmospheric Chemistry and Physics, 13, 2063–2090, https://doi.org/10.5194/acp-13-2063-2013, 2013.

Young, P. J., Naik, V., Fiore, A. M., Gaudel, A., Guo, J., Lin, M., Neu, J., Parrish, D., Rieder, H., and Schnell, J.: Tropospheric Ozone Assessment Report: Assessment of global-scale model performance for global and regional ozone distributions, variability, and trends, Elementa: Science of the Anthropocene, 6, 2018a.

Young, P. J., Naik, V., Fiore, A. M., Gaudel, A., Guo, J., Lin, M., Neu, J., Parrish, D., Rieder, H., Schnell, J., et al.: Tropospheric Ozone Assessment Report: Assessment of global-scale model performance for global and regional ozone distributions, variability, and trends, Elementa: Science of the Anthropocene, 6, https://doi.org/10.1525/elementa.265, 2018b.

Zhai, S., Jacob, D. J., Wang, X., Liu, Z., Wen, T., Shah, V., Li, K., Moch, J. M., Bates, K. . H., Song, S., et al.: Control of particulate nitrate air pollution in China, Nature Geoscience, 14, 389–395, https://doi.org/10.1038/s41561-021-00726-z, 2021.

Zhang, J. J., Wei, Y., and Fang, Z.: Ozone pollution: a major health hazard

worldwide, Frontiers in immunology, 10, 2518, https://doi.org/10.3389/fimmu.2019.02518, 2019a.

Zhang, Q., Zheng, Y., Tong, D., Shao, M., Wang, S., Zhang, Y., Xu, X., Wang, J., He, H., Liu, W., et al.: Drivers of improved PM2. 5 air quality in China from 2013 to 2017, Proceedings of the National Academy of Sciences, 116, 24 463–24 469, https://doi.org/10.1073/pnas.1907956116, 2019b.

Zhang, Y.: Online-coupled meteorology and chemistry models: history, current status, and outlook, Atmospheric Chemistry and Physics, 8, 2895–2932, https://doi.org/10.5194/acp-8-2895-2008, 2008.

Zhao, C., Wang, Y., Yang, Q., Fu, R., Cunnold, D., and Choi, Y.: Impact of East Asian summer monsoon on the air quality over China: View from space, Journal of Geophysical Research: Atmospheres, 115, https://doi.org/10.1029/2009JD012745, 2010.

Zhao, Y., Zhang, L., Zhou, M., Chen, D., Lu, X., Tao, W., Liu, J., Tian, H., Ma, Y., and Fu, T.-M.: Influences of planetary boundary layer mixing parameterization on summertime surface ozone concentration and dry deposition over North China, Atmospheric Environment, 218, 116 950, https://doi.org/10.1016/j.atmosenv.2019.116950, 2019.

Zheng, B., Tong, D., Li, M., Liu, F., Hong, C., Geng, G., Li, H., Li, X., Peng, L., Qi, J., et al.: Trends in China's anthropogenic emissions since 2010 as the consequence of clean air actions, Atmospheric Chemistry and Physics, 18, 14 095–14 111, https://doi.org/10.5194/acp-18-14095-2018, 2018.